Doctoral Dissertation

Molecular dynamics simulation study of Si-based materials etching processes

Erin Joy Capdos Tinacba

June 2021

Quantum Engineering and Design Course

Division of Precision Science & Technology and

Applied Physics

Graduate School of Engineering

OSAKA UNIVERSITY

To my dad...

Acknowldegement

I would like to express my sincere gratitude to everyone who helped me in my Ph.D. journey.

I thank Professor Satoshi Hamaguchi for accepting me in his laboratory when I was looking for a university to study in Japan. He has opened a lot of opportunities to expand my knowledge and my research experience. I appreciate his never ending support to keep me going with my research. I also thank him for his advice not just in research, but also in my career and personal life.

I thank everyone in Hamaguchi Laboratory, especially, Cha, Anjar, Nina, Umemura-san, Ito-san, Nicolas, Enggar, Jomar, Abdul, Ikuse-san, Isobe-san, Hojun, Jaber, Taira-kun, Daichi, Ichi, Kita-kun, and Kotani-kun for, making my life extra fun. You guys are awesome! I thank you for your patience in listening to my never ending stories, and for actively participating in the activities that I have organized.

I thank my family for their never ending support in all my decisions and dreams. We might be physically too far from each other but knowing that you are always with me gives me extra strength everyday.

My special thanks goes to Fumiaki Funama. Thank you for your love, understanding, patience, care, and everything that you have done for me. No words can describe how much I appreciate you. You are, indeed, the extra sunshine to my life.

Lastly, I want to thank God for His never ending blessings and guidance as I go through my Ph.D. journey.

Abstract

The continuous miniaturization of electronic devices has brought tremendous innovations to the modern technology especially in memory devices such as two dimensional (2D) NAND flash memory. However, as this miniaturization approaches its scaling limit, new challenges on the fabrication processes are arising. One of which is the need for new etching methods as the structure of memory devices shifts from 2D to three dimensional (3D) architecture. In the newly developed 3D NAND device, the memory cells are stacked vertically to increase its capacity and performance. To achieve this, alternating layers of semiconductor materials such as silicon (Si) and silicon dioxide (SiO_2), and in some cases, with silicon nitride (Si_3N_4), are stacked together. Memory cells are then fabricated through a series of lithography, etching, and deposition processes. Reactive ion etching (RIE) is a common known technique to fabricate holes on the stacked layer. However, as the aspect ratio of these holes increases with increasing number of stacked layers, the etching process becomes difficult. New etching methods that can provide higher etching yields and more isotropic etching is necessary. Plasma assisted atomic layer etching (PA-ALE) is also gaining much attention as it can provide highly uniform etching, better precision and low surface damage compared with the traditional RIE process.

In this study, classical molecular dynamics (MD) simulation was used to study the mechanisms in the RIE of Si and SiO_2 materials with ions that contain large amount of F atoms, and to have a better understanding of the role of F atoms during the etching process. $C_2F_5^+$, NF_2^+ and SF_5^+ ions were irradiated on the Si and SiO_2 materials to explore the capability of these ions for a faster one step etching process of alternating Si and SiO_2 stacked layers. The development of a simple sulfur (S) and F atoms interatomic potential

was also discussed. Based on the results, a good agreement between the simulated and multi-beam system experimental etching yields was achieved, which showed the validity of the simulation. The etching yields with $C_2F_5^+$ and SF_5^+ ion bombardments were higher compared with NF_2^+ ion bombardment. This indicates that more F atoms during the etching process is important to achieve high etching yield. For the case of the Si material, the etching yields with SF_5^+ ion bombardment is significantly higher than $C_2F_5^+$ ion bombardment for all ion energy range. As seen in the bond distribution profiles of the $C_2F_5^+$ ion irradiated Si material, this is because carbon (C) atoms can easily bond with Si atoms forming SiC layer which is known to be a stable and relatively hard material, thus hindering the etching. In the case of the SiO_2 material, C atoms bonded with oxygen (O) atoms forming volatile products such as CO. Therefore, the etching yields with $C_2F_5^+$ and SF_5^+ ion bombardments were almost the same. The analysis of desorbed species for all cases showed that the etching is due to the desorption of monoatomic Si and SiF_x (x = 1 - 4) desorbed species. The percentage of Si desorbed species increases while the percentage of SiF_x desorbed species decreases with increasing ion energy. Moreover, the effect of pure chemical etching, i.e. formation of SiF_4, diminished at very high ion energy. These results indicate that the etching process is dominantly due to physical sputtering effect as the energy increases.

MD simulation was also employed to study the feasibility of other gases such as I_2 in Si and SiO_2 etching. Modified Stillinger-Weber potential function was used to describe the interatomic interactions of Si, O, and I systems. The RIE of Si and SiO_2 materials with I^+ ion bombardment was then simulated. The simulated etching yields of Si and SiO_2 materials with I^+ ion bombardment were not that different from the etching yields with F^+, Cl^+ and Br^+ ion bombardments obtained from multi-beam system experiments. The desorbed species analysis showed that the etching process with I^+ ion bombardment is highly dependent on the desorption of monoatomic Si desorbed species for all energy range. Low percentages of SiI_x (x =1 -3) desorbed species were observed.

The surface damage formation in PA-ALE of Si with Cl desorption and low-energy Ar^+ ion bombardment was also studied using classical MD simulation. The effects of the

deposited Cl layer thickness and the Ar^+ ion energy on the etch per cycle (EPC) and surface damage formation were reported. Several cycles with reproducible etched depths per cycle were simulated for each ion energy. The EPC increased with ion energy. Based on the depth profiles, around 1.5 nm surface damage thickness was observed even at 20 eV Ar^+ ion energy, wherein ideal ALE condition is expected. This thickness moderately increased with increasing Ar^+ ion energy due to the transportation of the deposited Cl atoms deeper into the Si material by the ion bombardment. The simulation results imply that formation of damaged-layer is hard to avoid in PA-ALE process. In actual applications, if this damaged-layer has serious effects on the device performance, subsequent steps to reduce the thickness should be considered.

List of Abbreviations

ALE atomic layer etching

Ar argon

Cl chlorine

C_2F_5 pentafluoroethyl

DFT Density Functional Theory

F fluorine

EPC etch per cycle

I iodine

MD molecualr dynamics

NF_2 nitrogen difluoride

PA-ALE plasma assisted atomic layer etching

RIE reactive ion etching

SACs self aligned contacts

Si silicon

SiO_2 silicon dioxide

SF_5 sulfur pentafluoride

SW potential Stillinger-Weber potential

VdW potential Van der Waals potential

2D NAND two-dimensional NAND

3D NAND three-dimensional NAND

Contents

Chapter 1

Introduction

In 1965, Gordon Moore predicted that the number of transistors in a single chip will double every year [1]. True enough, as technology advances, the size of cells in electronic devices continuously decreased throughout the years. This has brought tremendous advancement especially in the field of memory devices as the scalling down of the memory cells is equivalent to an increase in memory density. However, recently, as the half-pitch for a cell reached below 20 nm [2], cell fabrication has reached its scaling limit. This has imposed several challenges in the fabrication processes of electronic devices such as lithography, etching, and deposition.

Conventionally, the memory cells are arranged in horizontal direction which is commonly known as 2D NAND Flash memory. This has wide applications in modern gadgets such as phones and solid-state storage devices [3, 4]. In order to compensate for the physical limitions brought by the miniaturization of the cells, the structure shifted from 2D planar to 3D NAND [2–6]. Severarl 3D NAND architecture were proposed such as pipe-shaped bit-cost scalable (P-BiCS), terabit cell array transistor (TCAT), vertial stack array transistor (VSAT) and vertical gate (VG) [6]. The general theme of these proposed architectures is that the memory cells are stacked up vertically in order to accommodate more cells for the same surface area.

Figure 1.1 [7] shows the general schematic diagram of a 3D NAND device structure. It is typically composed of alternating layers of silicon (Si) and silicon dioxide (SiO_2)

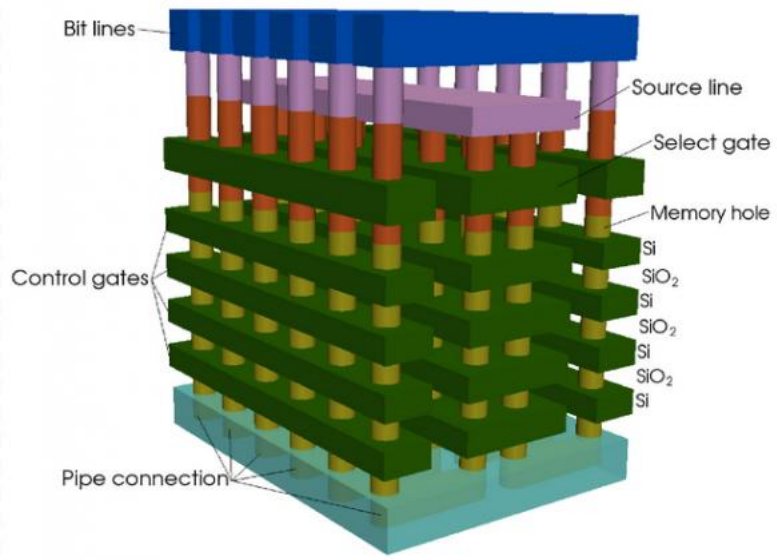

Figure 1.1: Schematic diagram of a 3D NAND device [7].

and in some cases, silicon nitride (Si_3N_4) materials. The memory cells are constructed through a series of lithography, etching, and deposition processes. The development of the 3D NAND architecture paved a way for the fabrication of ultra-high memory density devices. However, several challenges are encountered in the integration of cells in each stacked layers. The fabrication requires more critical lithography steps compared to the 2D NAND to make the minimum feature size of each cell. Driver transistors for contol gates are also needed in each layer [5]. Moreover, perhaps the most critical problem is the need for high aspect ratio etching especially as the number of layers increases. One of the major processes in the fabrication is to dig deep trenches or holes on the stacked layers. The ability of the current available etching methods such as wet etching and plasma etching is only limited to certain aspect ratio, i.e. ratio of the trench diameter and trench depth. As the trench diameter decreases and the number of stacked layers increases (which corresponds to an increase in trench depth), the etching becomes harder and more complicated. Several problems are encountered such as microloading, aspect ratio dependent etching (ARDE), micrograss, tilting and notching [8]. The race in discovering new, cost effective and faster etching methods to solve these challenges in the fabrication of the next generation of memory devices has been on going for the past few years.

1.1 Plasma Etching

Etching is one of the most essential procedures in semiconductor fabrication processes. This can be achieved through wet eching or dry etching methods. Wet etching involves the use of liquid chemicals or etchants such as potassium hydroxide (KOH) to etch the semiconductor wafers. Exposure to KOH solution leads to the oxidation of Si surface, thus etching is induced. Si surfaces were initially etched through wet etching. However, the applications of this method especially in patterning can be limited [8]. On the otherhand, dry etching utilizes ions and radicals from plasmas to etch the surface of semiconductor wafers. This is more advantages than wet etching because it can produce highly directional and anisotropic patterns on the materials.

Plasmas are composed of electrically neutral mixture of molecules, ions, radicals, electrons, photons, and neutrals [9]. These are generated by ionizing neutral gases. By taking advantage of the accelerating voltage of the ions across the plasma sheath, anisotropic etching of materials is possible. This can be further enhanced by applying bias voltage on the surface to adjust the potential drop across the plasma sheath [8].

The applications of plasma etching of semiconductor materials can vary by taking advantage of the plasma properties such as ion energy. In the succeeding subsections, two well-known plasma etching methods, reactive ion etching (RIE) and plasma assisted atomic layer etching (PA-ALE), will be discussed.

1.1.1 Reactive Ion Etching

In RIE, the ions and radicals from the plasma etch the material through physical and chemical sputtering [10]. In physical sputtering, the surface atoms are sputtered out from the surface due to the high kinetic energy from the incoming ions. In chemical sputtering, the radicals from the plasma or the reactive component of the ions bond on the surface atoms, weakening the bonding energy of the atoms on the surface. Thus, volatile products are formed such as SiF_4 in the case of Si-based materials etching with fluorocarbon plasmas [11]. In most cases, the etching is due to the combination of both

physical and chemical sputtering effects. In other words, the plasma radicals weaken the surface bonds and in effect, lesser ion impact energy is required to physically sputter the molecules from the surface.

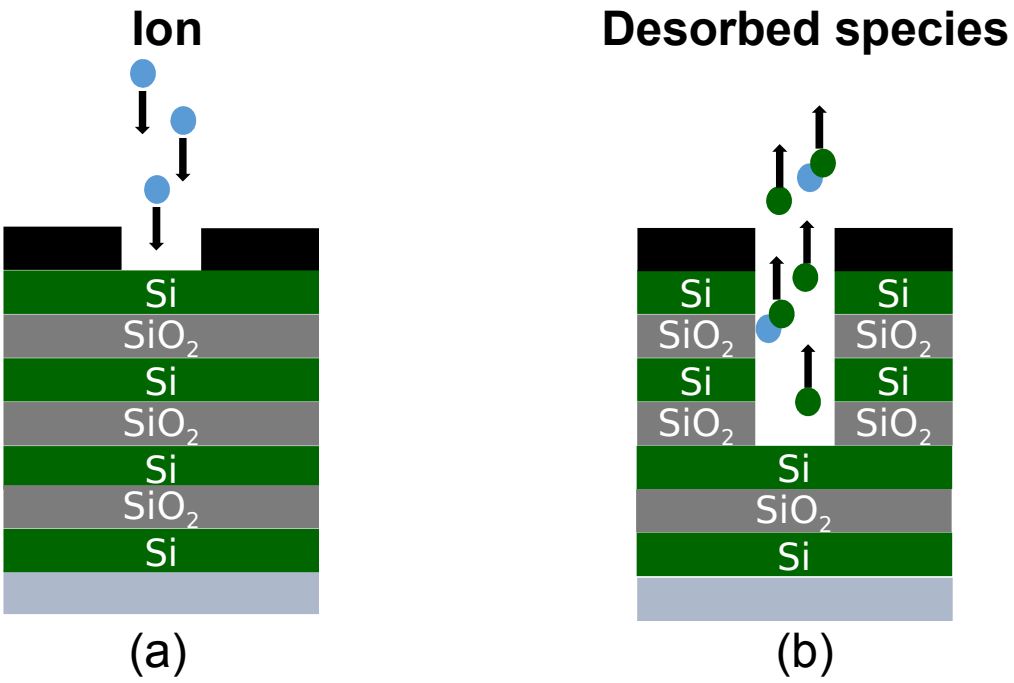

Figure 1.2: Illustration of reactive ion etching of stacked layers of Si and SiO_2 materials with (a) ion injection, and (b) etching due to desorption of volatile species.

RIE is typically used in semiconductor materials processing. Figure 1.2 shows an illustration of the RIE of stacked Si and SiO_2 materials, which are typically used in 3D NAND devices. In such devices, highly directional and uniform etching is desired, which can be achieved with RIE. However, with the recent nano-scaling of electronic devices, several etching challenges have arisen. One of which is the need for high aspect ratio etching that is able to provide a uniform vertical profile especially as the number of layers in such devices increases.

1.1.2 Plasma Enhanced Atomic Layer Etching

Recently, atomic layer processes such as ALE and atomic layer deposition is gaining much attention due to the increasing demand for innovation to cater the challenges in nano-scaling of electronic devices. In ALE, the etching process is divided into adsorption and desorption steps [12]. In the adsorption step, reactive species were deposited on the

surface to modify and weaken the bonds on the surface of the bulk material. Then in the adsorption step, the modified surface is etched. Ideally, a monolayer should be deposited in the first step and modify the adjacent monolayer of the surface. In effect, when the deposited layer is depleted on the surface during the adsorption step, the etching stops and only a monolayer of the surface is etched. This is called the self-limiting property of ALE. These two steps constitute one cycle of the ALE and are illustrated in Fig. 1.3. In a typical ALE process, this cycle is repeated for several times until the desired etched depth is achieved. Unlike in the RIE, the etching rate in ALE is low. However, the patterning precision is high and offers no or very low surface damage especially on the material. This makes it ideal in fabrication of devices that requires the etching of the top layer only, but not the adjacent layers such as in self-aligned contacts (SACs) [13].

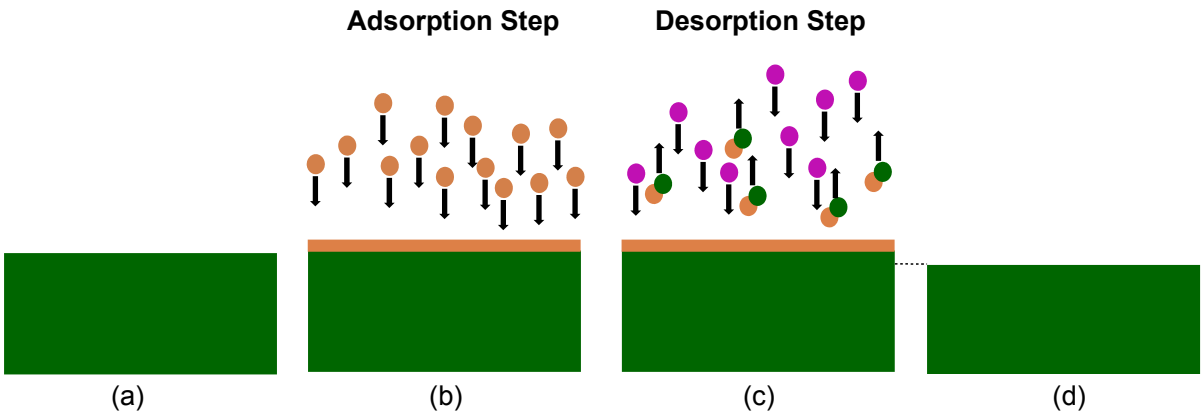

Figure 1.3: Illustration of one cycle in plasma assisted atomic layer etching (PA-ALE). In PA-ALE, the clean material (a) is modified by deposition of reactive species in the adsorption step (b). In the desorption step (c), the modified surface is etched with the injection of energetic ions from a plasma source, as indicated by the magenta spheres, until a monolayer or a thin layer of the material is removed (d).

ALE can be achieved through thermal [14, 15] and plasma processes [12, 16]. In plasma assisted ALE (PA-ALE) of Si material, chlorine (Cl) atoms from Cl_2 gas or low energy Cl plasma are normally deposited in the adsorption step because it is not reactive enought to etch the surface and it normally remains only on the top surface. In the desorption step, non-reactive plasma such as argon (Ar) plasma is typically used. Ideally, the plasma should not be energetic enough to etch the bare surface of Si, which means that the etching is fully dependent on the presence of the deposited species from the

previous step.

The early works on PA-ALE, in which it was called digital etching, of Si were reported by Horiike *et al.* [16–19] in the 1990s. They have studied several gas chemistries in the adsorption step including CF_4/O_2 [16], NF_3/N_2 and F_2/He [17], and Cl_2 [18]. The surface was irradiated with low energy Ar plasma in the desorption step. Based on their results, the gas chemistry in the adsorption step and adsorption time greatly affected the etch per cycle (EPC). An EPC of 1.5 Å/cycle, which is close to the 1.35 Å thickness of Si(100) monolayer, for 0.5 s CF_4/O_2 adsorption was achieved. Higher EPC values of 8 Å/cycle for pure NF_3 gas, and 5.7 Å/cycle for F_2/95% He were reported. The results with these gas chemistries indicated that the etching is due to the F chemisorption on the Si surface. In their later studies, Cl atoms were deposited on the surface and an EPC of 0.4 Å/cycle, which is less than a monolayer of Si, was calculated at very low bias voltage. They have also demonstrated the potential of ALE in the fabrication of trenches in Si. The results showed that ALE process produced features with better anisotropy compared to the tradional RIE. Furthermore, no microloading was observed, which is normally encountered in RIE of Si as the trench depth increases. However, these results did not gain much attention until recently when nanometer scaling of electronic devices became a trend in electronic device fabrication. Other papers on Si ALE with Cl adsorption and Ar^+ ion bombardment were published in recent years [20–24].

Nowadays, the applications of PA-ALE have expanded to other materials such as stacked SiO_2 and Si_3N_4 which are typical components in SACs [13, 25–29]. In most cases, fluorocarbon plasmas are also used to deposit a polymer on the surface in the adsorption step. Reports on non-ideal or quasi-ALE, wherein the etching does not fully stop or observation of ARDE, are also published [30].

1.2 Classical Molecular Dynamics Simulation

Several numerical methods were developed to study the surface and ion interactions such as Monte Carlo simulation [28, 30–33], molecular dynamics (MD) simulation [25, 34–39]

and *ab-inito* calculation [40]. The details of the MD simulation used in this research are discussed in the following subsections.

1.2.1 Modified Stillinger-Weber Potential Function

Classical MD simulation is used to study the atomic scale mechanisms of a system by solving Newton's equations of motion of each atom in the system. The equations of motions of the atoms are dependent on the potential functions that are used to describe the interactions of the atoms. In 1985, Frank H. Stillinger and Thomas A. Weber [41] developed a model potential-energy function to describe the interaction of Si atoms in a Si material. For any given system with N number of particles, the total potential Φ is given by

$$\Phi(1,...,N) = \sum_{i} V_1(i) + \sum_{i,j} V_2(i,j) + \sum_{i,j,k} V_3(i,j,k) + ... + V_{\mathrm{N}}(1,...,\mathrm{N})$$

where V_1, V_2, V_3, V_{N} are the one-body, two-body, three-body and so on potential contributions. However, to simplify the equation, it was assumed that V_{N} goes to zero with higher N. The one-body term V_1 is also assumed to be zero as this describes external forces experienced by each atom. Thus, the total potential Φ can be summarized as the sum of the two-body and three-body contributions

$$\Phi(i,j,k) = \sum_{i,j} V_2(i,j) + \sum_{i,j,k} V_3(i,j,k).$$

The original forms of V_2 and V_3 of the Stillinger and Weber (SW) potential model were modified by Ohta *et. al.* [39] to describe the interactions of Si-O-F and Si-O-Cl systems. The potentials reported by Ohta *et. al.* was further simplified for easier parameterization. The details of these potential functions are described in Chapter 3. Here, a brief summary of the modified Stillinger-Weber potential function will be described based on Refs. [39, 42, 43].

The two-body V_2 term is the summation of the repulsive V_{R} and attractive V_{B} bonding

between two atoms.

$$V_{\mathrm{R}} = ar^{-p} \exp\left(\frac{c}{r - r_c}\right)$$

$$V_{\mathrm{B}} = -br^{-q} \exp\left(\frac{d}{r - r_c}\right)$$

Assuming that the repulsive part is linearly dependent on the square of the attractive interaction, $p = 2q$ and $c = 2d$, then V_2 can be written as

$$V_2(r) = ar^{-2q} \exp\left(\frac{2d}{r - r_c}\right) - br^{-q} \exp\left(\frac{d}{r - r_c}\right), \text{ if } r > r_c, \tag{1.1}$$

where a, b, d, q, and r_c are parameters. The parameter r_c is the cut-off length, i.e., $V_2 = 0$ if $r \geq r_c$.

The three-body potential V_3 is use to define the angular dependencies of the potential. For three atoms i, j, k, V_3 is equal to the summation of three h fuctions

$$V_3(i, j, k) = h_{ijk}(r_{ij}, r_{ik}, \theta_{jik}) + h_{jik}(r_{ji}, r_{jk}, \theta_{ijk}) + h_{ikj}(r_{ki}, r_{kj}, \theta_{ikj}). \tag{1.2}$$

One h function is dependent on the angle between three atoms θ_{ijk} and the distances of the two atoms, r_{ji} and r_{jk}, from the vertex atom j, and is given by

$$h_{ijk}(r_{ji}, r_{kj}, \theta_{ijk}) = k_{ijk} |\cos\theta_{ijk} - \Theta_{ijk}|^{\gamma_{ijk}} f_{ij}(r_{ij}) f_{kj}(r_{kj}), \tag{1.3}$$

where f is used to prevent the overestimation of the angular dependency. This is dependent on the function V_2,

$$f_{ij}(r) = \begin{cases} 1, & r \leq r_{\min}, \\ \frac{V_2(r)}{V_{2\min}}, & r_{\min} < r < r_c, \\ 0, & r > r_c, \end{cases}$$

where $r_{\min}$ is the bond distance between i and j atoms at the minimum bond energy $V_{2\min}$.

1.2.2 Van der Waals Potential

The Van der Waals (VdW) potential was also used to account for relatively longer-range weak interactions among neighboring atoms, which can affect up to third neighboring atoms in a solid, as described by Ohta *et al.* [42]. The pairwise bond energy of a VdW interaction is extremely weak compared with that of a typical covalent bond, being only about 0.01 eV. In the MD simulation used in this study, we use the same pairwise attractive interaction model for all the atoms in the simulation box for the sake of simplicity, whose functional form is given by the following Lennard-Jones type function;

$$V_{VdW}(r) = \begin{cases} 4\epsilon\left\{ \left(\frac{\sigma}{r}\right)^{12} - \left(\frac{\sigma}{r}\right)^{6} \right\} \exp\left(\frac{d_1}{r-c_1} - \frac{d_2}{r-c_2}\right), & \text{if } c_2 < r < c_1, \\ 0, & \text{otherwise,} \end{cases} \tag{1.4}$$

where $\epsilon = 0.0108$ eV, $\sigma = 3.5$ Å, $d_1 = d_2 = 0.1$ Å, $c_1 = 8.0$ Åand $c_2 = 3.5$ Å. The exponential function was used to ensure that the function is continuously differentiable for all r, as in the SW potential. The VdW potential function above is plotted in Fig. 1.4. It should be noted that the energy at the bottom of the potential well of Fig. 1.4 is two orders of magnitude smaller than that of the two-body covalent bond described by V_2.

1.2.3 Integration Algorithm

In classical MD simulation, each atom in the system is treated as classical particles [44]. The force F_i acting on each atom i can be derived from the potential function Φ as

$$F_i = -\frac{\partial}{\partial r_i}\Phi.$$

The trajectory of each atom is determined by numerically solving the Newton's equations of motions,

$$\vec{F_i} = m_i\vec{a_i} = m_i\frac{\partial^2\vec{r_i}(t)}{\partial t^2},$$

$$\vec{p_i} = m_i\dot{\vec{r}}_i,$$

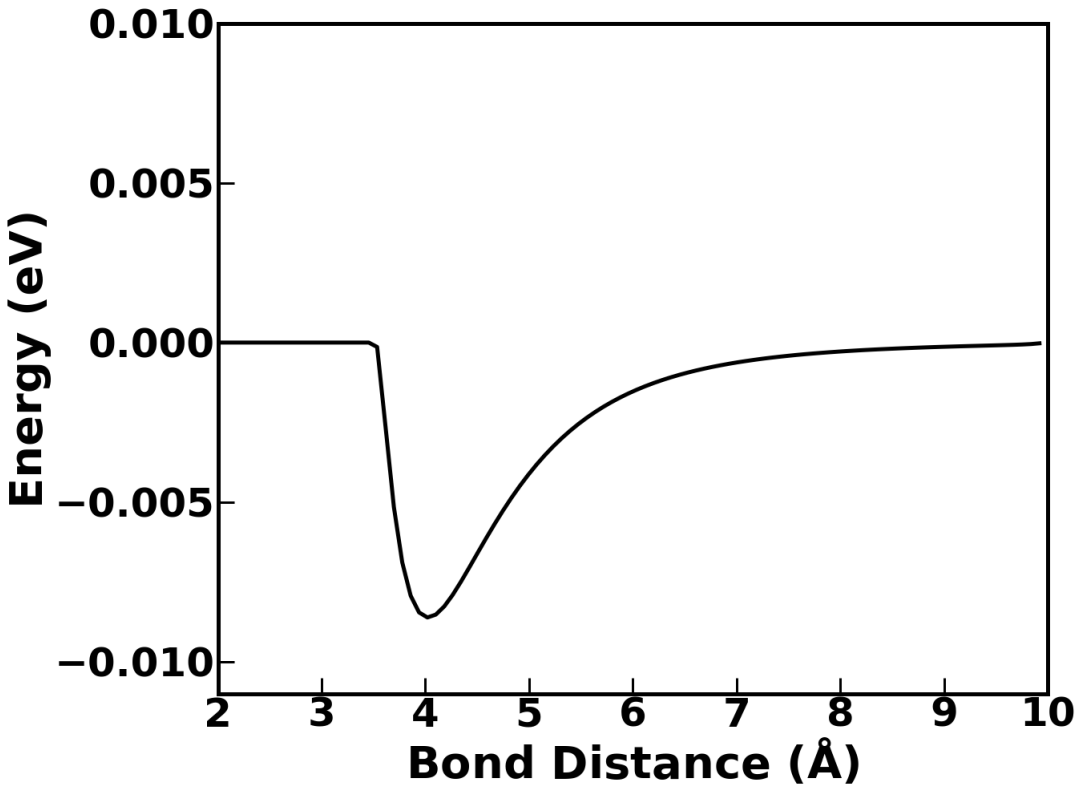

Figure 1.4: The functional form of the VdW potential model used in this study.

where m_i is the mass of the atom, r_i is the position at a certain time t, and p_i is the momentum. To accurately describe the interactions of the atoms in the system, r_i should be evaluated using an infinitely small time steps Δt.

There are several integration algorithm that are employed in simulations such as the finite difference method, Verlet algorithm and the velocity Verlet or leap-frog algorithm. In Verlet algorithm [45, 46], the positions r_i are computed at different times, t and Δt, using the Taylor series expansion.

$$r_i(t + \Delta t) = r_i(t) + \Delta t v(t) + \frac{1}{2}(\Delta t)^2 a(t) + ...$$

$$r_i(t - \Delta t) = r_i(t) - \Delta t v(t) + \frac{1}{2}(\Delta t)^2 a(t) - ...$$

The succeeding position of the atom at $t + \Delta t$ is then determined using the previous two equations

$$r_i(t + \Delta t) = 2r_i(t) - r_i(t + \Delta t) + (\Delta t)^2 a(t).$$

The velocity of the atom, which is a useful parameter in calculating the total energy of the system, is

$$v_i(t) = \frac{r_i(t + \Delta t) - r_i(t - \Delta t)}{2\Delta t}.$$

1.2.4 Microcanonical Ensemble and Thermostat Algorithms

Statistical mechanics is employed on MD simulations to extract relevant information on the macroscopic properties of the system. Typically, MD simulations are conducted under microcanonical ensemble or commonly known as constant NVE. In NVE, the number of particles N, volume of the simulation cell V and the total energy E are constant [47]. Other ensembles that can also be used are the canonical ensemble (NVT), wherein N, V and temperatue T are conserved, and the isothermal-isobaric ensemble (NPT) wherein N, system pressure P and T are conserved.

The temperature must also be considered during the simulation. Several techniques were developed to control the temperatue such as Nosé-Hoover thermostat [48], Langevin dynamics [49] and Berendsen thermostat [50].

In Langevin dynamics, the equations of motion is modified by a friction coefficient γ_i and a random force f_i

$$\dot{p_i} = F_i - \gamma_i p_i + f_i.$$

The dispersion σ_i of f_i is expressed as

$$\sigma_i^2 = \frac{2m_i\gamma_i k_{\mathrm{B}} T}{\Delta t},$$

where k_{B} is the Botlzmann constant.

The Berendsen thermostat is another method to re-scale the velocities of the atoms in the system. Here, an external heat bath is weakly coupled on the simulation system. The global coupling is expressed in terms of the temperature as

$$\left(\frac{dT}{dt}\right)_{bath} = \frac{T_o - T}{\tau_{\mathrm{T}}}$$

where τ_T is the time constant.

1.2.5 Periodic Boundary Conditions

In MD simulation, due to the limitations of the calculation power of computers and to save calculation time, small simulation box size is normally used. Periodic boundary conditions (PBCs) [51] are applied on the simulation box to approximate an infinitely large version of the system. This is accomplished by surrounding the simulation box with its replicates. By implementing PBCs, if one atom passes through one side of the box, it will come out on the opposite side. This makes it possible to simulate bulk materials using relatively small number of atoms.

1.3 Multi-beam Injection System

In a typical etching process of semiconductor materials in the industry, mixtures of several gases are used to generate the plasma. This produces several ions that can partipate in the etching process. However, in order to understand the individual role of the ions from the plasma during the etching process, multi-beam injection system was developed. Through this system, the etching of a surface with an ion beam that is composed of only one type of ion is possible.

Here, the multi-beam injection system is briefly discussed. The details of this system were discussed in detail in Ref. [52]. Figure 1.5 shows the schematic diagram of the system. In general, it is divided into four major parts: ion source, mass selecting magnet, beam line and reaction chamber. A Freeman-type ion source was used in this study. The ions were generated by supplying a mixture of Ar and the gas source (such as SF_6, NF_2 or C_2F_5) to the ion source. All the positive ions that were generated during the ionization are extracted by extraction electrodes with a high voltage of 25 kV. The ion of interest for study is selected using the mass selecting magnet. These ions are transported through the beamline and decelerated to the desired energy before injecting on the sample, which is located at the reaction chamber. A rotatable quadrupole mass spectrometer (QMS) in the

reaction chamber is used to measure the incident ion energy distribution. Several types of pumps such as turbo molecular pumps and cryogenic pumps were installed to maintain the system in UHV condition. The pressure at the reaction chamber is maintained at 10^{-8} Pa.

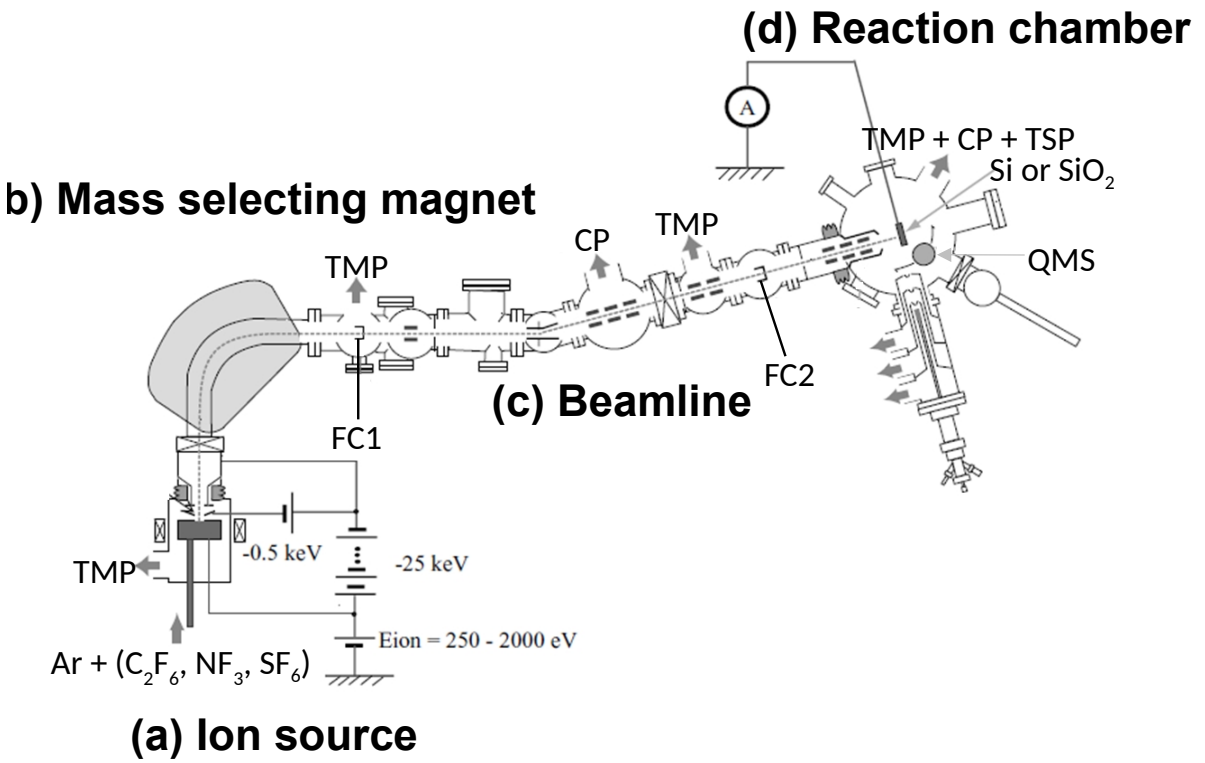

Figure 1.5: Schematic diagram of the multi-beam injection system. Is is divided into four parts: (a) ion source, (b) mass selecting magnet, (c) beamline, and (d) reaction chamber. TMP: turbo molecular pump, CP: cryogenic pump, TSP: titanium sublimation pump, FC: Faraday cup, QMS: quadropole mass spectroscopy.

During the etching, a metal mask with several gratings was used. After the ion bombardment, a contact profilometer (Dektak3ST®) was used to measure the etched depth. The experimental etching yield Y was calculated from the ion dose D, etched depth d, and the volume density of the material N.

$$Y = \frac{dN}{D}.$$

1.4 Objectives

In this research, classical MD simulation was employed to have a deeper understanding on the role of F atoms during the RIE of Si and SiO_2 materials. The simulated etching yields were compared with multi-beam injection system experimental results to confirm the validity of the simulation. The feasibility of using other gas sources such as I_2 in Si and SiO_2 etching applications was also studied. Moreover, the surface damage formation in PA-ALE of Si with Cl adsorption was explored.

This thesis is presented in the following manner. Chapter 2 describes the MD simulation of Si and SiO_2 RIE by $C_2F_5^+$ and NF_2^+ ions. In Chapter 3, RIE of Si and SiO_2 by SF_5^+ ion bombardment using a simple S-F system potential function is discussed. In Chapter 4, interatomic potential functions of Si, O and I systems were developed. The initial results of RIE of Si and SiO_2 materials with I^+ ion bombardment are discussed. Chapter 5 presents the MD study on the surface damage formation during PA-ALE of Si with chlorine adsorption. And finally, the over all conclusions are summarized in Chapter 6.

Chapter 2

Reactive ion etching of Si and SiO_2 by fluorine-rich ion species

2.1 Introduction

A continuous increase of the performance of electronic devices has been one of the major goals in the electronics industry. One of the major breakthroughs in recent flash memory technologies is the invention of three-dimensional (3D) NAND devices, wherein memory cells are stacked vertically, as 2D NAND flash memory devices have reached their scaling limit. A typical structure of this device is an alternating layer of polycrystalline-silicon (Si) electrodes and SiO_2 insulators [53]. Although 3D NAND flash memory devices are now widely available in the market, there remain several challenges in the fabrication processes of their future devices. One of the most critical challenges is the development of an efficient high-aspect-ratio (HAR) etching process for the fabrication of extremely deep channel holes with an aspect ratio of 100 or higher through the stacked layers [54].

Fluorine (F) atoms are known to be highly reactive on Si-based materials. These atoms can bond with Si, forming volatile products such as SiF_4 [10, 11, 55, 56], so fluorine-containing plasmas (or, more in general, halogen-containing plasmas) are often used for Si etching. SiO_2 is normally etched using fluorocarbon plasmas since carbon (C) atoms generated in such plasmas easily bond with oxygen atoms of the SiO_2 surface, producing

volatile products such as CO and thus increasing the etching yield [52]. However, on a Si surface, C atoms tend to deposit and can result in a very low etching yield [37, 52]. Therefore a fluorocarbon plasma is often used for selective etching of SiO_2 over Si. On the other hand, to achieve a one-step etching of Si and SiO_2 stacked layers, one needs a plasma that can etch both Si and SiO_2 with similar etching yields. This may be achieved by the use of highly energetic ion bombardment that can physically etch many different materials with similar etching yields.

Several studies were performed in the past on Si and SiO_2 etching by halogen/fluorine-based plasmas with the use of molecular dynamics (MD) simulation and beam experiments [34, 37, 38, 52, 57–69]. However, many of these studies focused on the effects of low energy ion incidence (with exceptions of, e.g., Ref. [52], [57] and [61]). For example, T. Shibano *et al.* [58] evaluated the etching yields of SiO_2 by F^+, CF^+, CF_2^+, and CF_3^+ ions with an ion incident energy of 80 - 350 eV, using beam experiments. Abrams *et al.* [37] performed MD simulations on Si etching with 50 – 200 eV CF_3^+ ion bombardment. Toyoda *et al.* [62] used beam experiments to evaluate the etching yields of Si and SiO_2 with 50 – 400 eV CF_2^+ and CF_3^+ ions. In such energy ranges, the etching yields of Si and SiO_2 may differ significantly, so that selective etching of SiO_2 over Si may be achieved. To achieve efficient Si- and SiO_2-stacked-layer etching, on the other hand, we need a less selective etching process with high etching yields, which may be realized by the use of highly energetic reactive ions. There have been only a limited number of publications on the evaluation of etching yields of highly energetic reactive ions. For example, Karahashi *et al.* published results of beam experiments for etching of Si [52] and SiO_2 [61] irradiated with 250 – 2,000 eV F^+ and CF_x^+ (x=1,2,3) ions. Since fluorine is highly reactive on a Si-based material and can form volatile molecules such as SiF_4, a supply of more fluorine atoms to a Si-based material surface with highly energetic ion bombardment should result in high etching yields.

The goal of this study is, therefore, to understand the etching mechanisms of highly energetic ions of reactive species, especially those containing multiple fluorine atoms, injected into surfaces of Si-based materials. In this article, we use classical MD simulations

to evaluate the etching yields of Si and SiO_2 by $C_2F_5^+$ and NF_2^+ ions and examine their surface reaction mechanisms. $C_2F_5^+$ and NF_2^+ ions are considered to be some of the major ionic species generated in plasmas formed with C_2F_6 and NF_3 gases. In the simulations presented in this article, the impact ion energy was varied from 500 to 2,000 eV.

2.2 Methodology

The MD simulation used in this study is based on a numerical simulation code presented in earlier studies [39, 67, 69, 70]. An outline of the simulation performed in this study is briefly described in this section. The model Si surface layer used in this study is a rectangular box of crystalline Si with a surface area of 3.26 x 3.26 nm^2 and an initial depth of 5.43 nm. Similarly, the model SiO_2 surface layer is a rectangular box of β–cristobalite SiO_2 with a surface area of 4.19 x 4.19 nm^2 and an initial depth of 6.98 nm. Periodic boundary conditions are imposed in the horizontal directions, so that the model surface layer (i.e., which we also call a "material" in this article) represents an infinitely wide surface layer. The rectangular cell where all simulation particles reside is called a "simulation cell". The depth of the material is chosen to ensure that the model material is sufficiently deep and no incident ion impact would affect the atoms located near the bottom of the layer. As the etching proceeds, more material atoms are added to the layer from the bottom, so that the model material remains deep enough during the entire simulation. The temperature of the model material is set at 300 K prior to each ion injection, which ensures that the surface is in thermal equilibrium with its environment at room temperature. The atoms in the bottom layer of the model material are set to be immobile during the simulation, which anchor the model material. $C_2F_5^+$ and NF_2^+ ions are selected as incident ions to be examined in this study, as mentioned in the previous section. The ion energy was varied from 500 to 2,000 eV. During the simulation, the equations of motion of each atom in the simulation cell, including incident ions, are numerically integrated based on inter-atomic potential functions of modified Stillinger-Weber type [39, 67, 69, 70]. The interatomic potential functions between an ion and

charge-neutral atoms are assumed to be the same as those among the corresponding charge-neutral atoms for the sake of simplicity. The Van der Waals (VdW) potential for each ion and material systems was was varied because the strength of the VdW is not the same for all atoms. For Si material, the VdW potential in equation 1.4 is reduced to 0.25% for $C_2F_5^+$ ion bombardment and no VdW potential was applied for NF_2^+ ion bombardment. In the case of SiO_2 material, the VdW potential was reduced to 0.75% and 0.25% for $C_2F_5^+$ and NF_2^+ ion bombardments, respectively.

The simulation is composed of cycles of ion bombardment and graduate cooling of the model material. The lateral position of an incident ion is selected randomly. Then the ion is injected from a position slightly above the surface, so that right after each simulation cycle starts, the incident ion starts to interact with surface atoms, i.e., hits the material surface. Once the ion hits the surface, the temperature of the material (or kinetic energy of all atoms constituting the material) increases rapidly. The material temperature is monitored during the simulation, which ensures that the (volume-averaged) material temperature is well below its melting point. When the material temperature is deemed too high, the simulation stops and more material atoms are added to the bottom of the current material, as mentioned above. After the material is thickened in this way, we restart the simulation with a new ion injection. After each ion injection, the simulation is performed under micro-canonical conditions for 300 femtoseconds. We have confirmed that the collision cascade dynamics of all atoms in the material layer typically ends within the first 300 femtoseconds after ion hits the surface under our simulation conditions.

Right after this micro-canonical simulation, a phase of gradual material cooling ensues. In this phase, the system is relaxed for 1,600 femtoseconds using Langevin thermostat [71, 72] and then cooled down to 300 K using Berendsen thermostat [73, 74] for the following 100 femtoseconds. This concludes a single simulation cycle for a total duration of 2 picoseconds. At the end of each simulation cycle, all desorbed species (species that are not bonded with the material) are counted as etched species and removed from the simulation cell. A new simulation cycle then starts with a new ion injection into the surface that has been modified by the previous simulation cycles. In our typical simulation, such

simulation cycles are repeated for 4,000 times (i.e., 4,000 ion impacts) to ensure that the system reaches steady state in the sense that macroscopic characteristics of the modified top material layer (e.g., chemical composition and the depth of the modified layer) and the average numbers of species desorbed and/or adsorbed per ion injection hardly change over many simulation cycles. In our system, 4,000 ion injections correspond to a dose of 3.78 x 10^{16} ions/cm^2 for the Si material and 2.28 x 10^{16} ions/cm^2 for the SiO_2 material.

2.3 Results and Discussions

2.3.1 Etching yields of Si and SiO_2

The etching yield of a surface for a specific atomic species is defined as the number of removed atoms of this species from the surface per incident ion. In this study, the etching yield always refers to the etching yield of Si, meaning that the number of Si atoms removed from a Si or SiO_2 surface per ion impact. When the system is in steady state, the etching yield for O of a SiO_2 surface must be twice as that of Si. However, one should note that, in the initial stage of etching when the surface layer is being modified by ion bombardment, the ratio of etching yields for Si to O of a SiO_2 surface may not be 1:2.

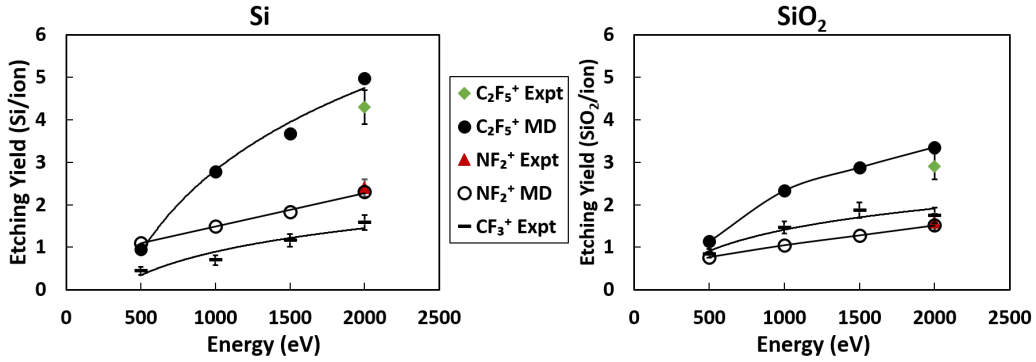

Figure 2.1: The etching yields of Si atoms for (a) Si and (b) SiO_2 surfaces by $C_2F_5^+$ and NF_2^+ ion bombardment as functions of ion incident energy obtained from MD simulation. The etching yields by CF_3^+ ions (experimentally obtained values from Refs. [52] and [61]) are also plotted for comparison. The curves are guides for the eye. The diamond with an error bar denotes the etching yield by 2,000 eV $C_2F_5^+$ ions and the triangle with an error bar denotes the etching yield by 2,000 eV NF_2^+ ions obtained from beam experiments.

The etching yields (for Si) of Si and SiO_2 surfaces by $C_2F_5^+$ and NF_2^+ ion bombardment obtained from the MD simulation are plotted as functions of ion incident energy in Fig. 2.1. The yields were obtained when the etching has reached a steady state in the sense that the etching yield no longer depend on the ion dose. Experimentally obtained etching yields are also plotted in the same figure for comparison, which indicates that the simulation results are consistent with experimental observations. Comparison of the simulation data of Fig. 2.1 with other preliminary experimental data (not given here) also suggests that the simulation data are in reasonable agreement with the experimental data. The experimental etching yields plotted here were obtained from ion beam experiments [52]. The experimentally obtained etching yields by CF_3^+ ions published in Refs. [52] and [61] are also plotted as references.

It is seen that the etching yield of a Si surface is higher than that of a SiO_2 surface in general for both $C_2F_5^+$ and NF_2^+ ion injections. This is because the Si–Si bond has a lower bond energy (2.3 eV) than the Si–O bond (4.2 eV). The etching yields by $C_2F_5^+$ ion bombardment on both Si and SiO_2 surfaces are higher than those by NF_2^+ ion bombardment. These observations are especially true at a higher ion incident energy of 1,000 – 2,000 eV, where physical sputtering effects are stronger than chemical sputtering effects. At 500 eV, the etching yields by $C_2F_5^+$ and NF_2^+ ions are almost the same even though $C_2F_5^+$ ions contain more F atoms for both surfaces. This is because, at low energy, an amorphous fluorinated C film is deposited on the surface, thus, hinders the etching [60, 61, 75].

It is also seen that the etching yields of Si and SiO_2 surfaces by $C_2F_5^+$ ions are much higher than those by CF_3^+ ions for the same ion incident energy. The etching yields of Si by NF_2^+ ions are also higher than those by CF_3^+ ions despite the fact that an NF_2^+ ion carries fewer F atoms than a CF_3^+ ion. The results show that NF_2^+ and $C_2F_5^+$ ions are good candidates for one–step processes for HAR etching applications.

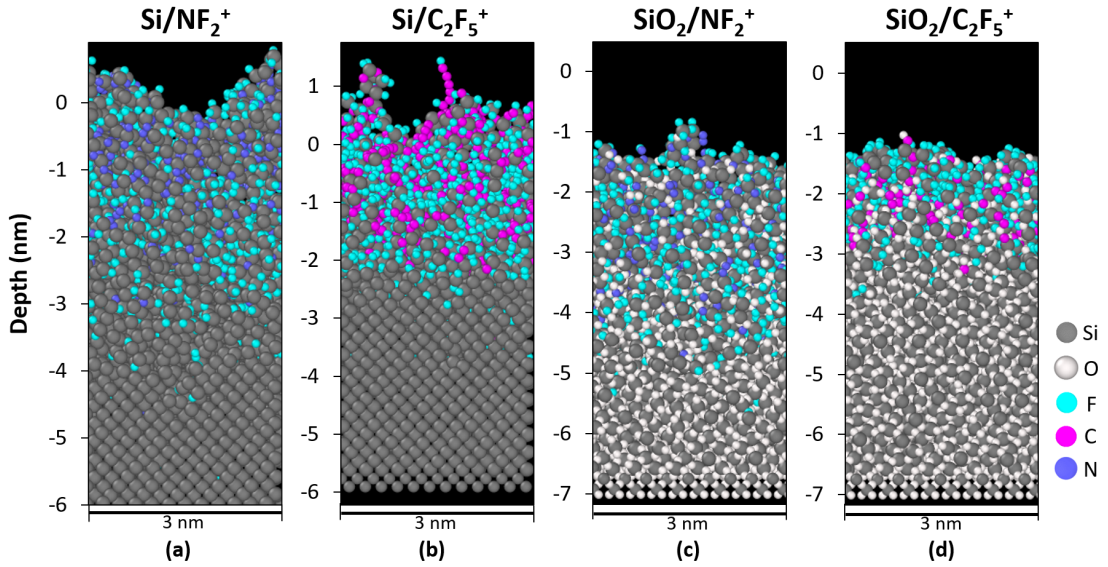

Figure 2.2: Snap shots of Si surface layers subject to (a) NF_2^+ and (b) $C_2F_5^+$ ion beams and SiO_2 surface layers subject to (c) NF_2^+ and (d) $C_2F_5^+$ ion beams at ion doses of (a) 7.98 x 10^{15} cm^{-2}, (b) 4.96 x 10^{15} cm^{-2}, (c) 7.96 x 10^{15} cm^{-2}, and (d) 2.96 x 10^{15} cm^{-2}, respectively, obtained from MD simulation. The ion incident energy is 500 eV.

2.3.2 Evaluation of mixing layers

Snapshots of Si and SiO_2 surface layers after 500 eV NF_2^+ and $C_2F_5^+$ ion bombardments are presented in Fig. 2.2, taken at the onset of steady state etching with an ion dose of around 2.96 – 7.98 x10^{15} ions/cm^2. The figure shows that a mixing layer, i.e., a layer where incident atoms are mixed with surface atoms, is formed on each material surface. It is seen in Fig. 2.2 that significant fluorination of the surface occurs in these layers.

The thickness of each mixing layer at the onset of steady state etching is plotted as a function of the ion incident energy in Fig. 2.3. Here, the thickness of a mixing layer is defined as the thickness of a layer where the atomic concentration of F atoms is higher than 5% of its peak value. It is observed that the thickness gradually increases with increasing ion incident energy. The mixing layers formed by NF_2^+ ion bombardment is thicker on both Si and SiO_2 materials than those by $C_2F_5^+$ ion bombardment with the same ion incident energy. Given the same ion incident energy, each F atom of an incident NF_2^+ ion has higher kinetic energy than that of an incident $C_2F_5^+$ ion. This enables the F atoms of NF_2^+ ions to penetrate deeper into the material at impact, resulting in a thicker

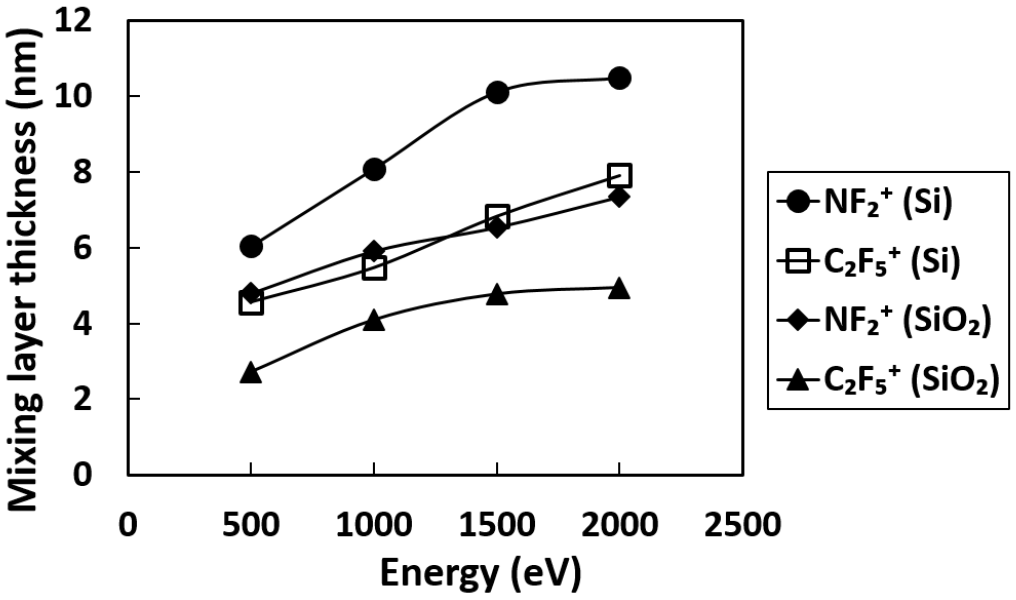

Figure 2.3: The mixing layer thicknesses formed in Si and SiO_2 materials as functions of ion incident energy at the onset of steady state etching obtained from MD simulation. The curves are guides for the eye. The legend indicates the incident ion species with the surface materials in parentheses.

mixing layer. When the ion incident energy is sufficiently high, the etching yield becomes high enough to prevent the growth of the mixing layer.

The depth profiles of the concentrations of Si, O, C, and N atoms in the materials at the onset of steady state etching are plotted in the cases of 500 eV and 2,000 eV incident ion energies in Fig. 2.4. Here, (a)-(d) show the depth profiles in Si, and (e)-(h) in SiO_2. The ion dose at which each set of depth profiles is taken is written above the set of profiles. The horizontal axis represents the atomic concentration in units of 10^{23} cm^{-3} and the vertical axis represents the height (or depth in negative values) in units of nm, measured from the top surface of the initial material (denoted as the origin). The positive value of the vertical axis indicates that the surface layer is expanded to a height above the original surface or deposition of new materials has taken place. It should be noted that the position of the origin and scale of each vertical axis differ from one another.

It is seen in the cases of 500 eV ion injections of (a), (c), (e), and (g) of Fig. 2.4, where the steady state etching is just about to start, that a significant amount of fluorine

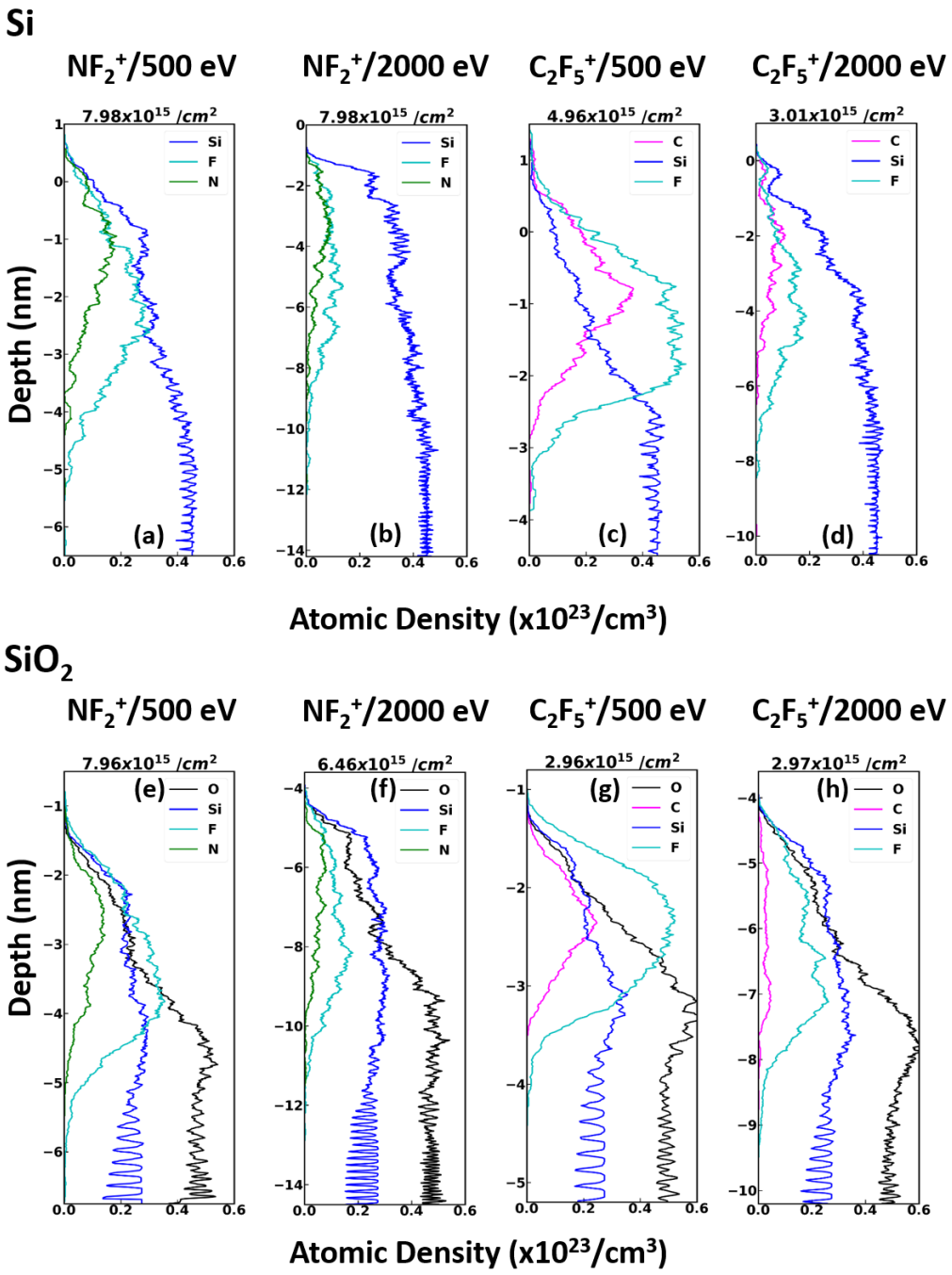

Figure 2.4: The depth profiles of the atomic concentrations at the onset of steady state etching, obtained from MD simulation, for a Si surface layer by (a) 500 eV NF_2^+, (b) 2,000 eV NF_2^+, (c) 500 eV $C_2F_5^+$, and (d) 2,000 eV $C_2F_5^+$ ions, and for a SiO_2 surface layer by (e) 500 eV NF_2^+, (f) 2,000 eV NF_2^+, (g) 500 eV $C_2F_5^+$, and (h) 2,000 eV $C_2F_5^+$ ions. The horizontal axis represents the atomic concentration in units of 10^{23} cm^{-3} and the vertical axis represents the height (or depth in negative values) in units of nm, measured from the position of the initial top surface (denoted as the origin) prior to ion bombardment. The ion dose at which the profiles are obtained (i.e., ion dose at the onset of steady state etching) is listed above each graph.

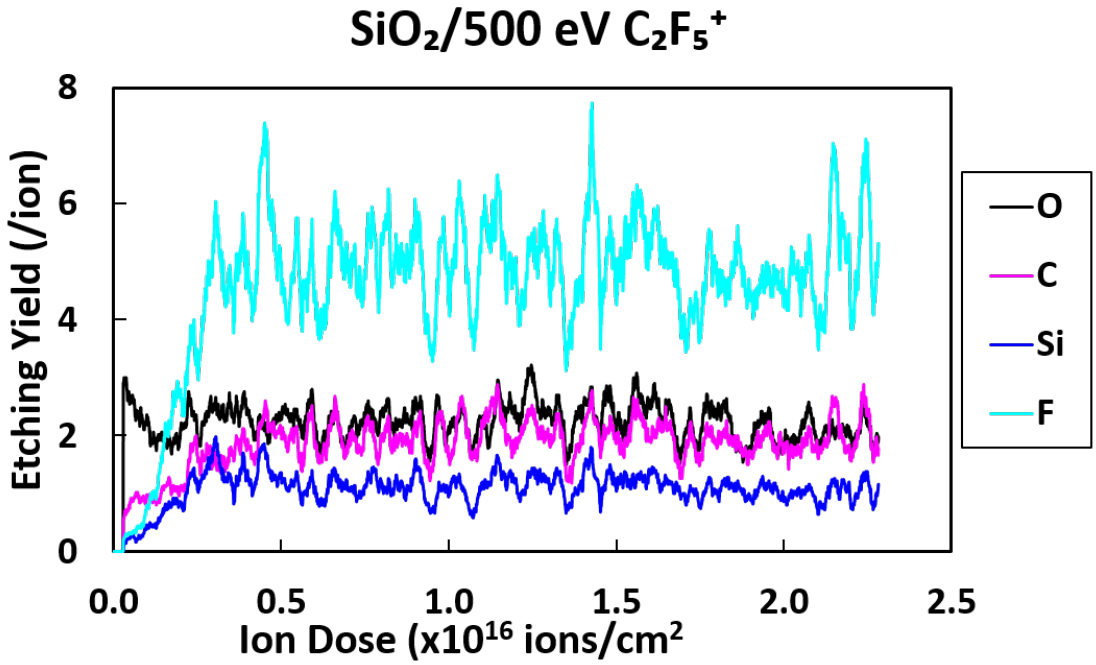

Figure 2.5: The etching yields for O, C, Si, and F species removed from a SiO_2 surface by 500 eV $C_2F_5^+$ ion incidence as functions of the ion dose, obtained from MD simulation. In this figure, the instantaneous etching yield for each atomic species (i.e., the number of atoms removed from the surface at each ion injection) measured in MD simulation is averaged over a small ion dose of 5.7×10^{12} ions/cm^2 around each ion dose to smooth the yield curve.

is accumulated near the top surface in the sense that the F density is nearly the same as, or even higher than, the Si density. On the other hand, in the cases of 2,000 eV ion injections of (b), (d), (f), and (h), the F density is lower (or much lower in some cases) than the Si density. These observations suggest that, at lower ion energy, etching is more dependent on chemical reactions of F atoms terminating Si bonds, whereas at higher ion energy, physical sputtering dominates the etching process.

It should be also noted that the atomic-density ratios of Si to O near the top SiO_2 surfaces shown in Fig. 2.4 are close to unity, indicating that there is a preferential removal of O atoms from the surface in the beginning of the etching process. This is also consistent with observation shown in Fig. 2.5, where the etching yields for all desorbed/sputtered species from the surface are shown as functions of ion dose in the case of SiO_2 etching by 500 eV $C_2F_5^+$ ions. The conditions of Fig. 2.5 correspond to those of Fig. 2.4(g). It is seen that the etching yield for O is much higher than twice of the etching yield of Si when the

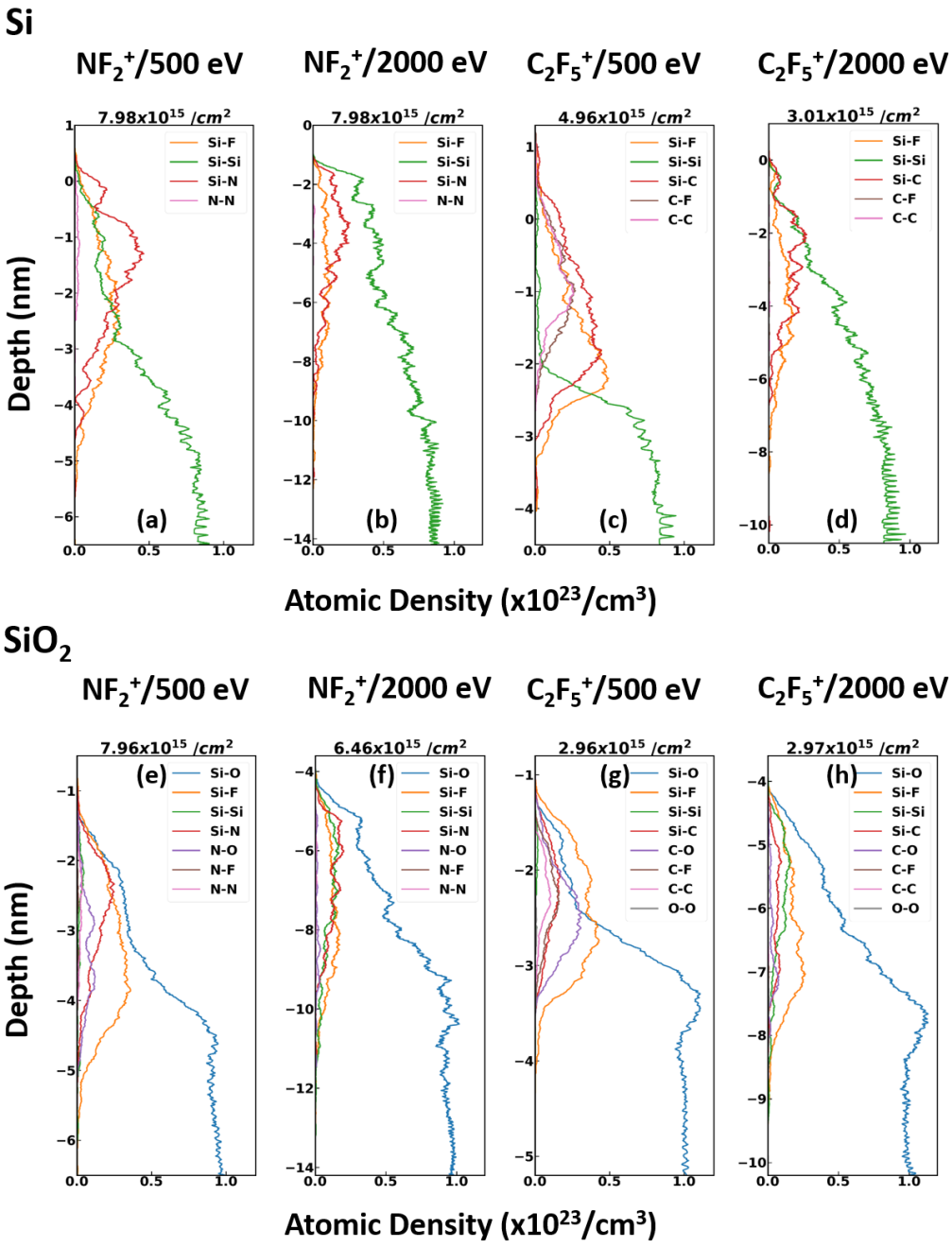

Figure 2.6: Bond distributions at the onset of steady state etching, obtained from MD simulation in Si surface layers for (a) 500 eV NF_2^+, (b) 2,000 eV NF_2^+, (c) 500 eV $C_2F_5^+$, and (d) 2,000 eV $C_2F_5^+$ ions and in SiO_2 surface layers for (e) 500 eV NF_2^+, (f) 2,000 eV NF_2^+, (g) 500 eV $C_2F_5^+$, and (h) 2,000 eV $C_2F_5^+$ ions. Here (a)-(h) correspond to (a)-(h) of Fig. 2.4. The horizontal axis represents the bond concentration in units of 10^{23} cm^{-3} and the vertical axis represents the height (or depth in negative values) in units of nm, measured from the position of the initial top surface (denoted as the origin) prior to ion bombardment. The ion dose at which the profiles are obtained (i.e., ion dose at the onset of steady state etching) is listed above each graph.

ion dose is small. A similar preferential sputtering of O atoms at an early stage of SiO_2 etching is observed as well in the case of NF_2^+ ion etching. It is also seen in Fig. 2.5 that etching reached steady state after an ion dose of around 3 x 10^{15} cm^{-2}, when an average etching yield for each species no longer changes.

The bond distributions of Si and SiO_2 materials are plotted in Fig. 2.6, whose (a)-(h) correspond to (a)-(h) of Fig. 2.4. In this figure, the densities of (pairwise) single bonds (such as Si-Si, Si-C, Si-O, Si-F, C-O, N-O, etc.) are plotted as functions of the depth. The densities of any higher-order bonds (such as double bonds) are negligibly small compared with those of single bonds and therefore not plotted here. It is seen that, in the case of low ion incident energy (500 eV), the density of Si-F bonds is typically higher than those of other Si bonds (i.e., bonds stemming from a Si atom) and comparable with the density of the material bonds (i.e., Si-Si bonds of a Si material or Si-O bonds of a SiO_2 material.) This is consistent with our observation in Fig. 2.4, where the top surfaces are highly fluorinated and many Si bonds are terminated by F atoms. The opposite trend is observed at 2,000 eV, wherein the density of the material bonds (Si-Si or Si-O) is much higher than that of Si-F bonds. This is because, as discussed earlier, a large number of material atoms are removed together with F atoms due to the high etching yield and therefore the density of remaining F atoms is relatively small.

Another evident observation is that, in the case of 500 eV $C_2F_5^+$ ion incidence on a Si surface, the densities of Si-C, C-F and C-C bonds are high, indicating that C atoms are deposited on the top surface and form an amorphous C layer containing Si and F. It is also seen that a similar C layer is about to be formed on the SiO_2 surface in the case of 500 eV $C_2F_5^+$ ion incidence. Such C layers hinder etching [60, 61, 75], which also explains the low etching yields of Si and SiO_2 materials by 500 eV $C_2F_5^+$ ion incidence, as discussed in Section 2.3.1.

We now also compare the cases of SiO_2 etching by $C_2F_5^+$ and NF_2^+ ion injections at low incident energy (500 eV). It is seen that the density of Si-O bonds on the surface is slightly lower in the case of $C_2F_5^+$ ion incidence than NF_2^+, whereas C-O bonds are also formed in the case of $C_2F_5^+$ ion incidence. This supports our earlier discussion in Section

2.3.1 that C atoms from $C_2F_5^+$ ions break Si-O bonds and form Si-C and C-O bonds. Once volatile CO_2 and CO are formed, they desorb from the surface and therefore the presence of C atoms promotes the etching of a SiO_2 surface. Similarly the formation of volatile NO_x by NF_2^+ ion incidence on a SiO_2 surface should promote the etching of a SiO_2 surface although the density of N-O bonds is seen to be very low in Fig. 2.6. Since all F, C, and N atoms may break Si-O bonds, the fact that more such reactive atoms are contained in a single incident ion in the case of $C_2F_5^+$ than NF_2^+ explains (at least partially) the higher etching yield of SiO_2 by $C_2F_5^+$ ions than by NF_2^+ ions observed in Fig. 2.1(b).

2.3.3 Desorbed species

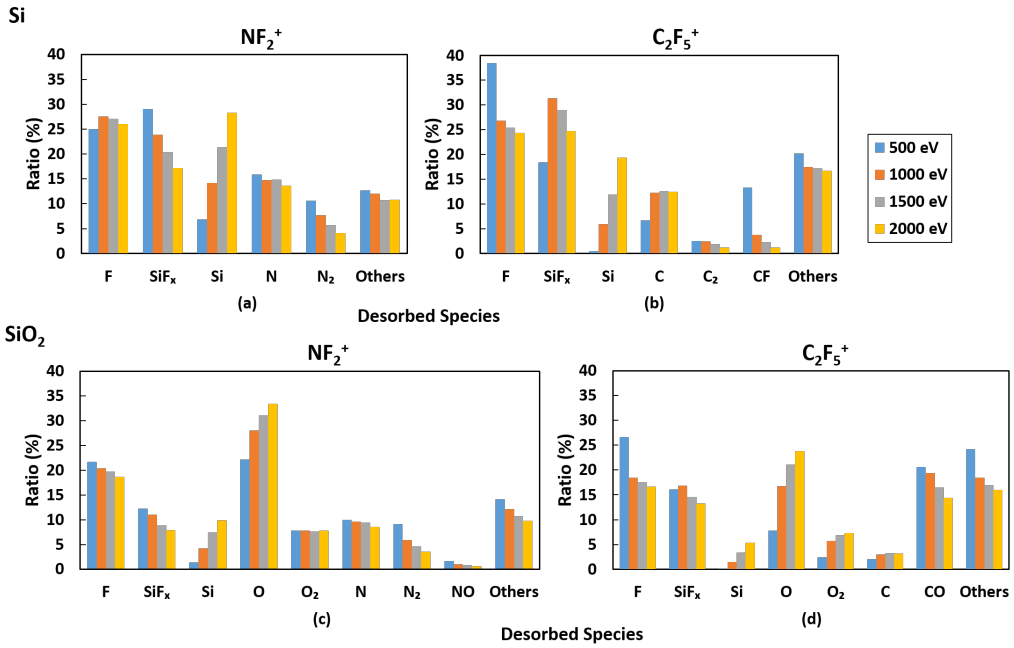

Figure 2.7: The ratios of desorbed species from (a) Si and (c) SiO_2 surfaces by NF_2^+ ion incidence and (b) Si and (d) SiO_2 surfaces by $C_2F_5^+$ ion incidence with various ion energies (indicated in different colors given in the legend). The desorbed species are listed in the horizontal axis labels, where SiF_x denotes SiF, SiF_2, SiF_3, or SiF_4 (excluding a Si atom).

The desorbed species or etched products were also studied, which may indicate chemical reactions taking place on the surface subject to reactive ion incidence. The distributions of F, SiF_x, Si, O, O_2, C, CO, N, N_2, NO and other sputtered/desorbed species observed in MD simulation of Si and SiO_2 etching by $C_2F_5^+$ and NF_2^+ ion incidence are

plotted in Fig. 2.7. The number of each species sputtered/desorbed from the surface per ion injection (i.e., etching yield) is counted in MD simulation and normalized by the total number of all sputtered/desorbed species per ion injection. This ratio (normalized etching yield) for each sputtered/desorbed species is plotted in percentage in Fig. 2.7. In this way, the relative shift among sputtered/desorbed species due to different incident ion species or energy can be seen clearly without being affected by the change in the absolute values of etching yields. The horizontal axis labels all sputtered/desorbed species. Here, SiF_x indicates radical species or a molecule of SiF, SiF_2, SiF_3, or SiF_4 (excluding a Si atom). The color indicates the ion incident energy. The material is Si for (a) and (b) and SiO_2 for (c) and (d). The incident ion species is NF_2^+ for (a) and (c) and $C_2F_5^+$ for (b) and (d), as indicated. Here the desorbed species are evaluated from the onset of steady state in each MD simulation to an ion dose of 3.78 x 10^{16} ion/cm^2 for a Si surface and 2.28 x 10^{16} ion/cm^2 for a SiO_2 surface, i.e., only in steady state.

It is seen that Si atoms are removed from the surfaces mostly by the formation of SiF_x (x = 1 - 4) or sputtering of monoatomic Si atoms. However, the amount of desorbed species in the form of SiF_x gradually decreases as the energy increases in general. This indicates that chemical reactions (such as bond breaking of Si by F atoms) are less important in etching at higher ion incident energy; more Si atoms (as well as O atoms in the case of a SiO_2 material) are removed by direct ion impact at higher ion incident energy. This is also reflected in the fact that the percentage of monoatomic Si atoms (as well as monoatomic O atoms in the case of SiO_2 etching) sputtered from the surface increases significantly with increasing ion incident energy.

One exception is the case of a Si material etching by 500 eV $C_2F_5^+$ ions, where the amount of desorbed SiF_x is smaller at 500 eV than that at other higher energies. This is because, as discussed in the preceding subsection, a fluorinated C layer is formed on the Si surface and there are more C atoms than Si atoms near the top surface under these conditions. Indeed the sputtering/desorption of CF is exceptionally high in this case, as seen in Fig. 2.7(c).

It is also seen in Fig. 2.7 that, in the case of $C_2F_5^+$ ion incidence, the total amount

of SiF_x (x = 1 - 4) desorption is larger than that of Si desorption. This is in contrast to the case of NF_2^+ ion incidence, where the amount of SiF_x (x = 1 - 4) desorption is comparable or even smaller than that of Si desorption, especially at higher ion incident energy. In the case of $C_2F_5^+$ ion incidence, ample supply of fluorine to the surface causes more termination of Si bonds by F atoms, which results in the removal of more Si from the surface due to chemical etching than physical sputtering. The termination of Si bonds by F atoms on the surface increases the chance of Si removal by energetic ion impact. These results shown here also explain why the etching yield is higher for $C_2F_5^+$ ions than NF_2^+ ions, as discussed in Section 2.3.1.

It is also observed in Fig. 2.7(d) that, in the case of SiO_2 etching by $C_2F_5^+$ ions, O atoms are removed mostly as CO and O, which is similar to what has been observed experimentally in Ref. [61], which shows that one of the major desorbed products is CO when a SiO_2 surface is etched by CF_x (x = 1 - 3) ion beams. It is also seen that the ratio of CO as sputtered/desorbed species decreases and that of O increases with increasing ion energy. Since CO is formed by chemical reactions in the mixing layer, the amount of desorbed CO decreases as the ion incident energy increases and the nature of etching becomes more physical than chemical.

In the case of SiO_2 etching by NF_2^+ ions shown in Fig. 2.7(c), O atoms are removed mainly as monoatomic O atoms and, to a less extent, O_2 molecules. Desorption of NO is much lower. In this case, Si may be removed via chemical etching by forming SiF_x (x = 1 - 4) but O atoms seem to be removed mostly by physical sputtering.

The detailed distributions of desorbed SiF_x (x = 1 - 4) are plotted in Fig. 2.8, which may facilitate a better understanding of the role of F atoms during Si and SiO_2 etching by NF_2^+ or $C_2F_5^+$ ions. As in Fig. 2.7, the number of each SiF_x species desorbed from the surface is normalized by the total number of all desorbed SiF_x (x = 1 - 4) species and plotted in percentage in Fig. 2.8. As in Fig. 2.7, the desorbed species are evaluated from the onset of steady state to an ion dose of 3.78 x 10^{16} ion/cm^2 for a Si surface and 2.28 x 10^{16} ions/cm^2 for a SiO_2 surface. The color indicates the ion incident energy. The material is Si for (a) and (b) and SiO_2 for (c) and (d). The incident ion species is NF_2^+

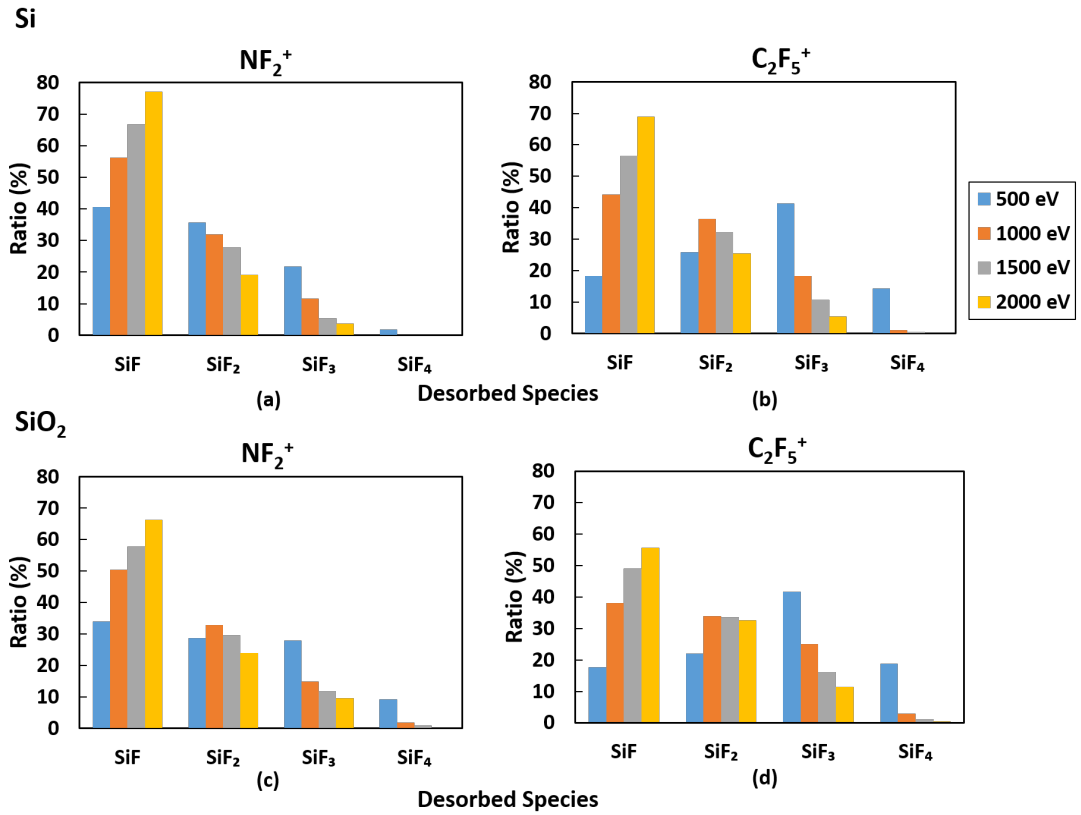

Figure 2.8: The ratios of desorbed species in the form of SiF, SiF_2, SiF_3, or SiF_4 from (a) Si and (c) SiO_2 surfaces by NF_2^+ ion incidence and (b) Si and (d) SiO_2 surfaces by $C_2F_5^+$ ion incidence with various ion energies (indicated in different colors given in the legend). Here the sum of all desorbed species in the form of SiF_x (x = 1 - 4) constitutes 100%.

for (a) and (c) and $C_2F_5^+$ ion for (b) and (d).

It is seen in all cases that the formation of SiF_4, the most volatile species among them, is almost negligible except at 500 eV. At each incident energy, the amount of desorbed species is in general the highest for SiF and the lowest for SiF_4 with SiF, SiF_2, SiF_3 and SiF_4 in descending order, except for the cases of 500 eV $C_2F_5^+$ ion incidence on both Si and SiO_2 surfaces. This indicates that, with a limited supply of F atoms, a Si atom is less likely to be bonded with more F atoms when it is sputtered off from the surface by energetic incident ions. In the case of 500 eV $C_2F_5^+$ ion incidence on both Si and SiO_2 surfaces, on the other hand, the desorbed species are seen to be listed as SiF, SiF_2, SiF_3 in ascending order of the amount of desorption (except for SiF_4). In other words, with an ample supply of fluorine to the surface, the removal of more Si from the surface is due to chemical etching, as discussed above.

With increasing ion incident energy, the amount of desorbed Si (shown in Fig. 2.7) and that of SiF increase, whereas the amount of SiF_3 and that of SiF_4 decrease in all four cases of Figs. 2.7 and 2.8. As the ion incident energy increases, there are fewer F atoms remaining on the surface, so that the probability for a Si atom to bond with a larger number of F atoms decreases. The amount of desorbed SiF_2 is also seen to decrease in general with increasing ion incident energy except for some cases at 500 eV ion incident energy.

2.4 Conclusions

In this study, classical MD simulation is performed to emulate interactions between incident energetic ion species with relatively large numbers of F atoms and a Si or SiO_2 surface. The etching yield of a Si or SiO_2 surface by such ions at high incident energy is typically high, so that etching by plasmas generated from NF_3 or fluorocarbon with high bias voltages is considered effective for a one-step etching process of stacked Si and SiO_2 layers. The etching yields of Si and SiO_2 by NF_2^+ or $C_2F_5^+$ ions were evaluated by MD simulation as functions of ion incident energy over the range between 500 eV and 2,000 eV and found to be consistent with experimentally observed etching yields. The simulation results show that the etching yield increases with ion incident energy and its ion energy dependence is especially strong in the case of $C_2F_5^+$ ion incidence. Since a single impact of a $C_2F_5^+$ ion supplies more F atoms to the surface than that of an NF_2^+ ion and F atoms tend to chemically etch Si and SiO_2, $C_2F_5^+$ ions may promote more chemical etching of the surface than NF_2^+ ions. On the other hand, C deposition on the surface may impede the efficiency of surface etching. As shown in Fig. 2.1, indeed, for a Si or SiO_2 surface, its etching yields by NF_2^+ and $C_2F_5^+$ ions are nearly the same at an ion incident energy of 500 eV, whereas the etching yield by $C_2F_5^+$ ions is much larger than that by NF_2^+ ions at 2,000 eV. Such ion energy dependence suggests that the chemical enhancement of the etching yield remains pronounced even at high ion incident energy if more fluorine is supplied to the surface. However, as seen in the desorbed products of Figs. 2.7 and 2.8, the higher

the ion incident energy is, the more physical the nature of etching becomes. As the ion incident energy increases, Si atoms are removed from the surface more in the form of Si or SiF and the amount of desorbed Si atoms bonded with more F atoms such as SiF_3 or SiF_4 decreases.

In a plasma etching process to create HAR structures such as HAR deep holes, the bottoms of such structures are exposed only to the gas-phase species whose angle of incidence is along the line of sight connecting the bottoms and gas-phase plasma. Therefore incident species reaching the bottom are essentially only energetic ions from the plasma while charge-neutral radicals, whose angles of incidence follow a wide angular distribution, are typically adsorbed near the entrance of a HAR structure and hardly reach its bottom. Therefore, etching reactions at the bottoms of HAR structures must be nearly the same as those of ion-surface interactions examined in this study. However, some desorbed species may stick to the side walls, which may affect the overall etching efficiency of HAR structures. Transport of desorbed species in HAR structures formed in stacked Si and SiO_2 layers is beyond the scope of the present work and will be the subject of a future study.

Chapter 3

Reactive ion etching of Si and SiO_2 by SF_5^+ ions

3.1 Introduction

Plasma-assisted deposition and etching processes [76–79] are some of the most widely used and essential processes in semiconductor manufacturing. As planar structures of memory devices shift to three-dimensional (3D) structures, new challenges have emerged especially in etching processes. One example is the manufacturing processes of 3D NAND flash memory devices [5], whose typical structure is composed of alternating layers of polysilicon (poly-Si) or silicon nitride (Si_3N_4), and silicon oxide (SiO_2) [53, 80, 81]. Memory cells are constructed by fabricating channel holes through these layers. To achieve higher memory capacity, the memory cell is required to have more such layers. Consequently, the aspect ratio of the holes also increases as the capacity of 3D NAND flash memory devices increases. Then, this imposes several difficulties in the etching processes such as twisting, bowing, undercut, contact-edge-roughening, and aspect-ratio-dependent etching [31, 33]. In the past, selectivity was the priority during etching and most studies were focused on this topic. However, for high-aspect-ratio (HAR) etching [82, 83] to form deep holes for 3D NAND flash memory applications with a short process time, the selectivity between the stack layer materials is undesired. Instead, fast and efficient etching

of both poly-Si and SiO_2 layers is favored. Moreover, the application of HAR etching is not only limited to 3D NAND flash memory manufacturing, but also has significant importance for other microelectronic devices. Thus, there is a demand in addressing the problems in high aspect ratio (HAR) etching in general.

The choice of gases for a plasma discharge is one of the most essential factors affecting the etching yields and profiles of the channel holes. The etching yield is defined as the average number of removed atoms from the surface for each ion impact. Earlier studies demonstrated that halogen gases such as fluorine (F), chlorine (Cl), and bromine (Br) are highly effective in etching Si-based materials [10, 61, 62, 65, 69, 84]. Recently, several studies about HAR etching of Si-based material using halogen gases were published. Iwase *et al.* used HBr/fluorocarbon-based gas with nitrogen addition to achieve a single-step etching process of poly-Si/SiO_2 [53] and SiN/SiO_2 stacks [81]. Computational methods were also utilized to study the HAR etching profiles of Si and SiO_2 materials. For example, Huard *et al.* used a Monte Carlo feature-profile model (MCFPM) to predict the etch-profile evolution of Si etched with Ar/Cl_2 plasmas [31]. Huang *et al.* used the same model for SiO_2 etching with $Ar/C_4F_8/O_2$ [33]. Tinacba *et al.* also investigated the effects of energetic incident ions with high F content such as $C_2F_5^+$ and NF_2^+ on the yields of Si and SiO_2 in reactive ion etching (RIE) via molecular dynamics (MD) simulation [85].

SF_6 gas contains a large amount of fluorine and can be an efficient etchant for HAR etching. Several studies on plasma etching of Si and SiO_2 materials using plasmas generated from gas mixtures of SF_6 have been reported. Such plasma discharges are typically formed from mixtures of SF_6 with other gases such as Ar, O_2, CHF_3 and CF_4 [78, 86–92]. O_2 is normally added to increase the anisotropy by side-wall passivation [93, 94]. Major results have shown that a higher SF_6-to-O_2 ratio in Si creates a mask undercut because the amount of O atoms is not enough to passivate the side walls [91, 92].

The goal of this study is to understand the etching reactions of Si and SiO_2 by an SF_6 plasma. To be more specific, we focus on the interaction of Si and SiO_2 surfaces with incident energetic SF_5^+ ions, which are likely to be generated in an SF_6 plasma. To achieve this goal, we performed molecular dynamics (MD) simulation to simulate energetic SF_5^+

ion impact on Si and SiO_2 surfaces and compared the results with experimental data obtained from a mass-selected ion beam system [52].

3.2 Outline of the MD Simulation

MD simulation was used to study the interaction of SF_5^+ ions with Si and SiO_2 surfaces. The details on how MD simulation can be used to study ion-beam and surface interactions are presented in earlier references [38, 39, 67, 69, 85]. In this study, modified Stillinger-Weber (SW) potential functions [41] were employed to describe the interactions among all the atoms. The interatomic potential models for Si, O, and F atoms were reported in previous studies [38, 39]. The potential function models involving sulfur (S) atoms will be discussed in the following section. Equation 1.4 was used to include the Van der Waals interactions in the system.

The simulation started with a pristine Si (100) or SiO_2 (100) surface of a rectangular model material. The surface area of the Si and SiO_2 model materials were 3.26×3.26 nm^2 and 4.19×4.19 nm^2 and their initial thicknesses were typically 5.43 nm and 6.98 nm. Periodic boundary conditions were imposed in the horizontal directions (i.e., x and y directions) to emulate an infinitely wide surface. In the direction of depth (i.e., negative z direction), the last two monolayers of atoms at the bottom of the material were rigidly fixed and served as an anchor to prevent the simulation cell from drifting. The model material is set to be large enough, such that no moving atom during the simulation would reach or pass through the bottom layer of the model material. If an atom passes through the bottom layer, the simulation will be re-performed with a thicker material model with added bottom layers. The initial temperature of the material was set to 300 K.

The MD simulation is composed of cyclic SF_5^+ ion bombardment on the surface. In each cycle, one SF_5^+ ion is directed perpendicular to the surface. The position of each ion impact is selected randomly. One cycle lasts for 2,200 fs for Si (2,000 fs for SiO_2), which may be divided into three stages. The first 500 fs is the constant total-energy calculation wherein the temperature of the model material increases due to the fast transfer of kinetic

energy of the impacting ion to the material's atoms. After this first stage, all the particles removed from the surface are recorded. The system is artificially cooled by the Langevin thermostat in the next 1,600 fs (1,400 fs for SiO_2). The Berendsen heat bath is then applied in the last 100 fs until the system temperature reaches its initial value of 300 K. This cycle is repeated typically 4,000 times with the same material in each simulation, such that the roughness and modification of the chemical composition of the material surface are formed self-consistently with the continuous ion bombardment. As mentioned above, if the depth of the model material is reduced sufficiently, new layers of atoms are added to the material from the bottom. In this study, the SF_5^+ ion energy was varied from 150 to 2,000 eV.

The MD simulation results were compared with experimental results obtained via multi-beam injection system [52]. The details of this system were discussed in detail in Ref. [52]. With the aid of this system, the interactions of a specific ion or specie with a surface under an ultrahigh vacuum (UHV) condition can be investigated.

3.3 Simplified Interatomic potential model for S

In this section, we develop a simplified atomic potential model for S that represents molecular moieties or molecules SF_n ($n \leq 6$) approximately. We intend to limit the role of S atoms in our MD simulation only to "carrier" atoms that can take multiple F atoms to the surface simultaneously when F atoms are injected into a Si or SiO_2 surface in the form of SF_5^+ ions. Except for the fact that the S atom represented by this interatomic potential model has its own atomic radius and mass, it is assumed that it does not react with Si, O, or other S atoms. In other words, we essentially eliminated the chemical properties of S in our model, except that it can be bonded with up to 6 F atoms around it. One of the main goals of this research is to clarify to what extent the simultaneous injection of chemically reactive F atoms into a Si or SiO_2 surface accounts for the observed surface etching reactions. In what follows, we by no means intend to develop realistic interatomic potential models of S that react with Si, O, F, and other S atoms in this study. Indeed

S exhibits rather complex reactions with Si, O and F. The classical modeling of realistic interatomic potential functions for S reacting with Si, O, F, and other S atoms is beyond the scope of the present work.

In classical molecular dynamics simulations, the interactions among atoms are described by pre-determined interatomic potential function Φ, which is in general a function of the position of all atoms. For a system with N atoms, the total potential energy Φ is given by

$$\Phi = \Phi(r_1, r_2, r_3, r_4, ..., r_N)$$

where r_i (i = 1, 2, ..., N) is the position of the i-th atom and the total number of atoms used in the simulation is assumed to be N. The total potential may be expanded using cluster expansion as

$$\Phi = \sum_i V_1(r_i) + \sum_{i<j} V_2(r_i, r_j) + \sum_{i<j<k} V_3(r_i, r_j, r_k) + ...$$

where V_1 is the one-body term, which is caused by external forces and can be considered zero in this study. The function V_2 is the two-body term and V_3 is the three-body term, and so on. However, according to Stillinger and Weber [41], the total potential energy may be approximated by the sum of V_2 and V_3 if the atomic bonds are strong and highly directional. The calculations of the two- and three-body potential functions in this study are based on previously published work [38, 39]. Because the potential functions depend only on the relative positions, we now write

$$V_2(r_i, r_j) = V_2(|r_i - r_j|)$$

and assume that it depends on the interatomic distance r (r > 0) in the following manner;

$$V_2(r) = ar^{-2q} \exp\left(\frac{2d}{r - r_c}\right) - br^{-q} \exp\left(\frac{d}{r - r_c}\right), \text{ if } r > r_c, \tag{3.1}$$

where a, b, d, q, and r_c are parameters. The parameter r_c is the cut-off length, i.e., V_2 = 0 if $r \geq r_c$.

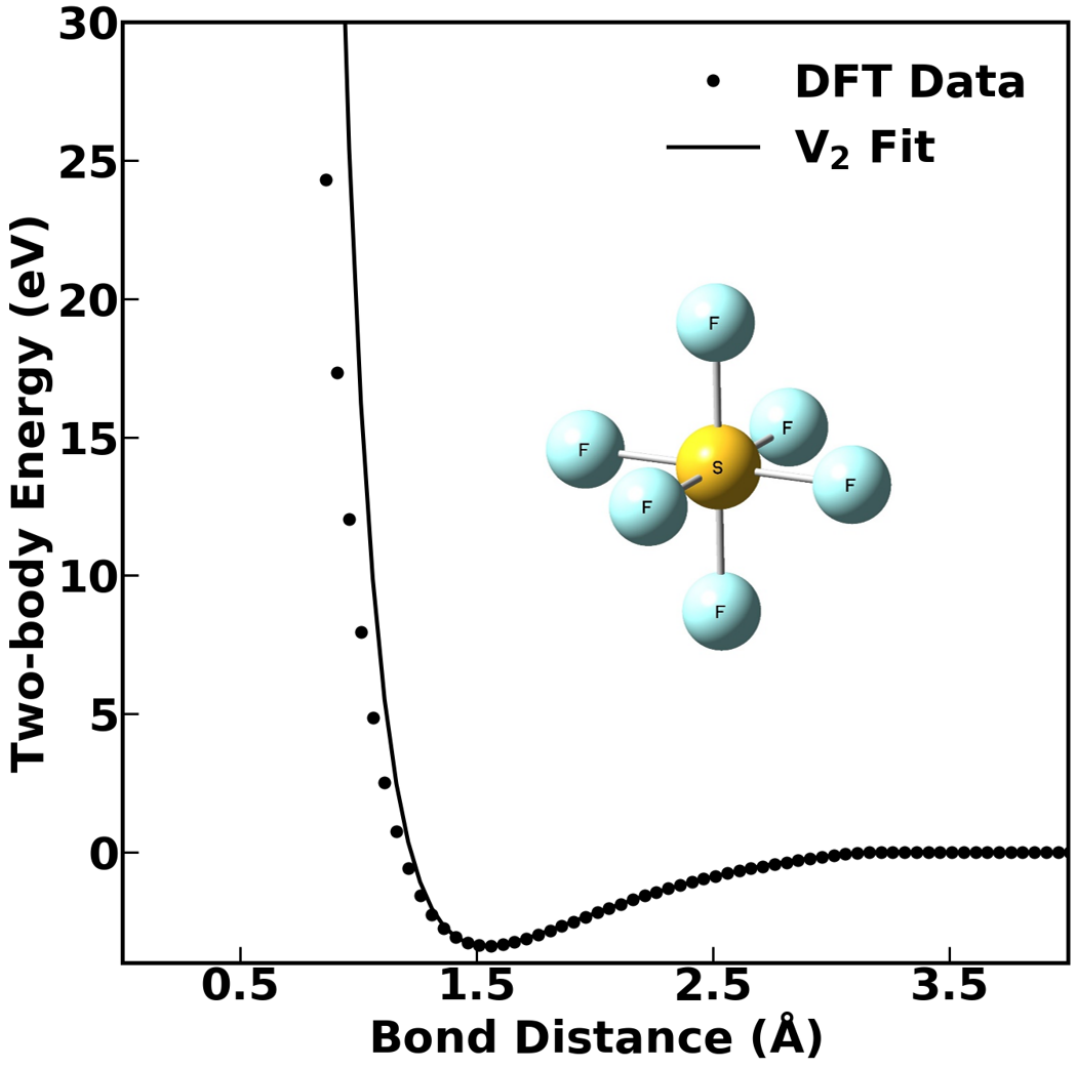

Figure 3.1: S-F two-body potential energy as a function of the bond distance. The data points are obtained from DFT calculations and the curve is obtained from V_2 fitting. The inset figure shows the SF_6 molecule configuration used in the DFT calculations.

Table 3.1: Calculated parameter values for the two-body potential (V_2) of S-F bond.

Parameters	Values	Units
a	142.30	$(\text{eV})^{2q}/\text{Å}$
b	43.96	$(\text{eV})^{q}/\text{Å}$
q	1.54	
d	2.50	Å
r_c	3.51	Å

Density-functional-theory (DFT) calculation using Gaussian 09 software [95] was performed to determine the two-body potential curve of S and F atoms using a stable SF_6 molecule. The calculation was conducted using B3LYP/6-311G. In the calculation, the S-F distances were simultaneously varied from 0.5 to 4 Å. The total energies of S and F atoms were subtracted from the total energy of an SF_6 molecule, which is then divided by the number of S-F bonds present in the SF_6 molecule. The final S-F potential curve was then adjusted to the published minimum bonding energy of -3.379 and S-F distance of 1.56 Å [96]. Equation (3.1) was fitted on the potential curve using the Levenberg-Marquardt fitting algorithm, as shown in Fig. 3.1. The horizontal axis corresponds to the S-F bond distance and the vertical axis corresponds to the two-body potential energy. The inset figure shows the geometry of the SF_6 molecule used in the calculation. The parameter values obtained from the fitting are listed in Table 3.1.

As mentioned above, we assume that S does not react with Si, O, or other S atoms in this study. Therefore, we use the Molière repulsive pair potential [97] to represent the S-Si, S-O, and S-S two-body interactions, i.e.,

$$V(r) = \frac{Z_1 Z_2 e^2}{4\pi\epsilon_o r}\left\{0.35\exp\left(\frac{-0.3r}{a}\right) + 0.55\exp\left(\frac{-1.2r}{a}\right) + 0.10\exp\left(\frac{-6.0r}{a}\right)\right\},$$

where Z_1 and Z_2 are the atomic numbers, e is the electric charge, ϵ_o is the electric constant, and r is the distance between the two atoms. The value of a is calculated from the Z_1 and Z_2 with the Bohr's radius ($a_o = 5.29177249 \times 10^{-11}$ m) as

$$a = 0.885 a_o (Z_1^{0.5} + Z_2^{0.5})^{-\frac{2}{3}}.$$

This means that the S-Si, S-O and S-S interactions are assumed to be only repulsive. The potential curves are plotted in Fig. 3.2. We assumed in this study that S does not react with Si or O for the sake of simplicity. This is based on our ex-situ experimental observation that no S remained on the Si or SiO_2 surface etched by an SF_5^+ ion beam. This observation is also consistent with an earlier study [98]. However, in reality, S is known to react with Si and O, forming e.g., SiS and SO_2. The creation of reactive potential functions for S is deferred to a future study.

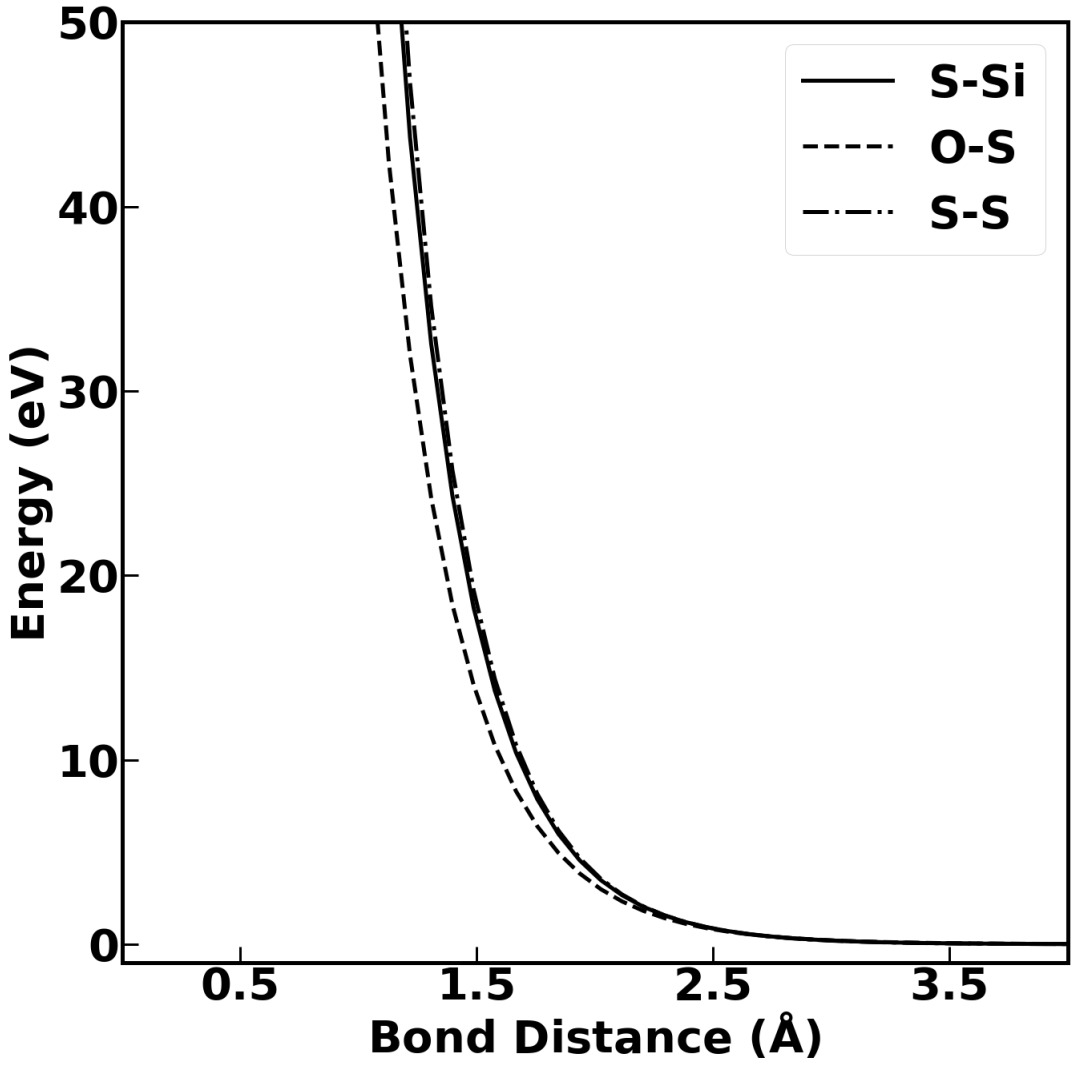

Figure 3.2: S-Si, Si-O and S-S two-body potentials obtained from Molière repulsive pair potential function used in this study.

The three-body potential function may be given by the following formula;

$$V_3(i,j,k) = h_{ijk}(r_{ij}, r_{ik}, \theta_{jik}) + h_{jik}(r_{ji}, r_{jk}, \theta_{ijk}) + h_{ikj}(r_{ki}, r_{kj}, \theta_{ikj}), \tag{3.2}$$

where $r_{ij} = |r_i - r_j|$ is the distance between the i-th and j-th atoms, and θ_{ijk} is the angle formed by the ij-bond (i.e., a bond between the i-th and j-th atoms) and kj-bond with the central atom at vertex being the j-th atom. The $h_{ijk}(r_{ji}, r_{jk}, \theta_{ijk})$ function is assumed to have the following form;

$$h_{ijk}(r_{ji}, r_{jk}, \theta_{ijk}) = k_{ijk}|\cos\theta_{ijk} - \Theta_{ijk}|^{\gamma_{ijk}} f_{ij}(r_{ij}) f_{jk}(r_{jk}), \tag{3.3}$$

where k_{ijk}, Θ_{ijk}, and γ_{ijk} are parameters that depend on the subscript ijk. Because of symmetry, we have $k_{ijk} = k_{kji}$, $\Theta_{ijk} = \Theta_{kji}$, and $\gamma_{ijk} = \gamma_{kji}$. The functions f_{ij} is a step-function-like smooth function that satisfies $f_{ij}(r) = 1$ if $0 < r \ll r_c$ and $f_{ij}(r) = 0$ if $r \geq r_c$ with r_c being the cut-off length between the i-th and j-th atoms. More specifically, we define f_{ij}, using the two-body function of $V_2(r)$ defined in Eqn. (3.1), which also depends on the species of i-th and j-th atoms, as

$$f_{ij}(r) = \begin{cases} 1, & r \leq r_{\min}, \\ V_2(r)/V_{2\min}, & r_{\min} < r < r_c, \\ 0, & r > r_c, \end{cases}$$

where $r_{\min}$ is the bond distance between the i-th and j-th atoms at the minimum bond energy $V_{2\min}$ of $V_2(r)$. Figure 3.4 shows the function $f_{\mathrm{SF}}(r)$ as a function of the distance r between S and F atoms.

For cases where one of the arguments of the function r_{ji} or r_{jk} is greater than or equal to the cut-off distance r_c, h becomes zero. If the cut-off length is sufficiently small, then only one of the three h functions forming the three-body potential V_3 of Eqn. (3.2) is nonzero for the stable SF_6 molecule shown in Fig. 2, which makes the fitting of Eqn. (3.3) to DFT calculation data more straightforward.

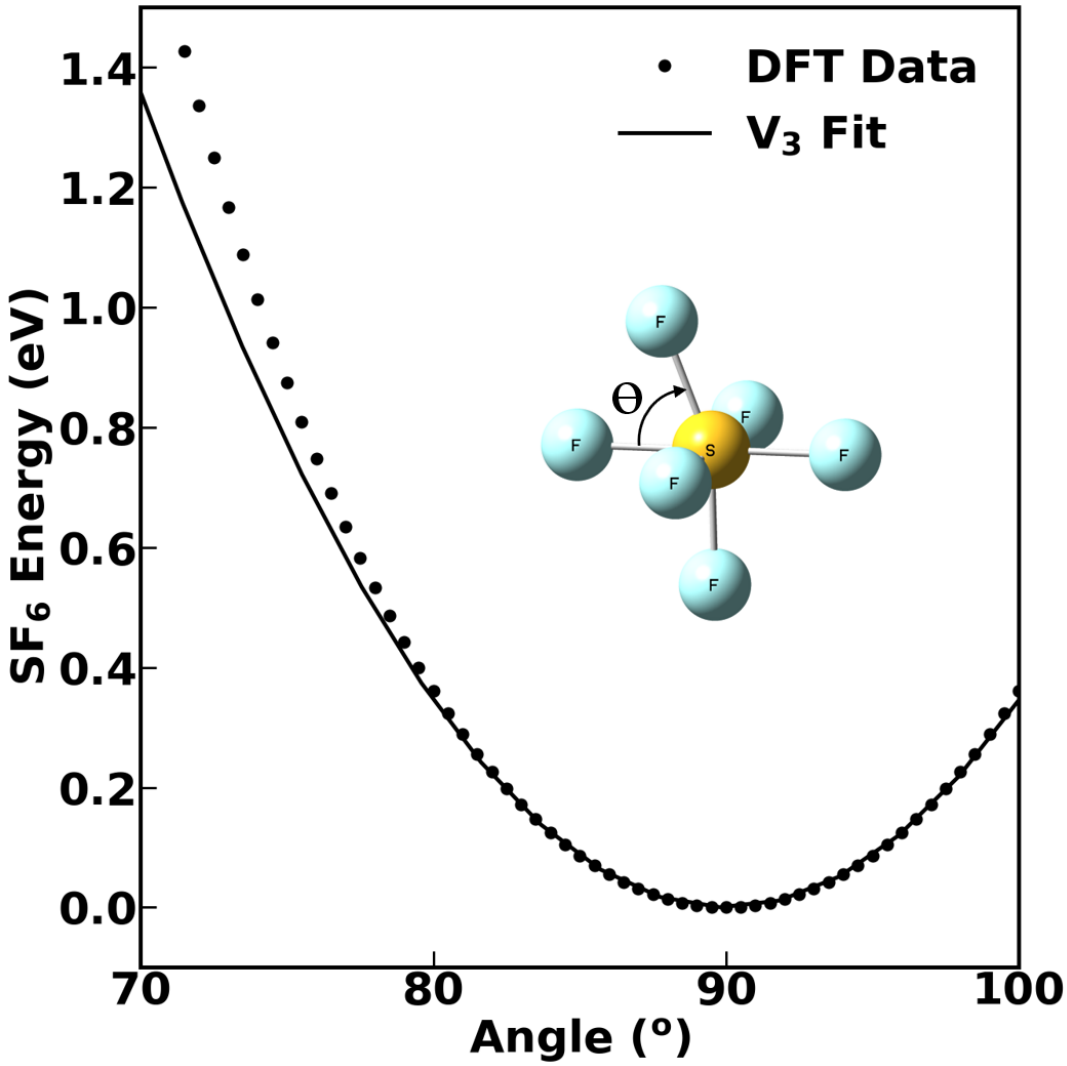

Figure 3.3: The total energy of SF_6 as a function of the angle θ indicated in the inset figure. Angle θ varies without changing its azimuthal angle. The SF_6 is in equilibrium if all F atoms are at the vertices of a regular octahedron and the S-F bond length is 1.56 Å. The total energies (denoted by dots) of the molecule are obtained from DFT calculations and set to be zero in equilibrium, i.e., $\theta = 90°$. The solid curve is obtained from fitting V_3 of Eqn. (3.3) with h_{FSF} defined by Eqn. (3.4) for all triplets of atoms in the SF_6 molecule simultaneously to the DFT energy data. The fitting is focused on the angle near $\theta = 90°$.

Table 3.2: Parameters for three-body potential fitting.

Parameters	Values
k	11.82391 eV
Θ	0.000
γ	2.01829

DFT calculations were also used to obtain the three-body potential V_3 for a triplet of two F atoms and an S atom. Figure 3.3 shows the total potential energy of an SF_6 molecule as a function of angle θ defined in the inset figure, as denoted by dots in the figure. The geometry of an SF_6 molecule in equilibrium is a regular octahedron with a bond angle at the S atom spanned by two adjacent S-F bonds being 90° and the S-F bond length being 1.56 Å. In Fig. 3.3, angle θ is assumed to vary without changing its azimuthal angle, i.e., the two F atoms and an S atom forming angle θ stay in the same plane at $\theta = 90°$.

The fitting of the three body potential V_3 for a triplet of two F atoms and an S atom can be easily performed if we assume the following functional form, i.e.,

$$h_{\mathrm{FSF}}(r_1, r_2, \theta) = \begin{cases} k_{\mathrm{FSF}} |\cos\theta - \Theta_{\mathrm{FSF}}|^{\gamma_{\mathrm{FSF}}} f_{\mathrm{SF}}(r_1) f_{\mathrm{SF}}(r_2) & \text{if} \quad \cos\theta > 0, \\ 0 & \text{if} \quad \cos\theta \leq 0. \end{cases} \tag{3.4}$$

Equation (3.4) was fitted to the DFT calculation data, as shown in Fig. 3.3. The values of k_{FSF}, Θ_{FSF}, and γ_{FSF} are listed in Table 3.2. The cut-off distance r_c is the same as that in Table 3.1. For any other triplet ijk that involves S atoms, the three-body function h_{ijk} is assumed to be null, e.g., $k_{\mathrm{SFF}} = k_{\mathrm{Si,S,Si}} = 0$, in this study.

3.4 Results and Discussion

Figure 3.5 shows the etching yields of Si, F, S, and O atoms for 150 eV SF_5^+ ion bombardment of SiO_2 material as functions of the ion dose. The etching yield of a specific atomic species is defined as the average number of atoms removed or emitted from the surface per ion impact. If the etching yield of Si or O is positive, etching of the surface

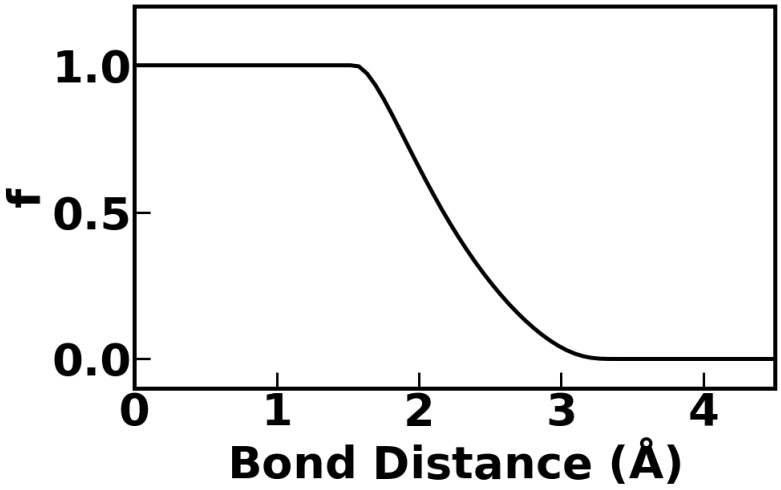

Figure 3.4: Function $f_{\mathrm{SF}}(r)$ as a function of the distance r between S and F atoms.

material SiO_2 is taking place. If the etching yield of S or F is less than 1 or 5, deposition of S or F is taking place as the injected ions are SF_5^+. In Fig. 3.5, the moving average of the instantaneous etching yield (i.e., the number of atoms removed from the surface at each ion injection) over an ion dose of 5.7×10^{12} ions/cm^2 around each ion dose is plotted for each atomic species.

In the etching process, the chemical compositions of the material surface are gradually modified as the ion dose increases until the deposition of S and F atoms from the incident ions and their desorption from the surface are balanced. In such a steady state, the etching yield no longer depends on the ion dose. In the simulation, we assumed that the steady state etching took place when the etching yield of F reaches approximately 5. It is seen in Fig. 3.5 that O is more preferentially sputtered than Si initially.

The simulated and experimental etching yields of Si atoms for Si and SiO_2 materials by SF_5^+ ion impact are plotted as functions of the ion incident energy in Fig. 3.6. The experimental etching yields by F^+ ions for Si [57] and SiO_2 [61] and simulated etching yield by $C2F_5^+$ ions [85] are also included for comparison. The etching yields obtained from the MD simulations were those averaged in steady state. The experimental data were obtained from depth profiling of etched surfaces by multi-beam injection system in a similar manner discussed in Ref. [52]. Details of the ion beam experiments for the SF_5^+

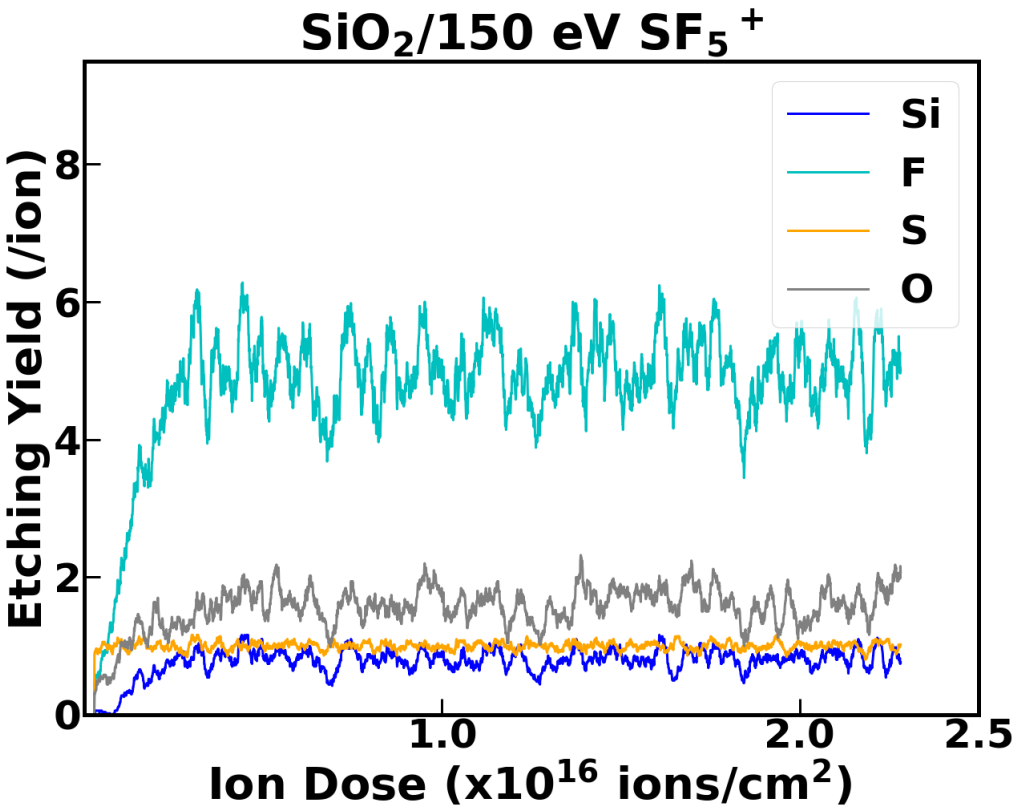

Figure 3.5: Simulated etching yields of Si, F, S, and O atoms as functions of the ion dose for 150 eV SF_5^+ ion bombardment of a SiO_2 material. The etching yield plotted in this figure is the moving average of the instantaneous etching yield over a dose of 5.7×10^{12} ions/cm^2 around each ion dose.

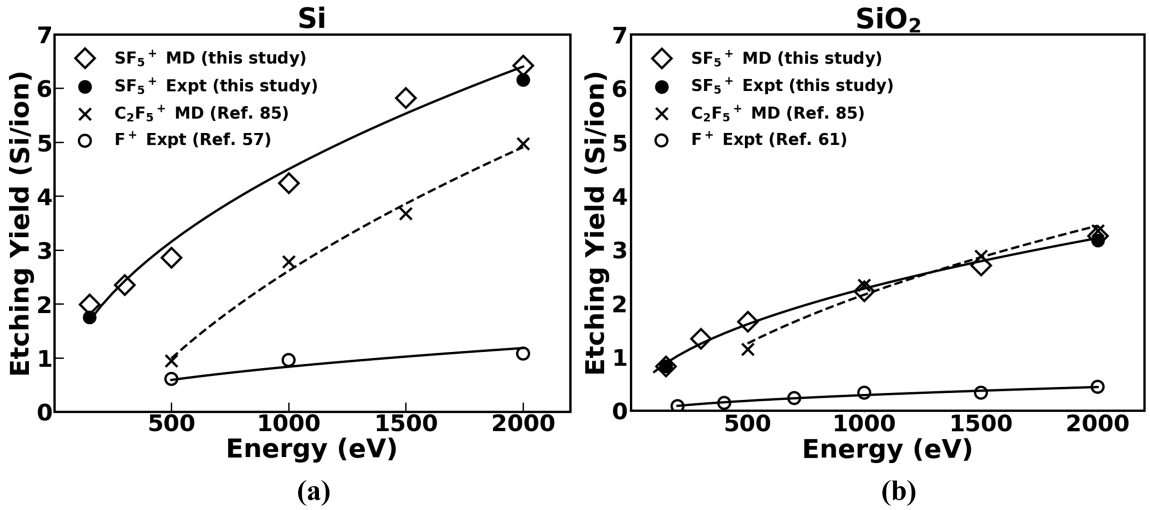

Figure 3.6: Comparison of simulated and experimental etching yields for (a) Si and (b) SiO_2 materials with SF_5^+, $C2F_5^+$, and F^+ ion bombardment as functions of the ion incident energy. The simulated etching yields by SF_5^+ and $C_2F_5^+$ ions are denoted by ◊ and × while the experimental etching yields by SF_5^+ and F^+ ions are denoted by ● and ❍. The simulated and experimental yields by SF_5^+ are obtained in this study. The simulated etching yields by $C_2F_5^+$ ions are taken from Ref. [85] and the experimental etching yields by F^+ ions are taken from Ref. [57] for Si and Ref. [61] for SiO_2. The simulated etching yields were obtained from MD simulation as those for steady-state etching. The curves are guides for the eye.

ion data shown in Fig. 3.6 will be published separately. The universal energy dependence of ion-enhanced etching yield proposed by Steinbrüchel [99] $Y(E) \approx A(E^{1/2} - E_{th}^{1/2})$, where E is the incident ion energy and E_{th} is the energy threshold, was fitted to the etching yield data. Based on the figure, a good agreement between the simulation and experimental results was achieved. The etching yield for the Si material is higher than that for the SiO_2 material at the same ion incident energy and species, which is expected because the Si-Si bond energy is lower than the Si-O bond energy. The etching yield of Si by SF_5^+ ions is also higher than that by $C_2F_5^+$ ions at the same incident energy [85]. This is because C atoms tend to be deposited on the surface during $C_2F_5^+$ ion injections and the formed Si and C mixed layer hinders or slows down the removal of Si atoms [60–62, 75]. In our MD simulations based on the potential model discussed above, S atoms hardly remain on the surface after SF_5^+ ion incidence and therefore volatile species such as SiF_x are formed on the surface unhindered. As mentioned earlier, this seems consistent with our experimental observation as well as that of an earlier study [98].

Figure 3.7 shows the depth profiles of atomic concentrations in Si and SiO_2 materials

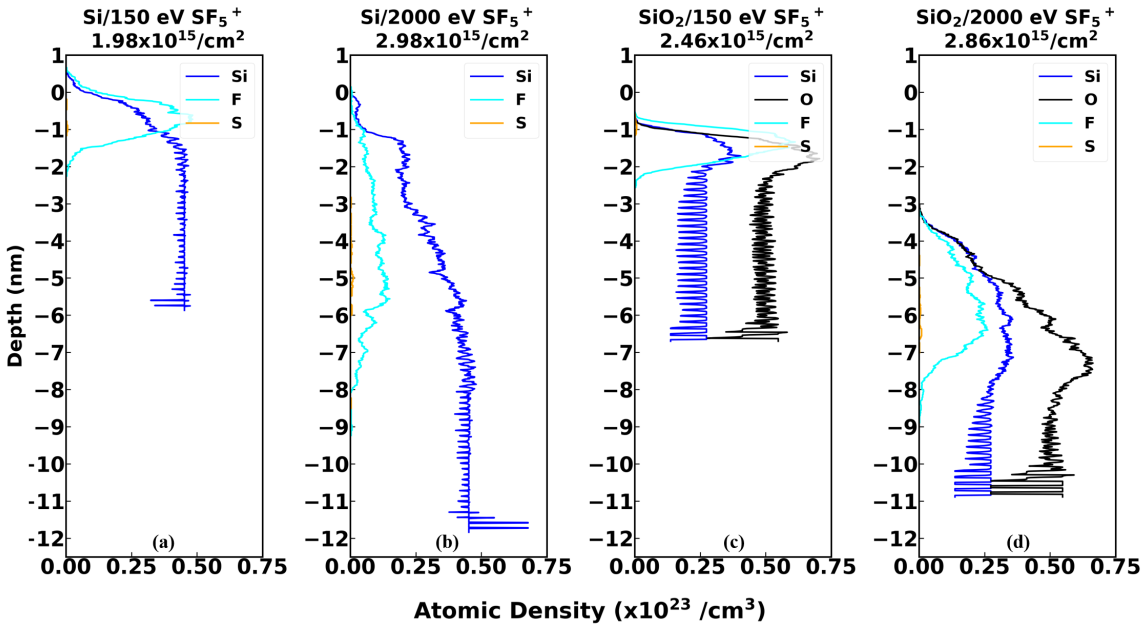

Figure 3.7: Depth profiles taken at the onset of steady state etching of Si with (a) 150 eV and (b) 2000 eV SF_5^+ ion bombardment, and SiO_2 with (c) 150 eV and (d) 2000 eV ion bombardment. The ion dose at which the depth profiles were obtained is listed on the top of each graph. The horizontal axis corresponds to the atomic density and the vertical axis corresponds to the depth (in a negative value) measured from the top surface of the initial material.

around the onset of steady-state etching at ion incident energies of 150 eV and 2,000 eV. The number on the top of each set of profiles denotes the ion dose at which the profiles were depicted. The depth (in a negative value) is measured from the top surface of the initial material. The layer where the material atoms are mixed with incident F atoms is called a mixing layer. This layer serves as a site for the reactions to take place during the etching process. The formation of such layers in etching processes by the injections of chemically reactive species has been also confirmed experimentally [10, 52]. According to Winters and Coburn [10], a mixing layer is formed through the attachment of F atoms with Si dangling bonds present on the surface as well as the insertion of F atoms into the Si-Si bonds or Si-O bonds in the subsurface region. It is seen that, for both Si and SiO_2 materials, thinner mixing layers are formed at 150 eV than at 2,000 eV. This is because, at 2,000 eV, the ions have higher kinetic energy and penetrate more deeply into the materials. In the case of 150 eV ion incidence, because of the abundant presence of F atoms that terminate the bonds of material atoms in the mixing layer, the

etching is chemically enhanced and desorbed species from the surface are more likely to form fluorides, such as SiF_x (x = 1 - 4), than in the case of 2,000 eV ion incidence. The opposite is observed at 2,000 eV, where steady-state etching occurs although the atomic density of F atoms on the surface is still low. This implies that surface atoms are removed mostly by physical sputtering owing to high-energy ion impact.

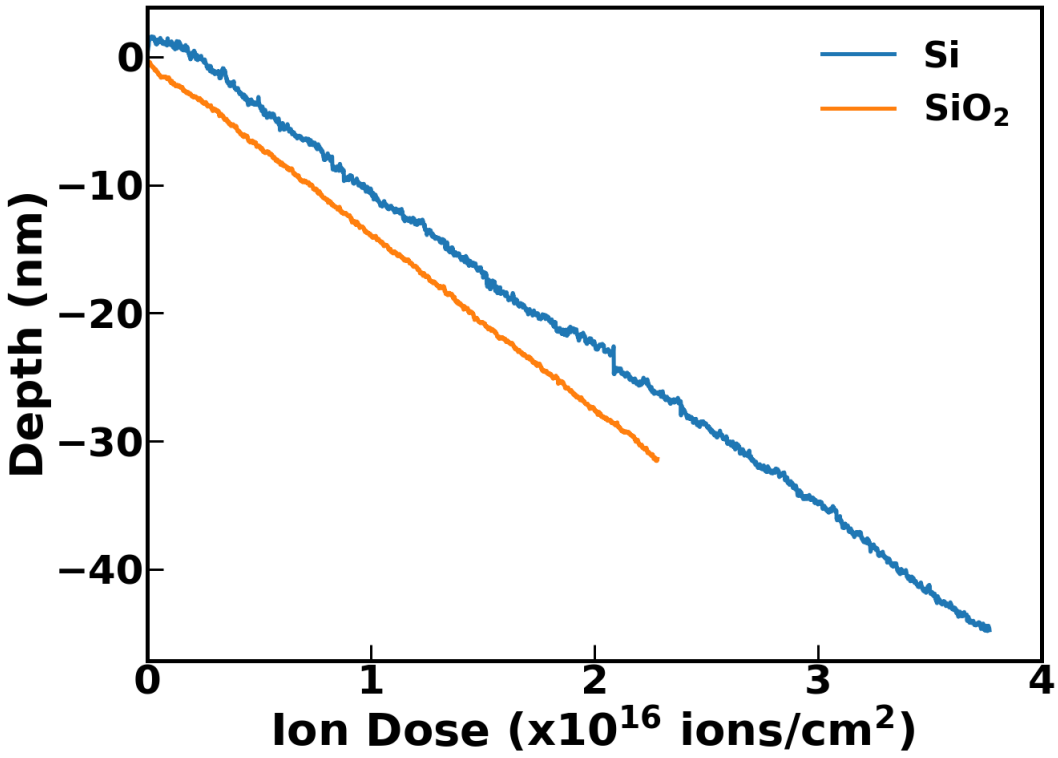

Figure 3.8: Change in the depth of Si and SiO_2 materials as functions of the ion dose by 2,000 eV SF_5^+ ion bombardment. The etched depths per 1×10^{16} ions/cm^2 ion dose, obtained from linear fitting of the data are 12.5 nm for Si and 13.6 nm for SiO_2. The depth 0 indicates the initial height of the material.

Although the Si etching yield for a Si material is higher than that for a SiO_2 material, as shown in Fig. 3.6, the etched depth at the onset of steady-state etching is much greater for SiO_2 than Si, as seen in Fig. 3.7. This is due to the initial preferential sputtering of O atoms from SiO_2 as well as the initial swelling of the Si material arising from the implantation of F atoms. Furthermore, because of the difference in the number density of Si atoms between Si and SiO_2, a higher etching yield of Si does not mean that its etching rate is higher. Following the conventional definition, the etching rate here is defined as

the change in depth of the material per unit time or unit ion dose. The changes in depth of Si and SiO_2 materials at 2,000 eV SF_5^+ ion bombardment are plotted as functions of the ion dose in Fig. 3.8. The linear fitting of these curves at higher ion doses (in steady state) indicates that the depth changes for an ion dose of 1×10^{16} ions/cm^2 are 12.5 nm for Si and 13.6 nm for SiO_2, which are very close to each other, despite the fact that the sputtering yield of Si is much higher than that of SiO_2 at this ion energy. In other words, a stacked material of poly-Si and SiO_2 layers can be etched through with nearly the same etching rate by 2,000 eV SF_5^+ ions.

Figure 3.8 also shows the different nature of the transient phase between Si and SiO_2, where a mixing layer is formed in each material by incident ions at the very initial stage. The height (or negative depth) of Si increases to a positive value immediately after it is exposed to SF_5^+ ions because of the implantation of F atoms supplied from the incident ions. On the other hand, the initial slope (change in depth per unit ion dose) for SiO_2 is slightly steeper than that in a steady state because of the preferential sputtering of O atoms from SiO_2 at the initial stage.

The desorbed species were also analyzed to show how chemical reactions affect the removal of surface atoms. During the simulation, all the removed species (i.e., atoms and groups of atoms) were recorded with their positions and velocities. From this data, the nature of surface chemical reactions may be understood. The desorbed species for Si and SiO_2 materials at different SF_5^+ ion incident energies are plotted in Fig. 3.9. The desorbed species at different ion incident energies are listed along the horizontal axis and the vertical axis represents the percentage of the number of each desorbed species to that of all desorbed species. For both cases, 'Others' refers to the total amount of desorbed species which do not contain Si or O atoms such as F_xS_y ($x = 0$ - 3, $y > 1$) and desorbed species which contain Si or O atoms but the amount is very low, i.e. Si_xF_y ($x > 1$, $y > 4$) and $Si_xO_yF_z$ ($x > 1$, $y > 2$, $z > 4$). The amount of these Si_xF_y and $Si_xO_yF_z$ are insignificant compared to the reported SiF_x and SiO_yF_x in the paper. The amount of F_xS_y is normally high, thus the percentage of 'Others' is high. It is seen in (a) that, for a Si material, Si atoms are most likely to be removed as single atoms or in the form of

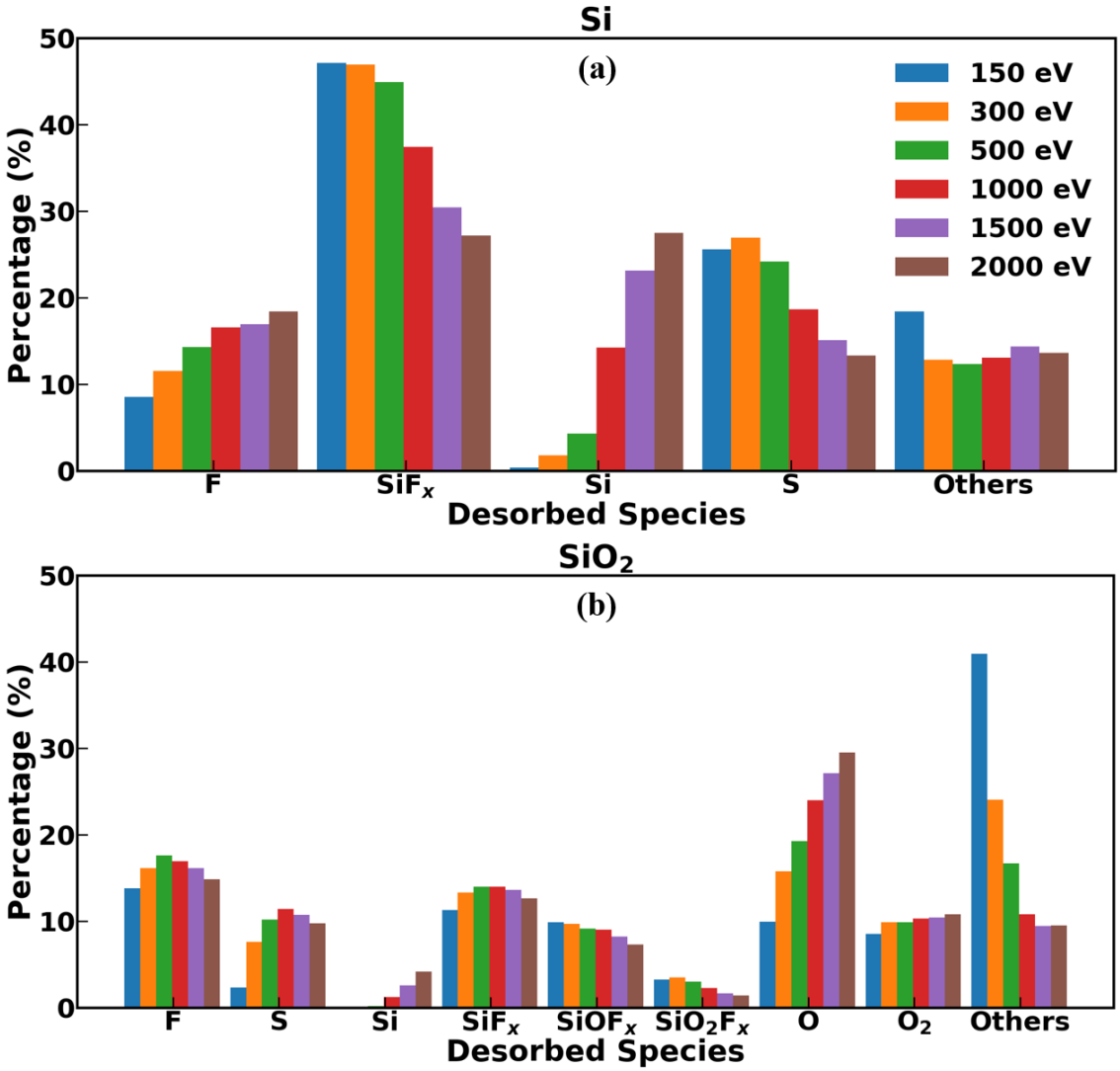

Figure 3.9: The percentage of desorbed species for (a) Si and (b) SiO_2 materials with 150 – 2,000 eV SF_5^+ ion incidence. SiF_x, $SiOF_x$, and SiO_2F_x represent desorbed species which contain different amount of F atoms (x = 1 - 4). The color indicates the ion energy. It should be noted that, in our simulation, we neglect chemical reactions of S and the results presented here should be construed as such.

SiF_x. With increasing ion incident energy, the percentage of SiF_x decreases whereas that of Si increases, which indicates that the etching becomes more physical than chemical at higher ion incident energy. However, even at 2,000 eV, the percentages of SiF_x and Si are almost the same. In other words, as SF_5^+ ions supply a large amount of F to the surface, the etching at 2,000 eV is sufficiently driven chemically.

The desorbed species for SiO_2 materials are summarized in a similar manner in (b) but a slightly different trend is seen. In this case, the ratio of monoatomic Si desorbed species is much smaller than those of other polyatomic Si desorbed species such as SiF_x, $SiOF_x$ (x = 1 - 4), and SiO_2F_y (y = 1 - 3) in all the energy range examined. On the other hand, O atoms desorb mostly as O and O_2 desorbed species but hardly as OF_z (z = 1 - 2). This is because the bond energy of O-F is much lower than that of Si-F and, therefore, adsorbed F atoms tend to leave the surface as compounds with Si, rather than O, if not as single F atoms.

Figure 3.10 shows the percentage of the number of desorbed species having the forms of SiF_x, $SiOF_x$ (x = 1 – 4), and SiO_2Fy (y = 1 – 3) for each x and y to that of all species listed in the figure. In the case of Si, it is seen in (a) that the desorbed species are dominated by SiF_3 and SiF_2 at ion incident energy ranging from 150 to 500 eV. Then, as the ion energy further increases, the percentage of SiF increases while those of SiF_2 and SiF_3 decrease and SiF_4 nearly disappears. In the case of SiO_2, it is seen in (b) that, at low ion incident energy ranging from 150 to 500 eV, desorbed species carrying higher numbers of F atoms such as SiF_4, SiF_3, $SiOF_3$, $SiOF_2$, and SiO_2F_2 are the main contributors to etching. And at higher energy, on the other hand, desorbed species with single F atoms, i.e. SiF, SiOF, and SiO_2F, dominate as desorbed species.

These results are also consistent with what is observed in the depth profiles in Fig. 3.7. At lower ion incident energy, more F atoms are available on the material surface to form desorbed species than at higher ion incident energy, so that the desorbing Si atoms can readily form species with higher numbers of F atoms such as SiF_3, SiF_4, $SiOF_3$, and SiO_2F_3. At higher energy, on the other hand, F atoms are less available on the surface and, with higher energy impact, surface Si atoms are sputtered mostly as species with

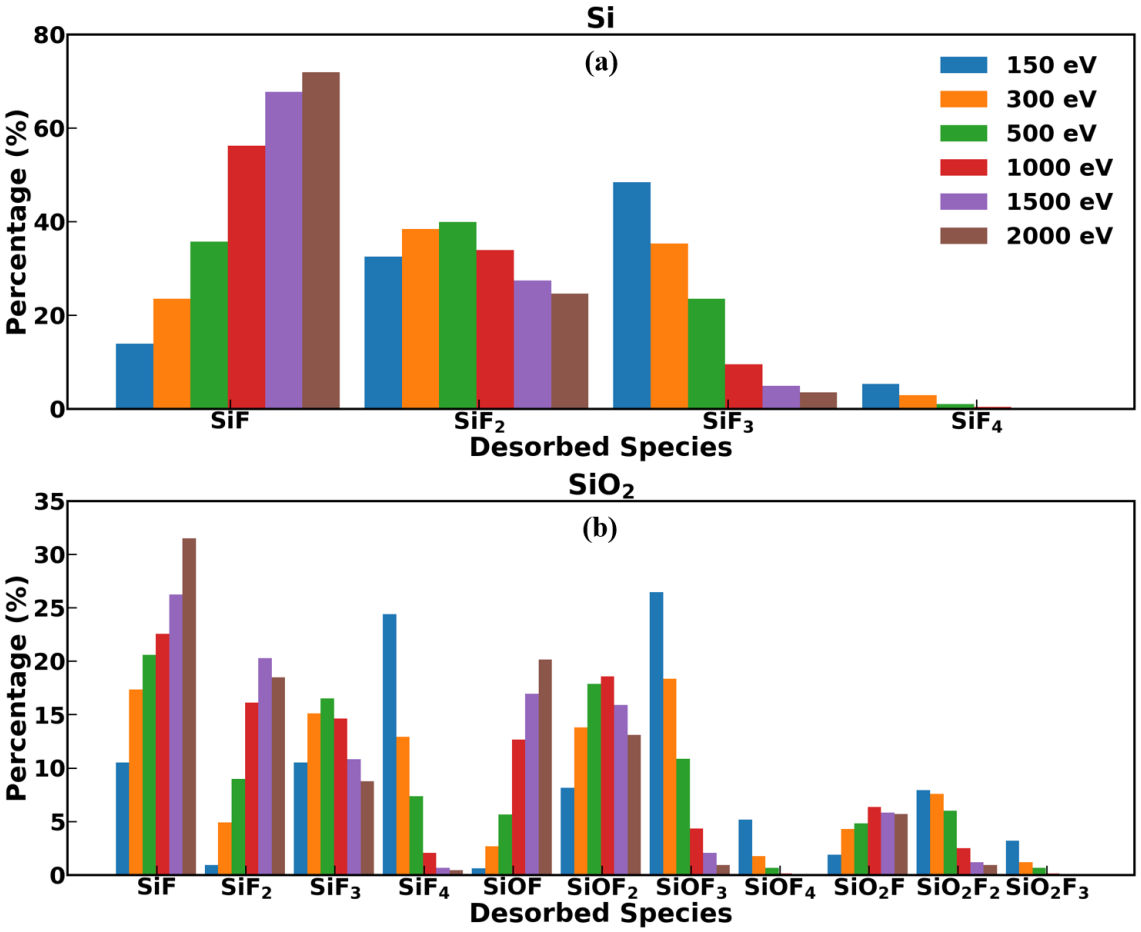

Figure 3.10: The percentage of Si-containing F atom desorbed species for (a) Si and (b) SiO_2 materials with 150 to 2000 eV SF_5^+ ion incidence. The color indicates the ion energy. It should be noted that, in our simulation, we neglect chemical reactions of S and the results presented here should be construed as such.

fewer numbers of F atoms. These results indicate that the etching of Si and SiO_2 by SF_5^+ ion bombardment is, even at high energy of 2,000 eV, still sufficiently driven by chemical reactions of F with the surface/subsurface atoms of the material. Full chemical etching is considered to occur when stable and volatile SiF_4 molecules are formed and desorbed [10, 87]. However, SiF_4 dominates as desorbed species only for SiO_2 etching at 150 eV among the cases we examined in this study, as seen in Fig. 3.10(b). This is because the density ratio of the accumulated F atoms to surface Si atoms is much higher in the case of a SiO_2 material than a Si material, as seen in Fig. 3.7. Since O-F bonds are much weaker than Si-F bonds, most available F atoms are bonded with Si atoms, rather than O atoms, and can form volatile SiF_4 molecules if the density of F atoms is sufficiently higher than the surface Si atoms.

On the other hand, Si atoms bonded with less than four F atoms such as SiF, SiF_2, and SiF_3 are normally chemically bonded to the surface with the remaining bonds and therefore nonvolatile at room temperature [10]. However, in the presence of energetic ion impact, these nonvolatile molecules can be easily knocked out from the surface during the collision cascade process. Thus, the etching by such species is caused by the bond termination of surface Si atoms by F atoms (chemical effects) combined with the direct impact of incident ions (physical effects), which is known as reactive ion etching. Furthermore, it is also possible that weakly bonded SiF_x molecules in the mixing layer are desorbed through thermal processes [52]. However, the thermal desorption cannot be observed correctly in our MD simulations where the cooling is too rapid compared with the real system.

3.5 Conclusions

We have performed MD simulations to evaluate etching yields of Si and SiO_2 materials by SF_5^+ ion bombardment for the ion incident energy range from 150 eV to 2,000 eV. The results were also compared with the etching yields obtained from mass-selected ion beam experiments. To perform the MD simulations, we constructed classical interatomic

potential functions for S with F and other atoms, assuming that S forms covalent bonds only with F. This assumption is based on the ex-situ experimental observation that no S remains on the Si or SiO_2 surface after being etched by SF_5^+ ions or SF_6 plasmas. However, in reality, S is also known to form covalent bonds with Si and O, forming, e.g., SiS and SO_2. The construction of more realistic interatomic functions for S is deferred to a future study. Despite this simplified assumption for the interatomic potential functions constructed in this study, the etching yields evaluated by our MD simulations were found to be in a good agreement with experimentally obtained yield data.

The MD simulation and experiments have shown that the etching yield of Si atoms evaluated for a Si material is nearly twice larger than that for a SiO_2 material in a steady-state etching at high ion incident energies, e.g., at 2,000 eV. Because of the difference in the number density of Si atoms between Si and SiO_2 materials, the etching rates, i.e., etched depths per unit time, for Si and SiO_2 are nearly the same under such conditions. This means that a stacked material of poly-Si and SiO_2 layers can be etched through with nearly the same etching rate if we use SiF_5^+ ions with a high ion incident energy.

Based on the depth profiles at the onset of steady-state etching obtained from MD simulations, it is found that the etching yield is dependent on the supply of F atoms to the material surface, especially at low ion incident energies. A steady-state etching was observed to occur only after an ample amount of F became available on the surface, especially when the ion incident energy is low. In general, RIE is due to the combination of both physical and chemical effects. The desorbed species from the surface by SiF_5^+ ion etching are mainly composed of SiF_x for a Si material, and SiF_x, $SiOF_x$ ($x = 1 - 4$), and SiO_2F_y ($y = 1 - 3$) for a SiO_2 material. These species, except for SiF_4, are non-volatile compounds but they are removed from the surface with the help of energetic ion impact. Our MD simulation results indicate that the etching of Si and SiO_2 by SF_5^+ ions becomes more dominated by physical sputtering as the ion incident energy increases.

Chapter 4

Development of Si, O, I system interatomic potentials

4.1 Introduction

Plasma processing has a very wide applications in several major industries such as electronics, automobiles, defense and even aerospace. One of the major applications of plasma processing is in reactive ion etching (RIE) of semiconductor materials for electronic devices. Plasmas that are generated from gases that contain fluorine (F) are normally utilized in current plasma etching processes of semiconductor materials such as silicon (Si) and silicon dioxide (SiO_2). This is because, F^+ ions are known to be highly reactive with Si atom by forming volatile molecules such as SiF_4 [100].

Several studies on Si and SiO_2 etching with halogen-containing plasmas have been published [36, 37, 53, 61, 62, 65, 84, 101–112]. In the early studies by Legtenberg *et al.* [102] in 1995, they added CHF_3 to SF_6/O_2 plasma to fabricate micromechanical structures with high aspect ratios on Si materials. In 1998, Vyvoda *et al.* [84] also studied the effects of different plasma conditions on the shapes of features in SiO_2-masked crystalline Si etched with Cl_2 and HBr plasmas. Based on their results, higher etching rates were achieved with Cl_2 plasmas. However, the trench profiles in HBr plasma etching were more vertical and the trench bottoms were flatter. More recent study by Gaboriau *et al.* [107]

in 2005 on the etching of Si and SiO_2 materials with inductively coupled fluorocarbon plasmas showed that etching of Si is dependent on the fluorine species on the plasma and on the fluorocarbon blocking overlayer formed on the surface. On the otherhand, SiO_2 is dependent on the ratio of F and carbon on the plasma.

Recently, the size of the components of electronic devices is continuously decreasing to nanometer scale. This has lead to several challenges in the fabrication processes such as the need for better precision, higher etching yields, and selectivity among others. Continuous research on new etchants is important and necessary to cater the arising problems in the fabrication of nano-scale semiconductor structures. In this research, simple interactomic potential functions were developed to describe the Si, O and I systems interactions using modified Stillinger-Weber potential functions [41]. The potential functions were then implemented in molecular dynamics (MD) simulation to study the feasibility of etching Si and SiO_2 surfaces with I^+ ion bombardment. The etching yields were calculated and compared with the experimental etching yields with other halogen such as F^+, Cl^+ and Br^+ ions.

4.2 Potential Development of Si, O, and I systems

Modified Stillinger-Webber (SW) potential functions [41] were used to describe the two-body and three-body potential of Si, O and I atoms. The details of the functions were discussed in previous studies [38, 42]. According to the SW potential function, the total energy of a system is equal to the sum of the two-body (V_2) and three-body (V_3) interactions as given by Eq. (4.1).

$$\Phi = \sum_{i<j} V_2(i,j) + \sum_{i<j<k} V_3(i,j,k) \tag{4.1}$$

V_2, which is a summation of the repulsive and attractive interactions, is given by the following equation:

$$V_2(r) = ar^{-2q} \exp \frac{2d}{r - r_c} - br^{-q} \exp \frac{d}{r - r_c}, \tag{4.2}$$

where a, b, d, p, q and r_c are parameters. The distance between two atoms is r and the cut-off distance is r_c, i.e. V_2 is zero beyond the cut-off distance. For this equation to be satisfied, $r < r_c$ and $d > 0$.

The three-body term V_3 is equal to the summation of three h functions.

$$V_{3Total}(r_i, r_j, r_k) = h_{ijk} + h_{jik} + h_{ikj}. \tag{4.3}$$

The h function is written as:

$$h_{jik}(r_{ij}, r_{ik}, \theta_{jik}) = k_{jik}|cos\theta_{jik} - \Theta_{jik}|^{\gamma_{jik}} f_{ij}(r_{ij}) f_{ik}(r_{ik}), \tag{4.4}$$

where θ_{jik} is the angle between the three atoms, and k, Θ, and γ are parameters. For a system with only 3 atoms, the V_{3Total} is approximately equal to only one h function, with the assumption that the other two h functions are negligible because the distance of the two atoms opposite the angle is larger than the cut-off distance, r_c.

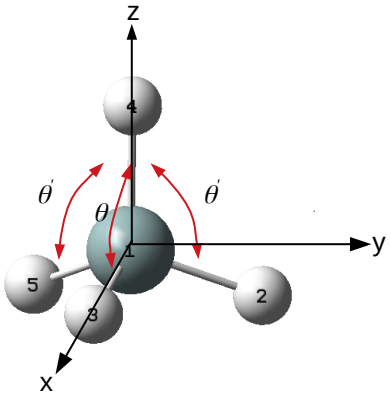

Figure 4.1: In methane-like structures, when the three body angle θ moves, the adjacent angles θ' also change.

For atoms with four available bonds and can form methane-like molecules such as Si, the optimized geometry has an angle of approximately 109.5°. In this case, the three-body potential is also affected by the adjacent angles (θ') as illustrate in Fig. 4.1. Because the structure is symmetric, the values of the two θ' are the same. V_{3Total} will now be equal to the sum of the three-body potential due to θ ($V_3(\theta)$), and the three-body potentials

due to the two θ' ($V_3(\theta')$).

$$V_{3Total} = V_3(\theta) + 2V_3(\theta'). \tag{4.5}$$

The expression for $\cos\theta'$ in terms of θ can be derived by taking the dot product of the vectors $\overrightarrow{14}$ and $\overrightarrow{12}$ in Fig. 4.1.

$$\cos\theta' = \overrightarrow{14} \cdot \overrightarrow{12} = -\frac{1}{3}\left(\cos\theta + \sqrt{2\left(1-\cos^2\theta\right)}\right). \tag{4.6}$$

Using Eqns. (4.4) and (4.6), V_{3Total} for methane-like structure molecule is

$$V_{3Total}(\theta_{ijk}) = \left(k\left|\cos\theta_{ijk} - \Theta\right|^{\gamma} + 2k\left|-\frac{1}{3}\left(\cos\theta_{ijk} + \sqrt{2\left(1-\cos^2\theta_{ijk}\right)}\right) - \Theta\right|^{\gamma}\right) f_{ji} f_{jk}. \tag{4.7}$$

Table 4.1: Parameters for V_2 fitting of Si-I, I-I and I-O two-body systems.

2 - Body	a (eV)^{2q}/Å	q	b (eV)^{q}/Å	d (Å)	r_c (Å)
I-I	603.18	2.23	60.84	0.99	3.89
Si-I	897.11	1.72	93.94	2.25	3.99
O-I	532.92	1.95	71.82	1.97	3.67

Density Functional Theory (DFT) calculations of the two-body potentials of Si-I, I-I, and I-O were performed using Gaussian 09 software [95] using B3LYP method and LANL2DZ basis sets. SiI_4, I_2 and OI_2 molecules were used in the calculation. First, the molecules were optimized especially SiI_4 and OI_2. Then the energy was scanned while changing the distance of the atoms simultaneously, and at the same time, keeping the angles between the atoms constant. After the energy scan, the minimum energy and bond distance of the DFT calculation data are adjusted based on literature values [96]. The fitting of Eqn. (4.2) on the DFT data are presented in Fig. 4.2. The values of the fitting parameters are listed in Table 4.1.

DFT calculations of the three-body potentials of different O, I and Si combinations (I-Si-I, I-Si-Si, I-Si-O, Si-O-I, O-O-I and I-O-I) were also performed using the same method

and basis sets. In all of the calculations, all extra bonds were terminated with hydrogen (H), assuming that the effects of H on the energy is negligible. In the case wherein the central atom is Si, the I-Si-H bond angles are kept at 109.5° during the calculation. The distances between the atoms were fixed based on the optimized geometry. Figure 4.3 shows the fitting of the DFT calculation data and the fitting of Eqn. (4.7) for (a) molecules with Si as the central atom (I-SiI, I-Si-Si, and I-Si-O), and fitting of Eqn. (4.4) for (b) molecules with O as the central atom (I-O-I, Si-O-I, and O-O-I). The inset figures illustrate the set-up of the molecules in the three-body scan.

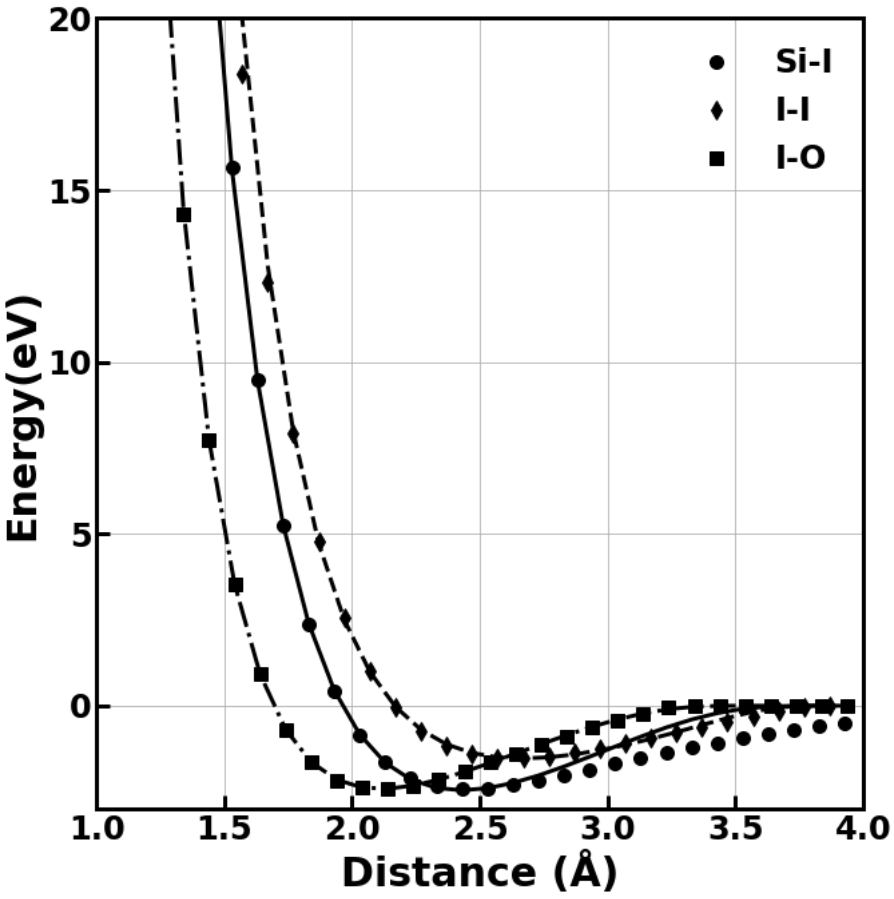

Figure 4.2: Fitting of Si-I, I-I, I-O two-body potentials. The ●, ◆ and ■ data points represent the DFT calculation data. The curves represent the fitting of the data points using Eqn. (4.2).

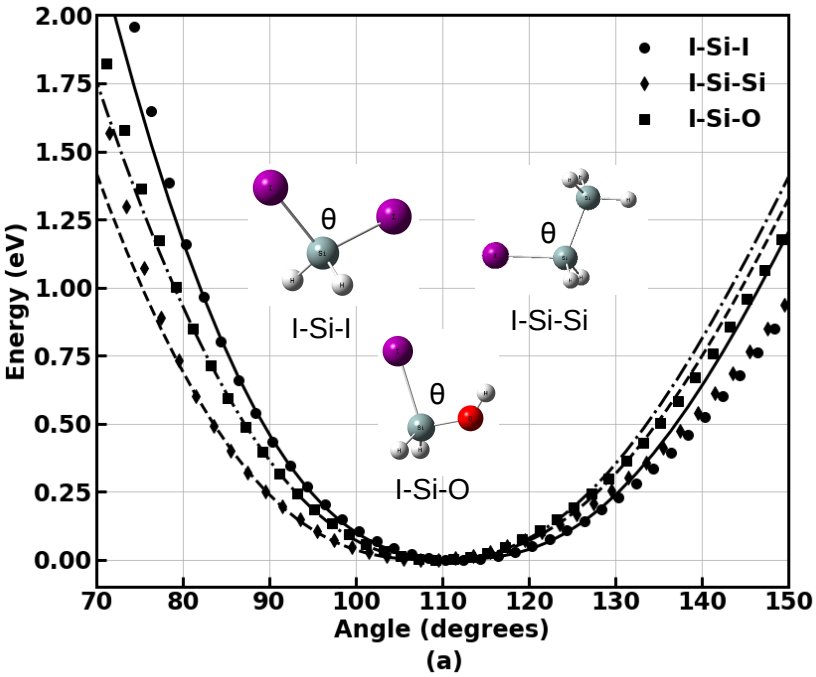

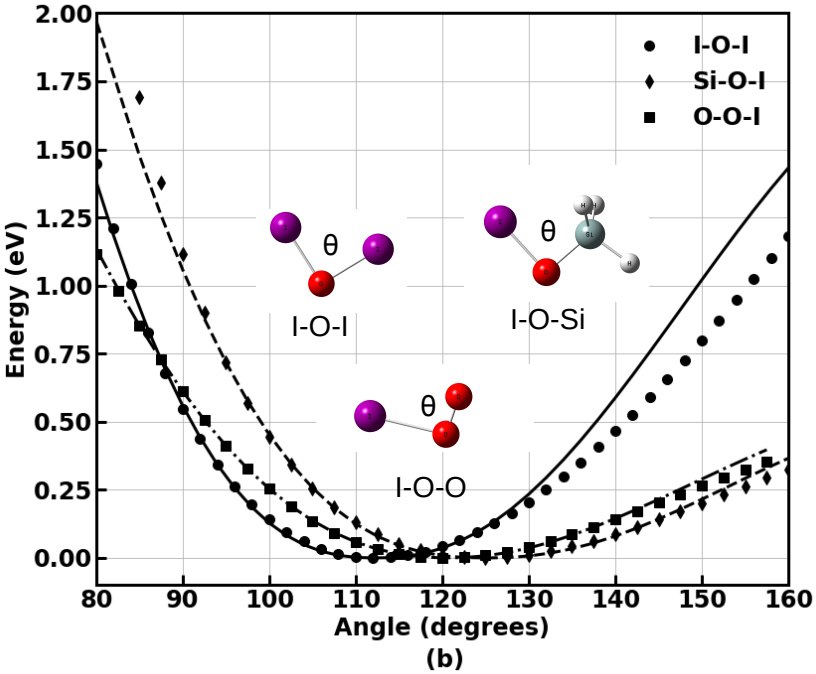

Figure 4.3: Three-body potential fitting of (a) I-Si-I, I-Si-I and I-Si-O, and (b) I-O-O, Si-O-I and O-O-O. The ●, ◆ and ■ data points represent the DFT calculation data. The inset figures show the molecule configurations during the DFT calculation.

Table 4.2: Parameters obtained from three-body fitting.

3 - Body	k (eV)	Θ	γ
I-SiI	4.76	-0.39	2.61
I-Si-Si	3.81	-0.31	2.61
I-Si-O	3.96	-0.34	2.35
Si-O-I	3.92	-0.57	2.36
O-O-I	2.54	-0.51	2.11
I-O-I	5.75	-0.38	2.40

4.3 Molecular Dynamics Simulation

The developed potentials were implemented in MD simulation to study the etching of Si and SiO_2 materials with I^+ ion bombardment. The details of the simulation were already discussed in the previous chapters of this thesis. In the simulation, the ions were treated as charge neutral atoms owing to the Auger or resonant tunneling processes. Through this process, when the ions approach the surface, their wave funtions overlap and charge is transferred from the ions to the surface, neutralizing the ions [57, 113].

The size of the Si material is 4.89 nm $\times$ 4.89 nm with an initial thickness of 5.43 nm, and the size of the SiO_2 material is 4.19 nm $\times$ 4.19 nm with an initial thickness of 6.98 nm. Periodic boundary conditions were applied on the horizontal directions to represent an infinite width of the material. Sufficient thickness of the material was set to avoid overheating of the material during the ion impact. However, in cases wherein overheating happens, the simulation stops and several layers are automatically added from the bottom. The bottom two layers of the materials are fixed and serve as an anchor to avoid drifting or movement of the simulation cell.

In the MD simulation, an I^+ ion with a pre-determined energy is injected cyclically on the surface. One injection cycle lasts for 2,000 fs. The injection time is divided into energy conservation calcucalation for the first 300 fs, followed by Langevin thermostat [49] cooling for 1,600 fs and by another cooling through Berendsen heat bath [50] at the last 100 fs. The ion energy was varied from 300 to 2,000 eV. A total ion dose of 3.35 $\times$ $10^{16}/cm^2$ and 2.28 $\times$ $10^{16}/cm^2$ were simulated for Si and SiO_2 materials, respectively.

4.4 Results and Discussions

Figures 4.4(a)-(b) show the final images of the Si and SiO_2 materials at the onset of steady state etching, which means that the etching yield is no longer dependent on the ion dose, at 300 eV I^+ ion bombardment. The horizontal axis represents the depth in relative to the initial position of the top surface (depth = 0) before the ion bombardment. The x-axis shows the atomic density of Si, I and O atoms. Based on the figures, I^+ ions penetrated deeper in Si than in SiO_2, creating a thicker mixing layer. The mixed Si and I atoms on the top layer of Si is also porous and most of the I atoms penetrated deeper into the material and replaced Si atoms as indicated by the high atomic density of I and low atomic density of Si in the middle portion of the mixing layer. This also caused the shift of the position of the top surface to 3 nm. In the case of SiO_2 material, the I atoms did not drastically shift the positions of the Si and O atoms on the material. This can be due to the higher density of SiO_2 than Si.

The etching yields of Si, O and I as functions of ion dose at 300 eV I^+ ion bombardment are plotted in Fig. 4.5. The graphs show that steady state etching occured faster in SiO_2 material than Si. It was also observed that the etching yield of Si in Si material is not very consistent even after reaching steady state etching. Instead, the etching yields of I and Si rise and fall periodically. This can be caused by the deposition of more I atoms in the deeper portion of the material as discussed earlier in Fig. 4.4(a). As I atoms accumulate, the surrounding Si-Si bonds weaken until such time that the Si atoms will be simultaneously removed from the surface. The removal of Si atoms slows down when the amount of deposited I atoms on the material is relatively minimized. However, this trend should be verified experimentally.

The etching yields of Si and SiO_2 were averaged from the start of steady state etching. The averaged etching yields as functions of the I^+ ion energy are plotted in Fig. 4.5(a)-(b). Based on the figures, the etching yield of Si is higher than SiO_2 material. This can be attributed to the observations with the depth profiles wherein large amount of I atoms accumulated on the Si surface, breaking Si-Si bonds, which in return, caused the easier removal of Si atoms from the surface.

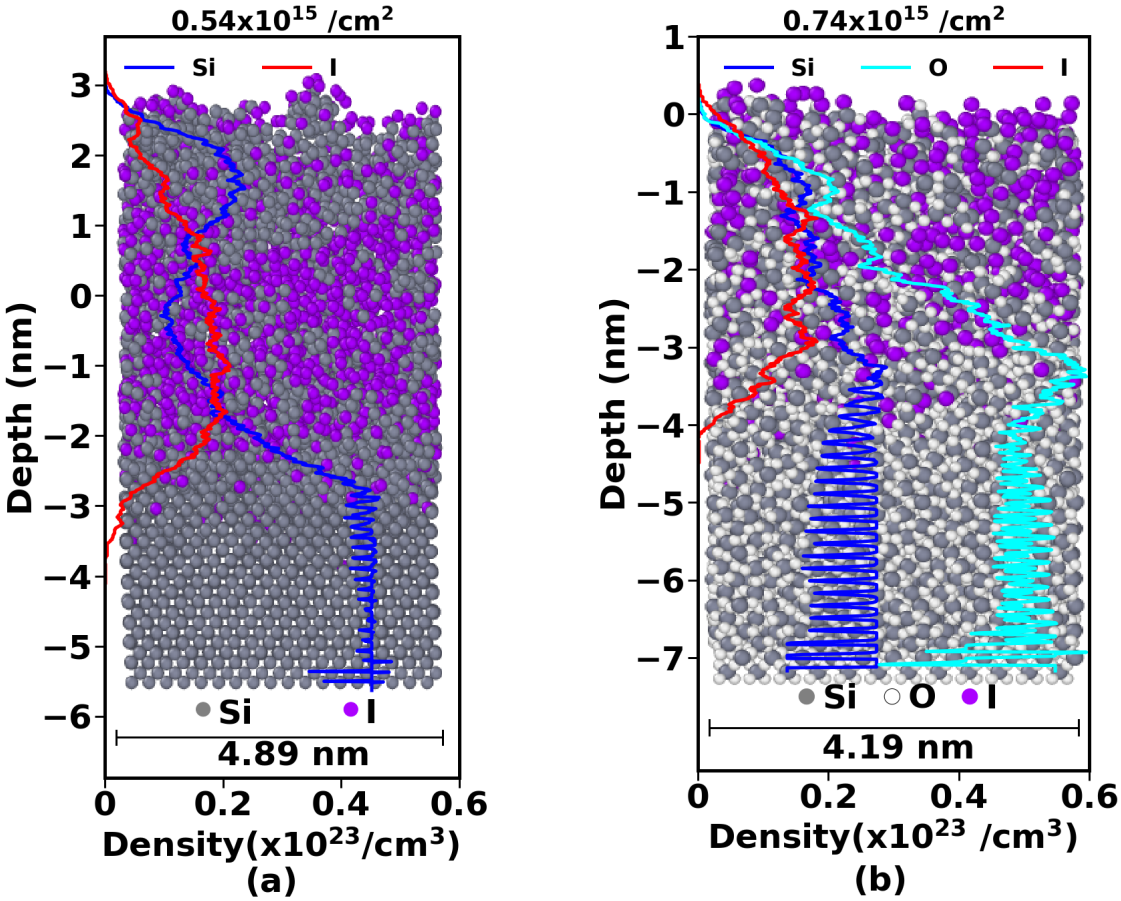

Figure 4.4: Final images of the Si and SiO_2 materials and the corresponding depth profiles after 300 eV I^+ ion bombardment taken at the start of steady state etching. The ion doses are written on top of the figures. The x-axis shows the atomic density of the Si, I and O atoms on the material. The y-axis represents the depth of the materials from the top surface.

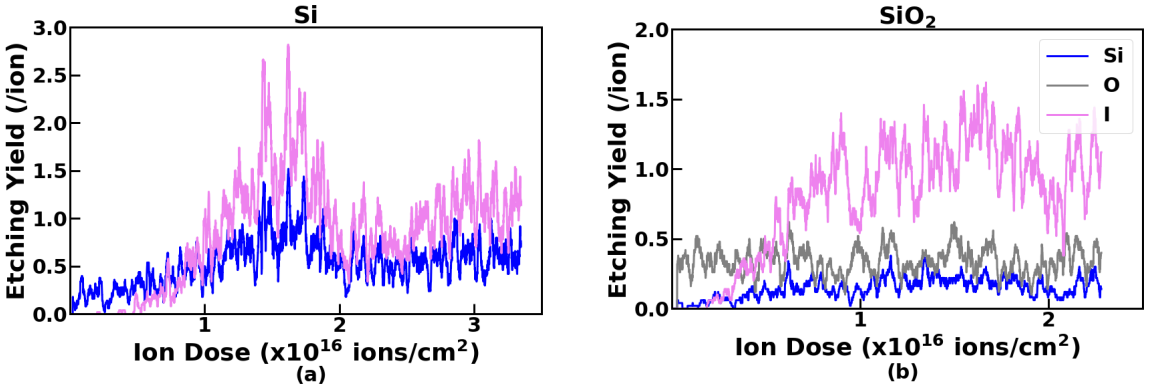

Figure 4.5: Etching yields of Si and SiO_2 at 300 eV I^+ ion bombardment.

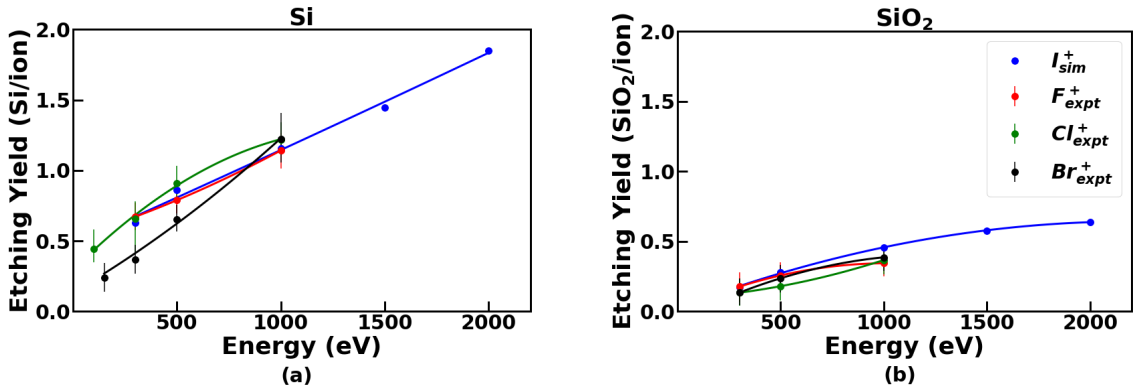

Figure 4.6: Comparison of simulated etching yields of Si and SiO_2 with I^+ ion bombardment and experimental beam data for F^+, Cl^+ and Br^+ ion bombardments.

The etching yields by other halogen ion bombardments such as F^+, Cl^+ and Br^+ obtained from multi-beam injection system experiments are also plotted in Fig. 4.6 for comparison. To the best of our knowledge, there are no published data of experimental etching yield of I^+ ions. We observed that the etching yields of both Si and SiO_2 with I^+ ion bombardment are not that different from the etching yields with F^+, Cl^+ and Br^+ ion bombardments. This indicates that our simulation is within reasonable range. It can be seen from the figures also that the etching yield dependence on the ion type is not so significant at high energy of 1,000 eV.

The desorbed species were also analyzed to study the etching mechanisms with I^+ ion bombardment. Figures 4.7(a)-(b) show the percentage of the desorbed species for 300 to 2,000 eV I^+ ion bombardment of Si and SiO_2 materials, respectively. Only the desorbed species with significant amount are listed on the x-axis. For the Si material in Fig. 4.7(a), the percentage of monoatomic desorbed species is highest for all energy range. This indicates that the Si atoms are removed from the surface due to physical sputtering effect. The percentage of Si containing I atoms such as SiI, SiI_2 and SiI_3 is very low even though the density of accumulated I atoms on the surface is very high as seen in Fig. 4.4(a). The same trend is observed in the case of SiO_2 material in Fig. 4.7(b). The percentage of monoatomic Si desorbed species is also very high and increases with I^+ ion energy. Moreover, very low amount of SiI and SiI_2 were sputtered from the surface. These indicate that the etching of SiO_2 is also mainly due to physical sputtering effects.

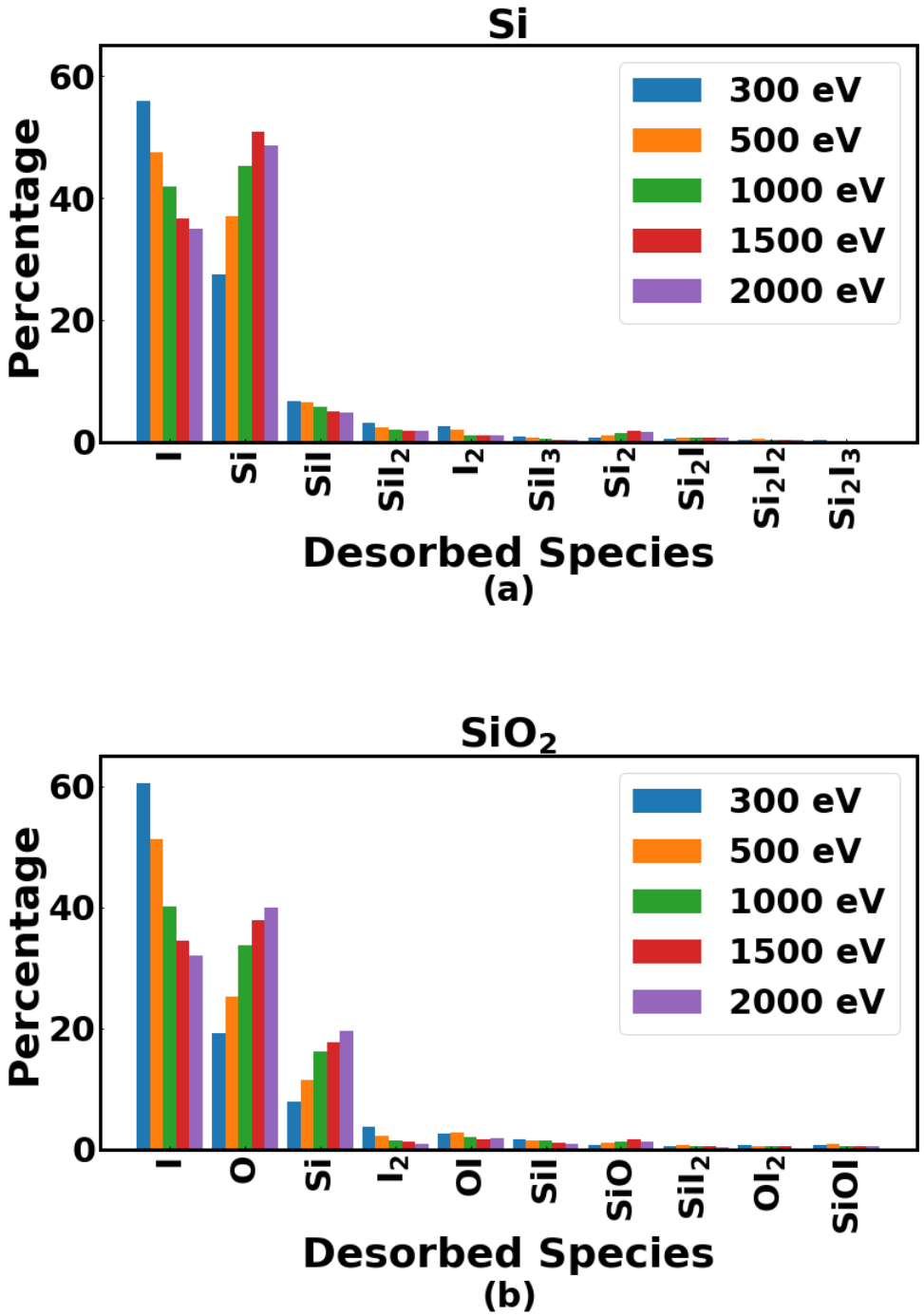

Figure 4.7: Desorbed species for (a) Si and (b) SiO_2 materials.

4.5 Conclusions

An interactomic potential model of Si, O and I atoms interactions was successfuly developed. The etching yields of Si and SiO_2 by I^+ ion bombardment in the incident ion energy range of 300 to 2,000 eV were evaluated with the newly developed potential functions using MD simulation. The simulated etching yields were compared with experimentally obtained data of Si and SiO_2 by F^+, Cl^+ and Br^+ ions because no experimental yield data are available. The numerically obtained etching yields seemed consitent with the experimental data for other halogen ions. This indicates that the simulation results can be reasonable.

The analysis of the depth profiles after the I^+ ion bombardment showed that I atoms can penetrate very deeply into the material especially in the case of Si material. Thus, thick mixing layer was created. Moreover, it was observed from the analysis of the desorbed species that etching is dominantly due to the physical sputtering of Si even in the lower energy range. Very few percentage of Si bonded with I desorbed species such as SiI and SiI_2 was observed. This can be due to the replacement of Si atoms by I atoms in the mixing layer. Based on Fig. 4.4(a), the atomic density of I atoms is higher than the atomic density of Si atoms in the middle portion of the mixing layer in the case of Si material. In the case of SiO_2 material in Fig. 4.4(b), the atomic densities of Si and I atoms are almost the same. These results indicate that majority of Si-Si and Si-O bonds are broken due to the deposition of I atoms, leading to the desorption of Si and O atoms.

Chapter 5

Surface damage formation during atomic layer etching of silicon with chlorine adsorption

5.1 Introduction

Recent advances in semiconductor technology have continued to drive the miniaturization of semiconductor devices and their minimum dimensions are now approaching the atomic size, i.e., the fundamental physical limit of the miniaturization. Therefore the industry is now adopting new device technologies such as three-dimensional structures and the use of non-conventional materials to improve their performance further. Accordingly, the mass manufacturing of such devices is facing tremendous challenges in developing highly precise and controllable processing technologies [79].

Some of the promising solutions to such manufacturing challenges are atomic layer processes (ALPs), i.e., cyclic processes of the formation of a uniform film with a near monolayer thickness, or the removal of a material with a near monolayer thickness at specific locations. The former is called atomic-layer deposition (ALD) [114, 115] and the latter is called atomic-layer etching (ALE) [12, 116–122]. In a typical ALP, once a monolayer (or a very thin layer close to a monolayer) of the material is deposited or

etched, the process automatically stops and the subsequent step will not occur unless it receives a trigger to proceed further. This is called a self-limiting feature of the ALP.

Plasma technologies [77, 123] are often used to materialize ALPs. Plasma processing [124–128] has been widely used for deposition and etching technologies in semiconductor manufacturing. Plasmas generate ions and radicals that can physically and chemically modify the surface typically at low surface temperature. Unlike thermal ALPs [40, 122, 129–134], which require surface heating, plasma-assisted ALPs are suited for low-temperature processes. One of the problems of plasma processing in the era of nano-scale devices is, however, the damage formation on the processed surface [70, 135–138] caused by ion bombardment.

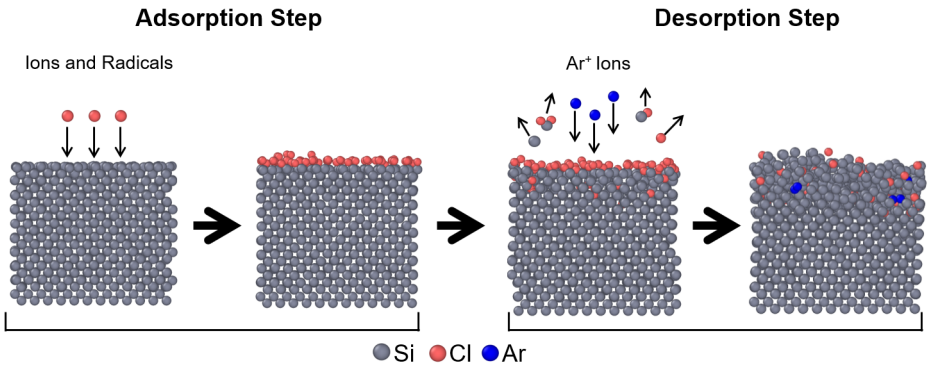

Figure 5.1: A single cycle of Si PA-ALE by Cl adsorption and Ar^+ ion irradiation. Each cycle consists of the adsorption step, where the Si surface is modified by incident Cl atoms and/or ions, and the desorption step, where the Cl modified surface is removed by low energy Ar^+ ion impact. Here, gray, orange and blue spheres represent Si, Cl, and Ar atoms (or ions), respectively.

The goal of this study is to understand the damage formation by low-energy ion bombardment used in silicon (Si) plasma-assisted ALE (PA-ALE) based on chlorine (Cl) adsorption. Figure 5.1 shows a schematic process flow of such an ALE process. In the adsorption step, a Si surface is exposed to a Cl-containing plasma or Cl_2 gas and its surface is chlorinated. This is to activate the surface by weakening the binding energies of surface atoms. If a Cl containing plasma is used without bias voltage in this step, the surface is chlorinated by Cl radicals as well as Cl^+ ions incident upon the surface at the plasma potential energy. If a Cl_2 gas is used, Cl_2 molecules are dissociated at the Si surface and only the top layer gets chlorinated. Under ideal conditions, no etching occurs

in the adsorption step. In the desorption step, the surface is irradiated with low-energy Ar^+ ions and the Cl modified surface may be removed by the impact. Because our aim is to remove the Cl modified surface layer only, the incident Ar^+ ions should not be energetic enough to etch a bare Si surface. Once the Cl modified surface is depleted, the etching is expected to stop. This defines the self-limit feature of ALE. These two steps form a single cycle of ALE, which is repeated a number of times until the desired etching depth is achieved.

Effects of ion impact on a material surface have been widely studied by ion beam experiments [52]. For example, detailed studies were performed to determine the sputtering yields of Si by Ar^+ or Cl^+ions [57, 65, 139–143], and chlorinated Si surfaces by Ar^+ ions [59, 144], for a wide range of ion incident energy. Molecular dynamics (MD) simulations [145–147] were also used to study such systems and their results [34, 38, 39, 66, 146, 148] are in good agreement with the experimental observations in general. Therefore, the basic nature of the desorption step of Si PA-ALE by Cl adsorption has been reasonably well understood. What we attempt to clarify in this study is how the etched surface of the preceding cycles affects the outcome of the following ALE cycles, depending on the ion incident energy. To achieve this goal, we also use MD simulation in this study.

Earlier experimental studies of PA-ALE by halogen adsorption were first reported by Horiike *et al.* [16, 17] in 1990 and several studies on PA-ALE by Cl adsorption followed [18, 20, 22, 23, 149, 150]. In these experiments, Cl_2 gas was used in the adsorption step, depositing a thin layer of Cl atoms on the Si surface. Thus, the measured etch per cycle (EPC), i.e., the averaged etched depth in a single ALE cycle, was small. A more recent study by Tan *et al.* [24] used a Cl plasma in the adsorption step, which led to the formation of a relatively thick Cl-Si mixed layer on the surface and exhibited a higher EPC. MD simulations [35, 148] and simulations based on other models [28, 30, 151–153] were also used to study PA-ALE of Si by Cl adsorption. Athvale *et al.* [35] first performed MD simulation of an ALE process. They briefly discussed the surface damage of Si PA-ALE but focused only on the first cycle. Kubota *et al.* [148] examined the reaction pathways of the desorbed species. A recent study by Huard *et al.* [30] used

a hybrid plasma equipment model to study the factors affecting ideal ALE processes. Sherpa *et al.* [153] examined a Cl adsorption step by *ab initio* MD simulation. Berry *et al.* [28] used Monte Carlo simulations to investigate the effect of ion impact angle on the ALE window. Regarding the past studies on PA-ALE for other materials, the reader is referred to, e.g., Refs. [25–27, 32, 154–156] for SiO_2, Refs. [29, 32, 157–164] for SiN, and Refs. [165–168] for metal oxides.

Most of the previous simulation studies on PA-ALE focused only on the first ALE cycle and there was no extensive discussion on the magnitude of surface damage formed over multi-cycle ALE. In this study, we performed MD simulations for multi-cycle Si PA-ALE processes to assess the surface damage formation.

5.2 MD Simulation

MD simulation [145, 147] was employed to reproduce PA-ALE of Si by Cl adsorption. The details of the simulation were discussed in previous publications [38, 39, 67, 69, 85, 169–171]. The interatomic potential functions for the Si-Cl-Ar system used in this study are the same as those used in Ref. [85]. The interatomic potential functions for ions are assumed to be the same as those for the corresponding charge-neutral atoms for the sake of simplicity. An incident Ar^+ ion is considered to be charge-neutralized right before it impacts upon the Si surface owning to the Auger emission process.

The top surface prior to the ALE process examined in this study is the (100) crystalline Si surface. The model material has a top surface with an area of 3.26 x 3.26 nm^2 and the initial material depth is 2.72 nm. Periodic boundary conditions are imposed on the horizontal directions, such that the model surface emulates a large surface of the actual material. The material is kept sufficiently deep (if necessary, additional layers of Si atoms are added from the bottom automatically) during the simulation so that the injection of particles (i.e., ions or charge-neutral species) would not affect the motions of atoms near the bottom of the material. The initial temperature of the material is set at 300K. The simulation is composed of repeated "injection cycles," in each of which an ion or charge

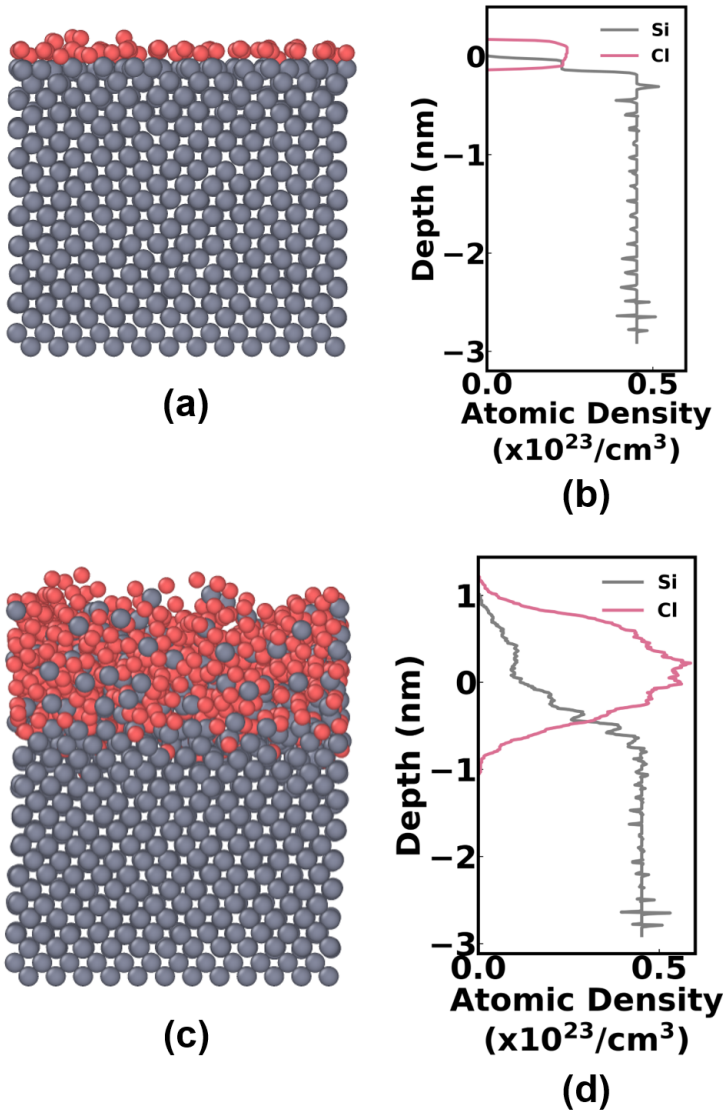

Figure 5.2: Si materials after Cl deposition MD simulations. (a) A crystalline Si material model with a (100) top surface at 300 K after it was exposed to 0.1 eV Cl atoms with an atomic dose of 0.94×10^{15} cm^{-2} in MD simulation. (b) The depth profiles of atomic densities corresponding to (a). (c) A crystalline Si material model with a (100) top surface at 300 K after it was exposed to 20 eV Cl^+ ions with an ion dose of 9.4×10^{15} cm^{-2} in MD simulation. (d) The depth profiles of atomic densities corresponding to (c). In both (a) and (c), red and gray spheres represent Cl and Si atoms and the angle of incidence was normal to the initial (100) Si surface. The depth is measured from the position of the top (100) surface of the initial Si material prior to the deposition of Cl. The atomic density was obtained as a moving average with an interval of 3 Å as a function of the depth. The Cl adsorption conditions for (a) and (c) are called the "thin Cl layer deposition" and "thick Cl layer adsorption" in this article.

Table 5.1: Simulation parameters for Si PA-ALE.

Parameters	Values
Incident kinetic energy of an incident Cl atom or ion	
Thin Cl layer deposition	0.1 eV
Thick Cl layer deposition	20 eV
Dose of Cl atoms or ions	
Thin Cl layer deposition	$0.94 \sim 1.88 \times 10^{15}$ cm^{-2}
Thick Cl layer deposition	9.4×10^{15} cm^{-2}
Ar^+ ion energy	$20 \sim 60$ eV
Ar^+ ion dose	1.88×10^{17} cm^{-2}
Angle of incidence for Ar^+ ions	normal to the surface
Number of cycles	6

neutral species is injected into the material with a predetermined incident kinetic energy at a random horizontal location of the material surface. The angle of incidence is set perpendicular to the material surface.

The duration of each injection cycle is 2,000 fs. Newton's equation of motion is solved for each particle in the system, except for the atoms located in the two monolayers at the bottom of the material. The atoms in these layers are fixed in position to prevent the material from moving downwards due to the momentum transfer from the incident particles. A variable time step is used in the simulation code to ensure the accuracy of the simulation and the typical time step employed in this study is 0.4 fs.

In each injection cycle, the MD simulation is performed under the constant-total-energy (i.e., microcanonical) conditions for the first 300 fs. During this period, we have confirmed that the material temperature increases due to the particle injection and most surface chemical reactions (i.e., the breakage and reformation of chemical bonds) take place. After the microcanonical simulation, the system is then cooled down to the initial temperature, using the Langevin thermostat [72, 147] for the subsequent 1,600 fs and Berendsen thermostat for the final 100 fs with a target temperature of 300 K. We have confirmed that the simulation system successfully returns to thermodynamical equilibrium at 300 K before the subsequent injection cycle starts.

In this study, we examined two different cases for Cl adsorption. In the first case, a thin layer of Cl atoms was deposited on the Si surface in the adsorption step, terminating

nearly all Si dangling bonds on the surface. In the MD simulation, we created such a Cl monolayer by injecting a sufficiently large number of Cl atoms with a kinetic energy of 0.1 eV in the (negative) vertical direction, i.e., direction normal to the initial material surface. Figure 5.2(a) shows a side view of a Cl adsorbed (100) crystalline Si surface obtained from MD simulation in this way. In this particular example, an average of 75 Cl atoms (i.e., 7.1×10^{14} cm^{-2}) remained on the surface. The depth profiles of Si and Cl atoms of (a) are given in (b). The horizontal axis represents the atomic density and the vertical axis represents the depth (in negative values). The atomic density here is evaluated as a moving average over an interval of 3 Å as a function of the depth. It is seen that nearly all Cl atoms were bonded with Si atoms on the top layer. In experiments, such a layer may be formed by the exposure of a clean Si surface to Cl_2 gas. The thin Cl layer of Fig. 5.2(a) represents the final atomic configuration of the adsorption step of the first ALE cycle in this case. In later cycles, where the surface may be rough and no longer crystalline due to the ion bombardment in the preceding cycles, we also performed similar MD simulations to emulate the adsorption steps. As the surface became rough and more active sites for Cl adsorption appeared in later cycles, we varied the atomic Cl dose to ensure that a Cl monolayer was formed on the surface in the adsorption step of each cycle.

In the second case, a thick Cl-containing layer was formed with 20 eV Cl^+ ion injection in MD simulation. As in the cases of (a) and (b) of Figure 5.2, ions were injected in the direction normal to the material surface and the total number of injected Cl^+ ions were 1000 (i.e., 9.4×10^{15} cm^{-2}) and the number of Cl atoms that remained on or under the Si surface was 704 (i.e., 6.6×10^{15} cm^{-2}). Figure 5.2(c) shows a side view of the Si material surface after this simulation and (d) shows the corresponding depth profiles of atomic densities. It is seen that a layer of mixed Cl and Si atoms with a thickness of about 2 nm is formed on the Si surface. In experiments, such a layer may be formed by the exposure of a clean Si surface to a chlorine-containing plasma. The relatively thick Cl layer of Fig. 5.2(c) represents the final atomic configuration of the adsorption step of the first ALE cycle in this case. As in the first case, in later cycles, we also performed the

same MD simulations to emulate the adsorptions steps of this case. The Cl deposition processes of the first and second cases above will be referred to hereinafter as the "thin Cl layer deposition" and "thick Cl layer deposition" in this article.

After the Cl adsorption step, 20,000 Ar^+ ions (corresponding to an ion dose of 1.88×10^{17} cm^{-2}) were injected into the Cl adsorbed surface to remove the chlorinated Si layer. The Ar^+ ion energy was varied from 20 to 60 eV in both cases. The angle of incidence was normal to the material surface. A summary of the simulation parameters is given in Table 5.1.

5.3 Results and Discussion

5.3.1 Changes in Etched Depth

Changes in etched depth during the desorption steps of Si PA-ALE obtained from MD simulations are summarized in Fig. 5.3. The blue curve represents the position of the Cl-adsorbed top surface (i.e., material height) as a function of the Ar^+ ion dose in the desorption steps over 6 ALE cycles. No adsorption step is shown in this figure. The material height is measured from the position of the initial crystalline Si surface prior to the first Cl adsorption step, as in Fig. 5.2. The Ar^+ ion dose in the horizontal axis is denoted by the cycle number "Cn" with $n = 1, \ldots, 6$ for the n-th ALE cycle. Each cycle corresponds to an Ar^+ ion dose of 1.88 x 10 ^{17}/cm^2. The origin of the horizontal axis is the beginning of the desorption step of the 1^{st} ALE cycle (C1). Its end, marked by a dashed vertical line, is also the beginning of the desorption step of the 2^{nd} ALE cycle (C2). Later cycles are also delineated by vertical dashed lines. The sudden increase of the blue curve at each vertical line indicates the increase of the surface height due to the Cl adsorption step not shown in this figure. The adsorption steps of (a) and (b) were performed under the "thin Cl layer deposition" conditions while those of (c) and (d) were under the "thick Cl layer deposition" conditions. The ion incident energies in the desorption steps were 20 eV for (a) and (c) and 50 eV for (b) and (d).

The Si etching by Ar^+ ion bombardment only, i.e., without Cl deposition, was also

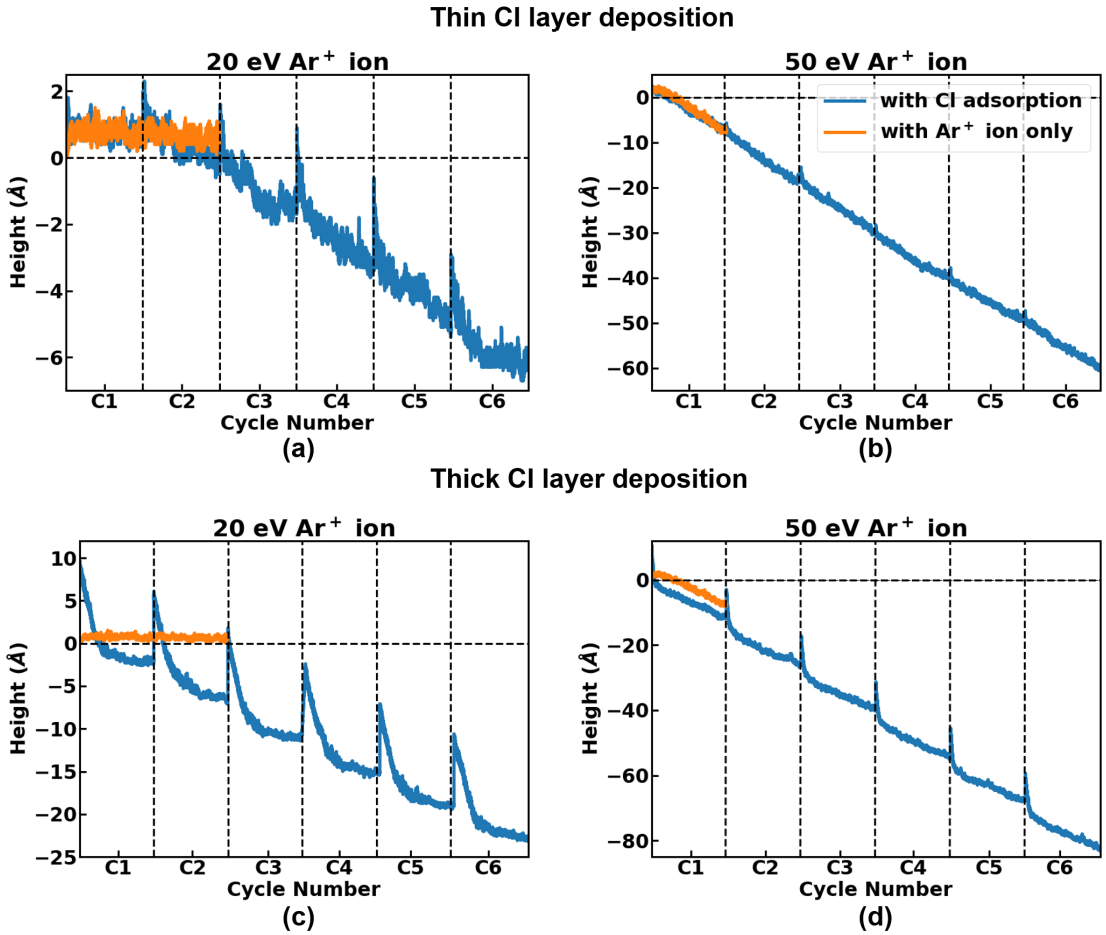

Figure 5.3: Changes in the material height as functions of the Ar^+ ion dose during the desorption steps over 6 ALE cycles, obtained from MD simulations. No Cl adsorption step is included in this figure. The blue curve represents the position of the Cl-adsorbed top surface. The adsorption steps for (a) and (b) were performed under the "thin Cl layer deposition" conditions and those for (c) and (d) were under the "thick Cl layer deposition" conditions. The incident Ar^+ ion energy in the desorption steps for (a) and (c) is 20 eV and that for (b) and (d) is 50 eV. The vertical axis represents the material height (i.e., the position of the top surface), measured from the position of the initial (100) Si surface, denoted by the horizontal dashed line. The horizontal axis is proportional to the Ar^+ ion dose, whose cycle number is denoted by Cn with $n = 1, \ldots, 6$ for the n-th cycle. The Ar^+ ion dose in each cycle is $1.88 \times 10^{17}/\text{cm}^2$. The orange curve represents the position of the top Si surface subject only to Ar^+ ion bombardment (i.e., without Cl layer adsorption steps). The dashed vertical lines delineate separate cycles.

simulated to differentiate the Cl effects on the ALE process. The orange curve represents the position of the Si top surface subject to Ar^+ ion physical sputtering only as a function of the Ar^+ ion dose. The ion energy for (a) and (c) is 20 eV and that for (b) and (d) is 50 eV. The orange curves in (a) and (c) are the same, and so are those for (b) and (d).

It is seen in Fig. 5.3(a) that the etched depth in a single cycle increased initially and became nearly constant in later cycles. This is because Ar^+ ion bombardment in the first two cycles roughened the Si surface and created more active sites that can be bonded with Cl atoms in the subsequent adsorption cycles. This process formed a thicker Si-Cl mixed layer that can be more readily removed in the subsequent desorption step than crystalline Si [153]. A similar trend is also seen in (c), but to less extent. Orange curves in (a) and (c) show that Si was hardly etched by 20 eV Ar^+ ions. It is also seen that Ar^+ ion bombardment amorphized the surface and increased the volume of the surface region, resulting in a surface higher than the initial crystalline surface.

For 50 eV Ar^+ ion bombardment, there is no notable difference in slope between the blue and orange curves. Especially in (c) for the thin Cl layer deposition, the etching was essentially due to physical sputtering only. This is because 50 eV energy is sufficiently high to etch a pristine Si surface for about a nanometer over this ion dose. In (d) for the thick Cl layer deposition, it is seen that a Si-Cl mixed layer was removed in the very early stage of each desorption step and the etching became essentially due to physical sputtering for the remaining period of the step.

The etched depth and surface concentration of Cl atoms in a single ALE cycle averaged from the third to sixth cycle are plotted in Fig. 5.4 as functions of the Ar^+ ion dose in the desorption step. Here the etched depth is defined as the position of the top surface measured from its position at the end of the previous desorption step. In this figure, the etched depth is plotted only when it takes a positive value. As in Fig. 5.3, (a) and (b) are for the thin Cl layer deposition case and (c) and (d) are for the thick Cl layer deposition case. The incident Ar^+ ion energy is 20 eV for (a) and (c) and 50 eV for (b) and (d). At low Ar^+ ion incident energy, it is seen that, with the increasing Ar^+ ion dose, the etched depth in (a) increased slowly with a weakly decreasing slope whereas the

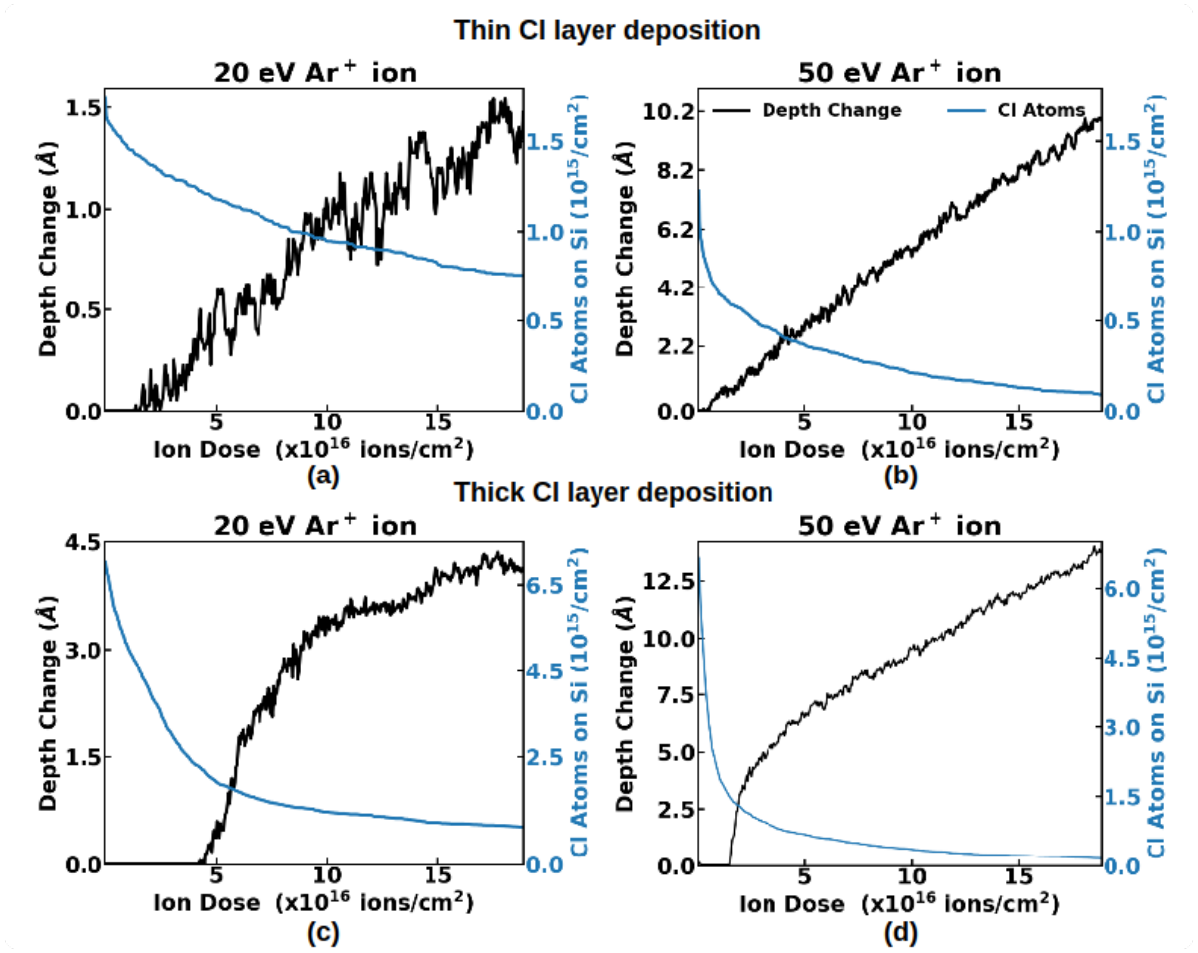

Figure 5.4: Changes in the etched depth (black) and surface concentration of Cl atoms (blue) as functions of the Ar^+ ion dose in the desorption step. Here the etched depth is defined as the position of the top surface measured from its position at the end of the previous desorption step. The ALE conditions for (a)-(d) are the same as those for (a)-(d) of Fig. 5.3, respectively. The results shown here are the averages of those over C3 - C6 cycles. The etched depth is defined as the position of the top material surface measured from that prior to the Cl adsorption step.

etched depth in (c) increased rapidly with a clear sign of saturation, i.e., the self-limit. The surface concentrations of Cl atoms also decreased slowly and nearly one-half of the initial Cl atoms remained on the surface at the end of the ALE cycle in (a) whereas the surface concentrations of Cl atoms in (c) decreased sharply with the Ar^+ ion dose. It should be noted, however, that, even in the case of (c), a small amount of Cl, with a surface concentration similar to that in (a), still remained on the Si surface at the end of the ALE cycle.

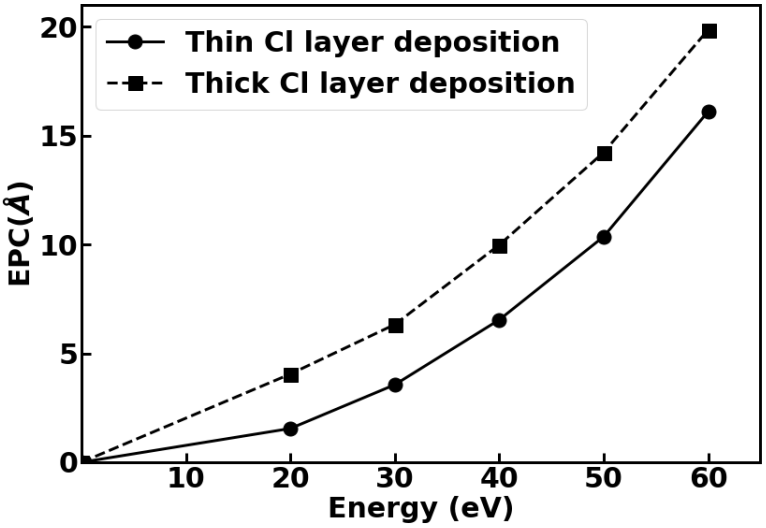

Figure 5.5: EPCs of Si PA-ALE processes obtained from MD simulations as functions of Ar^+ ion incident energy. The solid and dashed lines represent those for the thin and thick Cl layer deposition cases. Other ALE conditions are listed in Table 5.1. The value of EPC given here is the average of etched depths per cycle from C3 to C6.

At high Ar^+ ion incident energy, it is seen in (b) that, with a small amount of Cl deposited in the adsorption step, the etched depth monotonically increased all throughout the Ar^+ ion injection, indicating that the physical sputtering dominates the etching process. In (d), where a larger amount of Cl was deposited in the adsorption step, the etched depth increased drastically until about 5×10^{16} cm^{-2} and then increased monotonically in the same way as in (b). In both cases, the density of Cl atoms at the end of the ALE cycle is almost negligible. This shows that, as we saw in Fig. 5.3, no self-limit took place with 50 eV Ar^+ ions.

The EPCs with the thin and thick Cl layer deposition conditions obtained from MD

simulations are summarized in Fig. 5.5 as functions of the Ar^+ ion energy. The figure shows that the EPC is higher in the thick Cl layer deposition case than in the thin Cl layer deposition case, indicating that the thickness of the chlorinated layer is an important factor in determining the EPC. The simulated EPCs at 20 eV Ar^+ ion energy with thin and thick Cl layer deposition cases are 1.6 and 4.2 Å/cycle. In terms of the thickness of a single monolayer (ML) of Si (i.e., 1.36 Å), these correspond to 1.2 and 3.0 ML/cycle. No ALE window [23, 24, 149, 150] was observed in our simulation.

5.3.2 Damage Formation

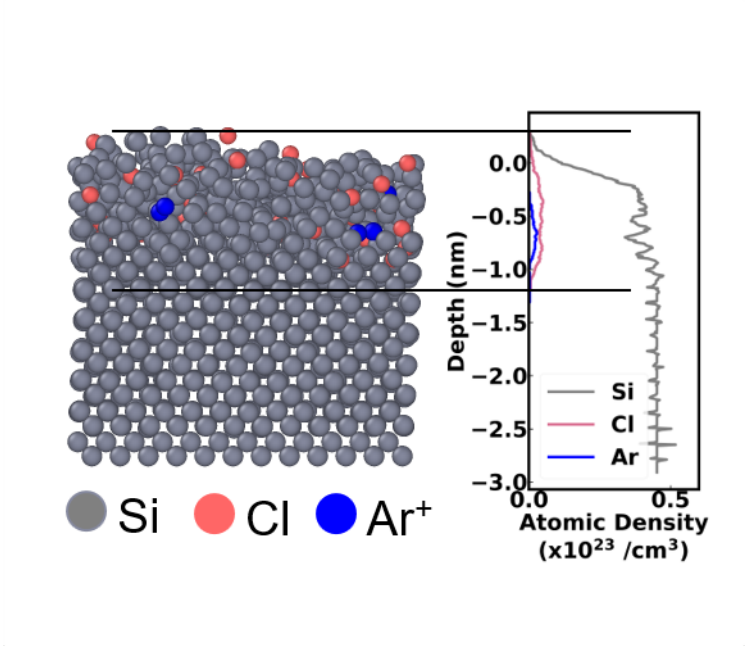

Figure 5.6: Atomic configurations and the corresponding atomic-density depth profiles at the end of the first ALE cycle (C1) with the thin Cl layer deposition at 20 eV Ar^+ ion bombardment. The other conditions are the same as those in Table 5.1. The gray, red, and blue spheres represent Si, Cl, and Ar atoms, respectively. The depth profile was obtained in the same way as in Fig. 5.2.

The depth profiles after each ALE cycle were used to measure the surface damage formed during the ALE processes. Figure 5.6 shows the atomic configurations of the material and the corresponding atomic-density depth profiles after the first ALE cycle (C1) with the thin Cl layer deposition and 20 eV Ar^+ ion bombardment. To characterize the damage formation, the thickness of the damaged-layer was measured from the depth profile, as illustrated in the figure, which is 1.5 nm in this case. In this article, the

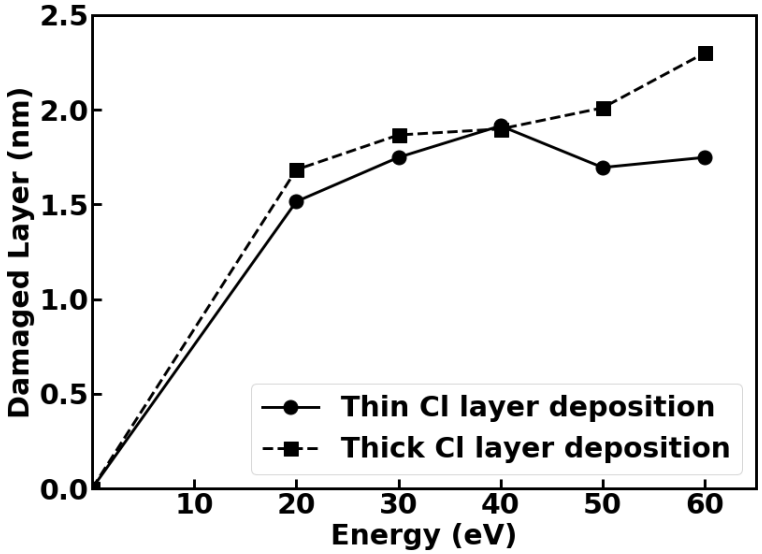

Figure 5.7: The thicknesses of damaged-layers formed during the Si PA-ALE processes, obtained from MD simulations, as functions of the Ar^+ ion incident energy. The solid and dashed lines represent those for thin and thick Cl layer deposition cases. Other ALE conditions are listed in Table 5.1. The value of the thickness here is the average of those over all 6 cycles, i.e., from C1 to C6.

damaged-layer thickness is defined as the penetration depth of Cl or Ar atoms measured from the etched surface.

Figure 5.7 shows the damaged-layer thicknesses as functions of the Ar^+ ion incident energy for the thin (solid lines) and thick (dashed lines) Cl layer deposition cases. The damaged-layer thickness was averaged over the first six cycles (i.e., from C1 to C6) under each ALE condition. Considering the uncertainty arising from the cycle-to-cycle variations, we can conclude from this figure that, for both thin and thick Cl layer deposition cases, the damaged-layer thicknesses weakly and more-or-less linearly increase with the increasing incident ion energy in the energy range studied here. With an increasing ion incident energy, the penetration depths of Ar^+ ions and recoiled Cl atoms increase but so do the etch rates. In other words, a large part of the damaged-layer formed during the desorption step is etched away at high ion incident energy. It is also seen that the damaged-layer is slightly thicker in the thick Cl layer deposition case.

The fact that, in both thin and thick Cl deposition cases, the observed damaged-layer thickness was about 1.5 nm (i.e., approximately 11 Si monolayers) even at 20 eV

ion incident energy can be problematic. The damaged-layer thickness observed here is significantly higher than the corresponding EPC at 20 eV ion energy and comparable at 60 eV. Therefore, the ALE damage formation may not be ignored in actual applications.

5.3.3 Desorbed Species

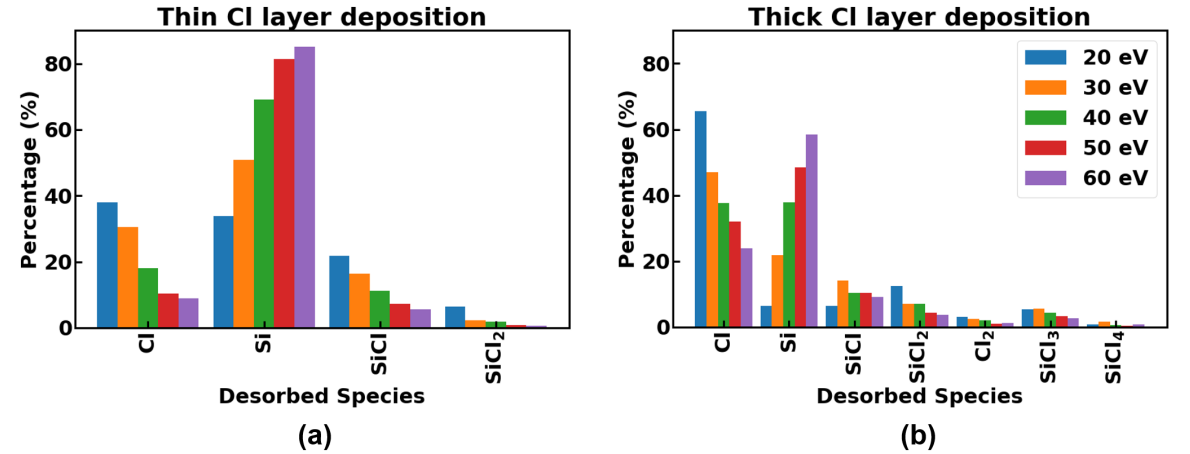

Figure 5.8: Dominant desorbed species during the desorption steps for different Ar^+ ion energies in the thin (a) and thick (b) Cl layer deposition cases. The color indicates the Ar^+ ion energy. Reflected or desorbed Ar ions or atoms are not counted.

We also analyzed the desorbed species during the ALE processes to understand the etching mechanisms better. Figure 5.8 shows the percentage of the number of desorbed species in the ALE desorption steps obtained from MD simulations. Here (a) is for the thin Cl layer deposition case and (b) is for the thick Cl layer deposition case. Any species emitted from the surface has a form of Ar or Si_nCl_m with n and m being non-negative integers. The total number of emitted species in the form of Si_nCl_m during the 6^{th} cycle (C6) examined here corresponds to 100 %. No Ar atom or ion emitted or reflected from the surface is counted because most of the incident Ar^+ ions are reflected once they hit the surface. Dominant desorbed species are listed on the horizontal axis. The color indicates the Ar^+ ion energy.

As it is seen in Fig. 5.8(a), only a small percentage of Cl bonded Si species such as SiCl and $SiCl_2$ desorbed from the surface. This is most likely due to the limited availability of Cl atoms on the surface under the thin Cl layer deposition conditions. The percentage of monoatomic Si atoms as desorbed species increases with the increasing Ar^+ ion energy,

which indicates that physical sputtering of Si by Ar^+ ion impact dominates at higher ion incident energy.

It is seen in (b), where more Cl atoms are available for surface reactions, that desorbed species with higher Cl content, including $SiCl_3$ and $SiCl_4$, are more visible. The percentage of monoatomic Si atoms also increases with the increasing Ar^+ ion energy, as in (a). These results indicate that ALE with the thick Cl layer deposition is enhanced by chemical etching, i.e. the formation of more $SiCl_m$ ($m = 1,...,4$), due to the abundant presence of Cl atoms supplied during the adsorption step.

Figure 5.9 shows the accumulated numbers of desorbed species in the desorption step of C6 as functions of the Ar^+ ion dose under various conditions. The vertical axis denotes the accumulated number of each species desorbed from a unit area of the material surface measured from the beginning of the desorption step. The adsorption steps for (a) and (b) are the thin Cl layer deposition and those for (c) and (d) are the thick Cl layer deposition, as given in Table 5.1. The incident energy of Ar^+ ions is 20 eV for (a) and (c) and 50 eV for (b) and (d).

It is seen in (a) that the dominant desorbed species is monoatomic Cl and the accumulated numbers of desorbed monoatomic Si atoms and SiCl radicals, which are the next highest after monoatomic Cl, are almost the same initially. However, as the amount of Cl on the surface depletes, the rates of desorption for SiCl and $SiCl_2$ decrease while monoatomic Si atoms continue to desorb. Furthermore, the desorption rate of monoatomic Si decreases as that of monoatomic Cl also decreases. It should be noted that the desorption of monoatomic Si does not mean the etching is purely due to physical sputtering. As we have seen in Fig. 5.3, the physical sputtering yield of Si by 20 eV Ar^+ ion bombardment is null essentially. The enhanced desorption of monoatomic Si atoms is likely caused by the bond breaking of Si atoms by Cl atoms remaining in the material.

With more abundant Cl species on the surface, we observe in (c) that Si atoms mostly desorb as Cl bonded species in an early stage of the desorption step. At 50 eV Ar^+ ion injection, as seen in (b) and (d), the desorption of $SiCl_m$ is observed only in the very early stage of the Ar^+ ion injection. On the other hand, the desorption of monoatomic Si

continues to increase with the Ar^+ ion dose due to physical sputtering. This is consistent with the observation in Fig. 5.3.

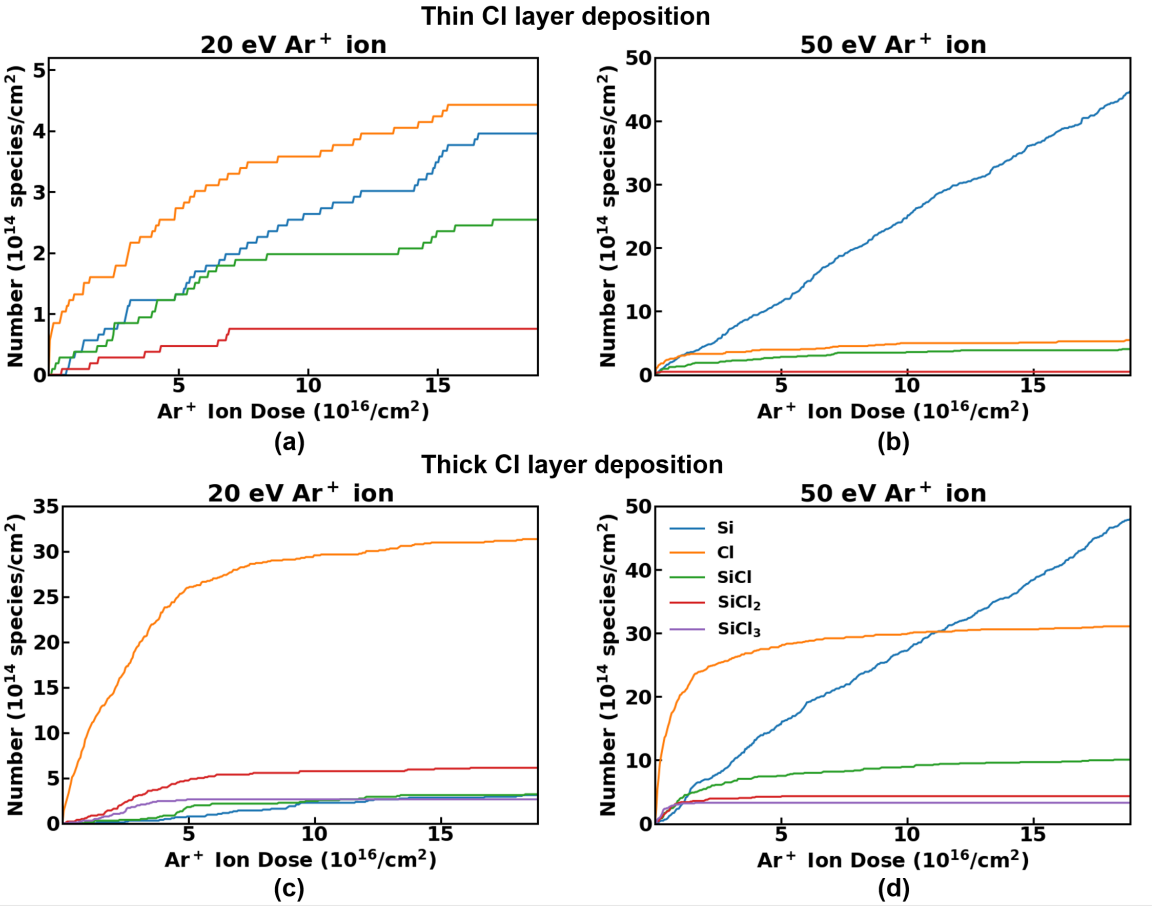

Figure 5.9: The numbers of desorbed species as functions of the Ar^+ ion dose during the desorption step of the 6th cycle (C6) of Si PA-ALE processes. The ALE conditions are the same as those in Table 5.1. The vertical axis denotes the accumulated number of species desorbed from a unit area of the material surface during the desorption step of this cycle. The adsorption steps for (a) and (b) are the thin Cl layer deposition and those for (c) and (d) are the thick Cl layer deposition. The incident energy of Ar^+ ions is 20 eV for (a) and (c) and 50 eV for (b) and (d). The blue, orange, green, red, and gray curves indicate the total numbers of desorbed Si, Cl, SiCl, $SiCl_2$, and $SiCl_3$ species during C6, respectively.

5.4 Conclusions

We performed MD simulations of PA-ALE processes of Si with Cl adsorption under various conditions and examined the effects of the amount of deposited Cl and Ar^+ ion incident energy on the etch rates, values of EPC, and damage layer formation.

In this study, we used a rather large Ar^+ ion dose of 1.88×10^{17} cm^{-2} to clarify the self-limit feature of the PA-ALE process. The ion flux Γ_i from an Ar plasma may be given approximately by

$$\Gamma_i = n_e u_B \,,$$

where n_e and $u_B = \sqrt{k_B T_e / M}$ are the electron density and Bohm velocity with k_B, T_e, and M being the Boltzmann constant, electron temperature, and Ar mass. For a typical inductively coupled plasma (ICP) [172] with $T_e = 5$ eV and $n_e = 2.0 \times 10^{11}$ cm^{-3}, we obtain $\Gamma_i = 7.0 \times 10^{14}$ $cm^{-2}s^{-1}$, i.e., an ion current of 0.11 mA/cm^2. With this ion flux, the duration of the desorption step with an Ar^+ ion dose of 1.88×10^{17} cm^{-2} is 270 sec or 4.5 min. Since few past publications on PA-ALE experiments presented the ion flux used in their studies, it is not clear how realistic our simulation results are. However, based on the plasma conditions reported in those publications, we surmise that the present study uses rather extended desorption steps, compared with typical PA-ALE experiments.

Figures 5.3(a), 5.4(a), and 5.9(a) show that, in the thin Cl layer deposition case, the self-limit was not observed at 20 eV Ar^+ ion injection even with this long desorption step. Figures 5.4(a) and 5.9(a) seems to imply that the etched depth and the amount of desorbed Cl were going to saturate and the self-limit could have occurred eventually. However, nearly a half of the original amount of Cl desorbed on the surface would remain in the material even in the self-limit state. On the other hand, as seen in Figs. 5.3(c), 5.4(c), and 5.9(c), with a larger amount of Cl on the surface, the etched depth and desorbed species reached their steady states and the self-limit of PA-ALE was achieved during the desorption step. At 20 eV Ar^+ ion irradiation, it took this long desorption time to show the self-limit under our simulation conditions.

At 50 eV Ar^+ ion irradiation, the physical sputtering yield of Si may not be negligible. The data compiled by Yamamura and Tawara [143] suggests that the Si sputtering yield at 50 eV Ar^+ ion bombardment is about 0.01. In our simulation, it is shown to be about 0.025. As shown in (b) and (d) of Fig. 5.3, the etched depth purely by Si physical sputtering during this desorption period is about 1 nm, based on our MD simulation. Even if our MD simulation overestimates the etch rate at this ion energy, the etched

depth during this desorption period is likely to be at least a few Å. This means that, if the EPC is about a monolayer (i.e., 1.36 Å), physical sputtering cannot be ignored in this energy range unless the desorption time or ion flux is kept small significantly [150]. As seen in Fig. 5.3(d), with a sufficient amount of Cl on the surface, chemically enhanced etching occurs at a very early stage of each desorption step, which would make the depth change look more self-limiting if the desorption time were sufficiently short.

The results of our study thus indicate that, to obtain an etch stop in a single ALE cycle (i.e., self-limit), one has to employ the right combination of the amount of Cl deposited in the adsorption step and the ion energy in the desorption step. If the amount of adsorbed Cl is too low or the ion energy is too high, physical sputtering dominates during the desorption step. In the opposite case, either no etching occurs or etching takes place too slowly to deplete the deposited Cl atoms and does not exhibit a self-limiting etch stop during the desorption step. In general, a sufficient amount of Cl needs to be adsorbed or deposited in the adsorption step to have a sufficiently high chemical etch rate compared with the physical sputtering rate of pristine Si at the given Ar^+ ion energy.

As seen in Fig. 5.5, in our MD simulation, we did not observe an ALE window, which has been reported in earlier experimental studies [23, 24, 149, 150] under various conditions. It is not clear why we did not observe it even with a sufficiently long desorption time. Indeed, above 40 eV, the major part of the EPC shown in Fig. 5.5 is due to physical sputtering in this figure. (In the thin Cl layer deposition case, EPC is nearly entirely due to physical sputtering at or above 40 eV.) Our simulations have shown that a chlorinated Si layer has a higher etch rate than the physical sputtering rate of pristine Si but the chemical etch rate also depends on the Ar^+ ion energy. Such difference in the etch rate of chlorinated Si is reflected in the difference in EPC between 20 and 30 eV of Fig. 5.5. Another possible reason is the lack of thermal desorption of Si in our MD simulation. As discussed earlier, our MD simulation quenches the system soon after the sputtering or emission of surface atoms occurs by a single ion impact, which prevents slow thermal desorption of surface atoms and moieties. At low ion incident energy, where the etch rate due to the direct Ar^+ ion impact is sufficiently low, the contribution from thermal

processes may not be negligible. Detailed discussion on the lack of ALE windows in our simulation is the subject of a future study.

The damaged-layer thickness, i.e., the thickness of a subsurface region where recoiled Cl (and possibly Ar) atoms remain after the ALE, is plotted in Fig. 5.7. Under the conditions that we examined, the damaged-layer thickness was higher than 1.5 nm and a weakly increasing function of the ion energy. The difference in the damaged-layer thicknesses between the thin and thick deposition cases was not particularly large. As shown in Fig. 5.6, the density of Cl atoms in the damaged-layer is about 0.5×10^{22} cm^{-3}. Because the damaged-layer thickness is significantly larger than the EPC at low ion incident energy and at best comparable with the EPC at relatively high ion energy, the formation of a damaged-layer whose thickness it not negligible compared with the EPC is unavoidable for all the energy range examined here. Depending on the device structures to which such ALE processes are applied, the damage formation may affect the device performance.

Chapter 6

General Conclusions

In this research, classical MD simulation was utilized to study two important etching processes in the miniaturization of electronic devices: reactive ion etching (RIE) and plasma assisted atomic layer etching (PA-ALE) processes of Si and SiO_2 materials.

In Chapter 2, the effects of the amount of F atoms on the RIE of Si and SiO_2 surfaces were studied via classical MD simulation. $C_2F_5^+$ and NF_2^+ ions were injected on the Si and SiO_2 surfaces, which are commonly used as stacked materials in 3D NAND devices. The simulation results, which has a very good agreement with multi-beam injection system experimental data, show that for both surfaces, $C_2F_5^+$ ion bombardment lead to higher etching yields especially at higher energy. These results indicate that the amount of F atoms and ion energy are important factors in achieving high etching yields, which is important in high aspect ratio etching of stacked layers in the fabrication of 3D NAND devices. However, for Si material, the etching yield with NF_2^+ ion bombardment is higher compared with CF_3^+ ion bombardment even though CF_3^+ ion contains more F atoms. The etching yields at 500 eV NF_2^+ and $C_2F_5^+$ ion bombardments are also almost the same. This can be due to the formation of amorphous layer on the surface especially silicon carbide, which is relatively a hard material. This is supported by the formation of amorphous C layer, composed of Si-C, C-F and C-C bonds with Si-C as the dominant bond, at 500 eV $C_2F_5^+$ ion energy as observed in the bond distribution analysis. These results indicate that aside from the number of F atom content, the reaction of the ion's components on

the material's surface should also be considered to optimize the etching process. The depth profiles also showed that for all cases, thick mixing layer was formed wherein few layers of the top surface is heavily fluorinated. This layer provided an avenue for the chemical reactions such as bond breaking to take place. It was observed that as the ion energy increases, the atomic density of F atoms on the mixing layer decreases which indicates that physical sputtering effect dominates at higher ion energy. These findings are consistent with the analysis of the desorbed species. For both Si and SiO_2 materials, the percentage of monoatomic Si desorbed species increases with ion energy. At the same time, the percentage of SiF desorbed species increases while SiF_2, SiF_3 and SiF_4 decrease with increasing ion energy. In fact, SiF_4 is almost negligible at 2,000 eV ion energy. These results show that while the etching does not become fully physical sputtering at higher ion energy, the etching is due to the combination of physical and chemical sputtering effects, i.e. F atoms terminate some of the Si-Si bonds, thus less energy is required to remove the Si atoms from the surface as indicated by the increase in SiF desorbed species.

In Chapter 3, a simple Stillinger-Weber (SW) potential type function to describe the sulfur (S) and F systems was used to study the RIE of Si and SiO_2 materials with SF_5^+ ion bombardment. Here, the interactions of S with Si and O were assumed to be repulsive using Molière potential for simplicity. This is based on the *ex-situ* XPS observations from previous studies that S atoms are not observed on the surface after SF_6 plasma etching. However, this might be an oversimplification of the S-Si, S-O and S-S interactions and can lead to large deviation from actual experimental results. Nevertheless, the simulated etching yields of Si and SiO_2 with SF_5^+ ion bombardment have a good agreement with the multi-beam injection system experimental results. The comparison of the simulated etching yields of Si material with SF_5^+ ion bombardment and $C_2F_5^+$ ion bombardment in Chapter 2 showed that the etching yield is higher with SF_5^+ ion bombardment for all energy range. This further supports that, indeed, C atoms form relatively hard layer on the Si material surface which can hinder the etching. Therefore, the individual effects of the etchant's components should be carefully considered in finding a suitable gas precursor to achieve high aspect ratio etching. It was also observed that the etching yield of Si is

significantly higher than that in SiO_2. However, the etch depth for a given SF_5^+ ion dose is lower for SiO_2 than Si or in other words, the etching rate is faster in SiO_2 than Si. At 2,000 eV ion impact, the etch depth of Si and SiO_2 are 12.5 nm and 13.6 nm, which are relatively close. This implies that stacked layers of Si and SiO_2 can be etched through with almost the same etching rate, which indicates that SF_5^+ ion is a good candidate for one step high aspect ratio etching of such materials.

In Chapter 4, the development of interatomic potential fuctions of Si, O and I systems using modified SW potential functions was presented. Using the newly developed potentials, the RIE of Si and SiO_2 materials with I^+ ion in the energy range of 300 eV to 2,000 eV was studied. Based on the depth profile analysis, the I atoms penetrated deeply into the materials especially in the case of Si, which can be due to the heavy mass of the I atom. It was also observed that I atoms have the highest atomic density at the middle part of the mixing layer. Because no experimental data is available, the etching yields of Si and SiO_2 with I^+ ion bombardment were compared with multi-beam injection system experimental results with other halogen ions such as F^+, Cl^+ and Br^+. The results showed that there is no significant difference with the etching yields, which implies that the simulation results can be reasonable. However, it is still important to verify the results using experimentally obtained data. Based on the analysis of the desorbed species, physical sputtering of monoatomic Si desorbed species is dominant in all energy range for both Si and SiO_2 materials. Moreover, only O monoatomic desorbed species and no O_2 desorbed species were present in the case of SiO_2 material. Few percentage of SiI_x (x = 1 - 3) desorbed species was also observed. In fact, no SiI_4 was reported. As observed in the depth profile analysis wherein the atomic density of deposited I atom is very high, this can be due to I atoms terminating all the Si-Si, Si-O and O-O bonds leading to the desorption of monoatomic Si and O desorbed species.

In Chapter 5, classical MD simulation was employed to study the surface damage formation in PA-ALE of Si with Cl adsorption and Ar^+ ion bombardment. This is important as ALE process is known to have no damage or very low damage on the material, which makes it desirable in nano-scale etching. Two different settings for the

adsorption step was studied. First is the thin Cl layer deposition case wherein a monolayer or very thin layer of Cl was deposited on the Si surface. Second is the thick Cl layer deposition case wherein around 2 nm thick Cl layer was deposited on the Si surface. In the desorption step, the deposited layer was irradiated with Ar^+ ions with an energy range of 20 - 60 eV. However, a relatively long desorption time was used compared to what is commonly reported in literature. The simulation showed that at 20 eV Ar^+ ion injection, the Si surface was not etched even after a very long Ar^+ ion dose. However, with the Cl adsorption, etching of Si was observed. Moreover, the etching curves became more consistent after one or two cycles. In the case of high Ar^+ ion energy (50 eV), etching is already observed even without the Cl adsorption. The etching rate with thin Cl layer deposition and without Cl layer deposition at this energy value is almost the same, while the etching is further enhanced in the thick Cl layer deposition case. These results indicate that the etching is induced by Cl adsorption especially at very low energy, and 50 eV Ar^+ ion energy is already enough to etch a bare Si surface. The summary of the etch per cyle (EPC) for all Ar^+ ion energy range showed that, in general, higher EPC was obtained with the thick Cl layer deposition case and the EPC increased as the energy increased. At 20 eV Ar^+ ion bombardment, EPC values of 1.6 and 4.2 Å/cycle, which correspond to 1.2 and 3.0 ML/cycle, were calculated. However, the EPC window, which was reported in several publications, was not observed. Based on the analysis of the surface damage, the thickness of the damaged-layer more-or-less linearly increases with the Ar^+ ion energy. The damaged-layer is also slightly thicker in the thick Cl layer deposition case. However, more importantly, around 1.5 nm damaged-layer thickness was calculated for both thin and thick Cl layer deposition cases even at very low Ar^+ ion energy of 20 eV. This is equivalent to around 11 Si monolayers. Depending on the application, this can be problematic as this is comparable with the simulated corresponding EPC values for both thin and thick Cl layer deposition cases. Consequently, the damage formation must be taken into account in actual applications.

Overall, the results showed that classical MD simulation is a useful tool to study the RIE and ALE of Si-based materials. The extension of the potential functions to other

chemistries to discover new etchants and precursors for etching processes that can cater to the challenges in nano-scale fabrication of future electronic devices is a subject for future research.

Bibliography

[1] *Moore's law*. URL: https://www.britannica.com/technology/Moores-law (visited on 05/26/2021).

[2] K. Parat and C. Dennison. "A floating gate based 3D NAND technology with CMOS under array". In: 2015 IEEE International Electron Devices Meeting. Washington, DC USA, 2015.

[3] S.J. Whang et al. "Novel 3-Dimnesional Dual Control-Gate with Surrounding Floating-Gate (DC-SF) NAND Flash Cell for 1Tb File Storage Application". In: 2010 IEEE International Electron Devices Meeting. San Francisco, California, USA, 2010.

[4] Y. Kim et al. In: *IEEE T. Electron. Dev.* 59 (2012), p. 35.

[5] H. Tanaka et al. In: *2007 IEEE Symposium on VLSI Technology* (2007), p. 14.

[6] Y.-H. Hsiao et al. In: *IEEE Electr. Device L.* 36 (2015), p. 1015.

[7] P. Clarke. *Toshiba takes 3D-NAND to 96-layers, 4 bits per cell*. 2017. URL: https://www.eenewseurope.com/news/toshiba-takes-3d-nand-96-layers-4-bits-cell-0 (visited on 05/25/2021).

[8] B. Wu, A. Kumar, and S. Pamarthy. In: *J. Appl. Phys.* 108 (2010), p. 051101.

[9] F. F. Chen. *Introduction to Plasma Physics and Controlled Fusion*. Springer, 2016.

[10] H. F. Winters and J. W. Coburn. In: *Surf. Sci. Rep.* 14 (1992), pp. 161–269.

[11] H. F. Winters and F. A. Houle. In: *J. Appl. Phys.* 54 (1983), p. 1218.

[12] K. J. Kanarik et al. In: *J. Vac. Sci. Technol. A* 33.2 (2015), p. 020802.

[13] M. Wang, P. L. G. Ventzek, and A. Ranjan. In: *J. Vac. Sci. Technol. A* 35 (2017), p. 031301.

[14] A. I. Abdulagatov and S. M. George. In: *J. Vac. Sci. Technol. A* 38 (2020), p. 022607.

[15] A. Fischer et al. In: *J. Vac. Sci. Technol. A* 39 (2021), p. 030801.

[16] Y. Horiike et al. In: *J. Vac. Sci. Technol. A* 8 (1990), p. 1844.

[17] H. Sakaue et al. In: *Jpn. J. of Appl. Phys.* 29 (1990), p. 2648.

[18] H. Sakaue et al. In: *Mat. Res. Soc. Symp. Proc.* 222 (1991), p. 195.

[19] J. Yamamoto et al. In: *Thin Solid Films* 225 (1993), p. 124.

[20] Y. Sawada T. Matsuura J. Murota and T. Ohmi. In: *Appl. Phys. Lett.* 20 (1993), p. 2803.

[21] K. Suzue et al. In: *Appl. Surf. Sci.* 82/83 (1994), p. 422.

[22] S. D. Athvale and D. J. Economou. In: *J. Vac. Sci. Technol. B* 14 (1996), p. 3702.

[23] S. D. Park, D. H. Lee, and G. Y. Yeom. In: *Electrochem. Solid ST.* 8 (2005), p. C106.

[24] S. Tan et al. In: *ECS J. Solid State Sci. Technol.* 4 (2015), N5010.

[25] S. Rauf et al. In: *J. Appl. Phys.* 101 (2007), p. 033308.

[26] D. Metzler et al. In: *J. Vac. Sci. Technol. A* 32 (2014), p. 020603.

[27] T. Tsutsumi et al. In: *J. Vac. Sci. Technol. A* 35 (2017), 01A103.

[28] I. L. Berry et al. In: *J. Vac. Sci. Technol. A* 36(1) (2018), 01B105.

[29] A. Hirata et al. In: *Jpn. J. Appl. Phys.* 59 (2020), SJJC01.

[30] C. M. Huard et al. In: *J. Vac. Sci. Technol. A* 35(3) (2017), p. 031306.

[31] C. M. Huard et al. In: *J. Vac. Sci. Technol. A* 35 (2017), p. 05C301.

[32] C. M. Huard et al. In: *J. Vac. Sci. Technol. A* 36 (2018), 06B101.

[33] S. Huang et al. In: *J. Vac. Sci. Technol. A* 37 (2019), p. 031304.

[34] M. E. Barone and D. B. Graves. In: *J. Appl. Phys.* 78 (1995), p. 6604.

[35] S. D. Athvale and D. J. Economou. In: *J. Vac. Sci. Technol. A* 13 (1995), p. 966.

[36] M. E. Barone, T. O. Robinson, and D. B. Graves. In: *IEEE T. Plasma Sci.* 24 (1996), p. 77.

[37] C. Abrams and D. Graves. In: *J. Appl. Phys.* 86 (1999), p. 11.

[38] H. Ohta and S. Hamaguchi. In: *J. Vac. Sci. Technol. A* 19 (2001), p. 2373.

[39] H. Ohta and S. Hamaguchi. In: *J. Chem. Phys.* 115 (2001), p. 6679.

[40] A. H. Basher, I. Hamada, and S. Hamaguchi. In: *Jpn. J. Appl. Phys.* 59 (2020), p. 090905.

[41] F. H. Stillinger and T. A. Weber. In: *Phys. Rev. B* 31 (1985), p. 5262.

[42] H. Ohta and S. Hamaguchi. In: *J. Plasma Fusion Res. SERIES* 6 (2004), p. 399.

[43] H. Ohta. "Molecular dynamics simulation of the plasma-surface interaction during plasma etching processes". PhD dissertation. Kyoto University, 2004.

[44] R. Car et al. In: *Handbook of Materials Modeling*. Ed. by S. Yip. Netherlands: Springer, 2005. Chap. Firt-principles molecular dynamics.

[45] L. Verlet. In: *Phys. Rev.* 159 (1967), p. 98.

[46] S. Hug. In: *Biomolecular Simulations: Methods and Protocols*. Ed. by L. Monticelli and E. Salonen. New York: Humana Press, 2005. Chap. Chapter 6.

[47] D. J. Tobias, G. J. Martyna, and M. L. Klein. In: *J. Phys. Chem.* 97 (1993), p. 12959.

[48] L. V. Woodcock. In: *Chem. Phys, Lett.* 10 (1971), p. 257.

[49] T. Schneider and E. Stoll. In: *Phys. Rev. B* 17 (1978), p. 1302.

[50] H. J. C. Berendsen et al. In: *J. Chem. Phys.* 81 (1984), p. 8.

[51] W. Dzwinel, J. Kitowski, and J. Mościński. In: *Mol. Simulat.* 7 (1991), p. 171.

[52] K. Karahashi and S. Hamaguchi. In: *J. Phys. D: Appl. Phys.* 47 (2014), p. 224008.

[53] T. Iwase et al. In: *Jpn. J. Appl. Phys.* 55 (2016), 06HB02.

[54] R. Micheloni et al. In: *Computers* 6 (2017), p. 27.

[55] Y.- Y. Tu, T.J. Chuang, and H. F. Winters. In: *Phys. Rev. B* 23 (1981), p. 823.

[56] G. Fortuno. In: *Plasma Chem. Plasma Process.* 8 (1998), p. 1.

[57] S. Tachi and S. Okudaira. In: *J. Vac. Sci. Technol. B* 4 (1986), p. 459.

[58] T. Shibano et al. In: *Appl. Phys. Lett.* 63 (1993), p. 2336.

[59] J. P. Chang and H. H. Sawin. In: *J. Vac. Sci. Technol. A* 15 (1997), p. 610.

[60] K. Ishikawa et al. In: *J. Vac. Sci. Technol. A* 21 (2003), p. L1.

[61] K. Karahashi et al. In: *J. Vac. Sci. Technol. A* 22 (2004), p. 1166.

[62] H. Toyoda et al. In: *Jpn. J. Appl. Phys.* 95 (2004), p. 9.

[63] A. Iwakawa et al. In: *Jpn. J. Appl. Phys.* 47 (2008), p. 11.

[64] R. Knizikevicius. In: *Micro. Engn.* 86 (2009), p. 55.

[65] T. Ito et al. In: *J. Vac. Sci. Technol. A* 31 (2013), p. 031301.

[66] P. Brichon, E. Despiau-Puno, and O. Joubert. In: *J. Vac. Sci. Technol. A* 32 (2014), p. 2.

[67] K. Miyake et al. In: *Jpn. J. Appl. Phys.* 53 (2014), p. 03DD02.

[68] N. Nakazaki et al. In: *J. Appl. Phys.* 118 (2015), p. 233304.

[69] S. Numazawa et al. In: *Jpn. J. Appl. Phys.* 55 (2016), p. 116204.

[70] K. Mizotani, M. Isobe, and S. Hamaguchi. In: *J. Vac. Sci. Tech. A* 33 (2015), p. 0021313.

[71] B. Smit D. Frenkel. *Understanding molecular simulation: From algorithms to applications.* Orlando, FL.: Academic Press, Inc., 1996.

[72] T. Schneider and E. Stoll. In: *Phys. Rev. B* 17 (1978), p. 1302.

[73] H. J. C. Berendsen et al. In: *J. Chem. Phys.* 81 (1984), p. 3684.

[74] S. C. Harvey, R. K. Tan, and T. E. Cheatham. In: *J. Comp. Chem.* 19 (1998), pp. 726–740.

[75] T. Tatsumi et al. In: *J. Vac. Sci. Technol. A* 23 (2005), p. 93.

[76] I. Adamovich et al. In: *J. Phys. D: Appl. Phys.* 50 (2017), p. 323001.

[77] K. D. Weltmann et al. In: *Plasma Process. Polym.* 16 (2019), p. 1800118.

[78] W. W. Brandt and T. Honda. In: *J. Appl. Phys.* 60 (1986), p. 5.

[79] G. S. Oehrlein and S. Hamaguchi. In: *Plasma Sources Sci. Technol.* 27 (2018), p. 023001.

[80] S.H. Lee et al. "A study on film thickness control of vertical flow showerhead reactor for RF plasma deposition". In: 2017 28th Annual SEMI Advanced Semiconductor Manufacturing Conference. Saratoga, Springs, NY, USA, 2017.

[81] T. Iwase, K. Yokogawa, and M. Mori. In: *Jpn. J. Appl. Phys.* 57 (2018), 0JCO3.

[82] T. Iwase et al. In: *Jpn. J. Appl. Phys.* 58 (2019), SE0802.

[83] M. Omura et al. In: *Jpn. J. Appl. Phys.* 58 (2019), SEEB02.

[84] M. A. Vyvoda et al. In: *J. Vac. Sci. Technol. A* 16 (1998), p. 3247.

[85] E. J. C. Tinacba et al. In: *Surf. Coat. Tech.* 380 (2019), p. 125032.

[86] D. Korzec, T. Kessler, and J. Engemann. In: *Appl. Surf. Sci.* 46 (1990), p. 299.

[87] R. d'Agostino and D. L. Flamm. In: *J. Appl. Phys.* 52 (1981), p. 1.

[88] S. F. Yoon. In: *Micro. Engn.* 14 (1991), p. 23.

[89] R. Hsiao and J. Carr. In: *Mater. Sci. Eng. B* 52 (1998), p. 63.

[90] C. Takahashi et al. In: *Jpn. J. Appl. Phys.* 39 (2000), p. 3672.

[91] S. Gomez et al. In: *J. Vac. Sci. Technol. A* 22 (2004), p. 3.

[92] S. Aachboun and P. Ranson. In: *J. Vac. Sci. Technol. A* 17 (1999), p. 2270.

[93] G. S. Oehrlein, J. F. Rembetski, and E. H. Payne. In: *J. Vac. Sci. Technol. A* 8 (1990), p. 1199.

[94] S. Hamaguchi and M. Dalvie. In: *J. Vac. Sci. Technol. A* 12 (1994), p. 2745.

[95] M. J. Frisch et al. In: *Gaussian, Inc., Wallingford CT* (2010).

[96] B. deB. Darwent. *Bond Dissociation Energies in Simple Molecules*. U.S. National Bureau of Standards, 1970.

[97] I. Torrens. *Interatomic Potentials*. New York: Academic, 1972.

[98] K. Suzuki et al. In: *J. Electrochem. Soc.* 129 (1982), p. 2764.

[99] C. Steinbrüchel. In: *Appl. Phys. Lett.* 55 (1989), p. 1960.

[100] H. F. Winters and J. W. Coburn. In: *Surf. Sci. Rep.* 14 (1992), p. 161.

[101] Ch. Steinbrüchel, H. W. Lehmann, and K. Frick. In: *J. Electrochem. Soc.: SOLID-STATE SCIENCE AND TECHNOLOGY* 132 (1985), p. 180.

[102] R. Legtenberg et al. In: *J. Electrochem. Soc.* 142 (1995), p. 2020.

[103] H. Hayashi, K. Kurihara, and M. Sekine. In: *Jpn. J. Appl. Phys.* 35 (1996), p. 2488.

[104] D. E. Hanson, A. F. Voter, and J. D. Kress. In: *J. Appl. Phys.* 82 (1997), p. 3552.

[105] I. W. Rangelow. In: *Surf. Coat. Tech.* 97 (1997), p. 140.

[106] C. Abrams and D. Graves. In: *J. Appl. Phys.* 88 (2000), p. 3734.

[107] F. Gaboriau et al. In: *J. Vac. Sci. Technol. A* 23 (2005), p. 226.

[108] K. Ishikawa et al. In: *Appl. Phys. Lett.* 86 (2005), p. 264104.

[109] K. Yanai et al. In: *J. Appl. Phys.* 97 (2005), p. 053302.

[110] F. Hamaoka, T. Yagisawa, and T. Makabe. In: *IEEE T. Plasma Sci.* 35 (2007), p. 1350.

[111] P. Mukherjee et al. In: *J. Vac. Sci. Technol. B* 28 (2010), C6P70.

[112] T. Ito et al. In: *J. Vac. Sci. Technol. A* 29 (2011), p. 050601.

[113] J. Burgdorfer, P. Lerner, and F. W. Meyer. In: *Phys. Rev. A* 44 (1991), p. 5674.

[114] S. M. George. In: *Chemical Reviews* 110 (2010), p. 111.

[115] H. C. M Knoops et al. In: *J. Vac. Sci. Technol. A* 37 (2019), p. 030902.

[116] S. U. Engelmann et al. In: *ECS J. Solid State Sc.* 4 (2015), N5054.

[117] T. Faraz et al. In: *ECS J. Solid State Sc.* 4 (2015), N5023.

[118] G. S. Oehrlein, D. Metzler, and C. Li. In: *ECS J. Solid State Sc.* 4 (2015), N5041.

[119] K. Ishikawa et al. In: *Jpn. J. Appl. Phys.* 56 (2017), 06HA02.

[120] R. J. Gasvoda et al. In: *J. Vac. Sci. Technol. A* 38 (2020), p. 050803.

[121] X. Sang and J. P. Chang. In: *J. Phys. D: Appl. Phys.* 53 (2020), p. 183001.

[122] S. M. George. In: *Accounts Chem. Res.* 53 (2020), p. 1151.

[123] I. Adamovich et al. In: *J. Phys. D: Appl. Phys.* 50 (2017), p. 323001.

[124] B. N. Chapman. *Glow Discharge Processes: Sputtering and Plasma Etching*. Wiley-Interscience, 1980.

[125] S. Hamaguchi. In: *IBM J. Res. Develp.* 43 (1999), p. 199.

[126] M. A. Lieberman and A. J. Lichtenberg. *Principles of Plasma Discharges and Materials Processing (2nd ed.)* Wiley-Interscience, 2005.

[127] K. Nojiri. *Dry Etching Technology for Semiconductors*. Springer, 2015.

[128] T. Makabe and Z. L. Petrovic. *Plasma Electronics*. Routledge, 2016.

[129] Y. Lee and S. M. George. In: *ACS Nano* 9 (2015), p. 2061.

[130] Younghee Lee and Steven M. George. In: *J. Phys. Chem. C* 123 (2019), p. 18455.

[131] M. Konh et al. In: *J. Vac. Sci. Technol. A* 37 (2019), p. 021004.

[132] A. H. Basher et al. In: *J. Vac. Sci. Technol. A* 38 (2020), p. 022610.

[133] A. H. Basher et al. In: *J. Vac. Sci. Technol. A* 38 (2020), p. 052602.

[134] R. Sheil et al. In: *J. Phys. Chem. C* 125 (2021), p. 1819.

[135] T. Ohchi et al. In: *Jpn. J. Appl. Phys.* 47 (2008), p. 5324.

[136] T. Ito et al. In: *Jpn. J. Appl. Phys.* 50 (2011), 08KD02.

[137] T. Ito et al. In: *Jpn. J. Appl. Phys.* 51 (2012), 08HB01.

[138] K. Mizotani et al. In: *J. Phys. D: Appl. Phys.* 48 (2015), p. 152002.

[139] Shin'ichi Tachi, Kiyoshi Miyake, and Takashi Tokuyama. In: *Jpn. J. Appl. Phys.* 20 (1981), p. L411.

[140] P. C. Zalm. In: *J. Appl. Phys.* 54 (1983), p. 2660.

[141] D. J. Oostra et al. In: *J. Appl. Phys.* 64 (1988), p. 315.

[142] M. Balooch et al. In: *J. Vac. Sci.Technol. A* 14.1 (1996), p. 229.

[143] Y. Yamamura and H. Tawara. In: *Atomic Data and Nuclear Data Tables* 62 (1996), p. 2.

[144] J. A. Levinson et al. In: *J. Vac. Sci.Technol. B* 18 (2000), p. 172.

[145] J. M. Haile. *Molecular Dynamics Simulation: Elementary Methods*. John Wiley and Sons, New York, 1997.

[146] B. A. Helmer and D. B. Graves. In: *J. Vac. Sci. Technol. A* 16 (1998), p. 3502.

[147] M. P. Allen and D. J. Tildesley. *Computer simulation of liquids*. 2nd. Oxford University Press, 2017.

[148] N. A. Kubota, D. J. Economou, and S. J. Plimton. In: *J. Appl. Phys.* 83.8 (1998), p. 4055.

[149] Bum-Jun Kim, Saehoon Chung, and Sung M Cho. In: *Applied Surface Science* 187 (2002), p. 124.

[150] S.-D. Park et al. In: *Jpn. J. Appl. Phys.* 44 (2005), p. 389.

[151] A. Agarwal and M. J. Kushner. In: *J. Vac. Sci. Technol. A* 27 (2009), p. 37.

[152] A. Ranjan et al. In: *J. Vac. Sci. Technol. A* 34 (2016), p. 031304.

[153] Sonam D. Sherpa et al. In: *J. Vac. Sci. Technol. A* 36 (2018), p. 031303.

[154] H. Nishino, N. Hayasaka, and H. Okano. In: *J. Appl. Phys.* 74.2 (1993), p. 1345.

[155] D. Metzler et al. In: *J. Vac. Sci. Technol. A* 34 (2016), 01B101.

[156] M Honda et al. In: *J. Phys. D: Appl. Phys.* 50 (2017), p. 234002.

[157] T. Matsuura, Y. Honda, and J. Murota. In: *Appl. Phys. Lett.* 74 (1999), p. 3573.

[158] C. Li et al. In: *J. Vac. Sci. Technol. A* 34 (2016), p. 041307.

[159] Y. Ishii et al. In: *Jpn. J. Appl. Phys.* 56 (2017), 06HB07.

[160] S. D. Sherpa and A. Ranjan. In: *J. Vac. Sci. Technol. A* 35 (2017), 01A102.

[161] S. D. Sherpa, P. L. G. Ventzek, and A. Ranjan. In: *J. Vac. Sci. Technol. A* 35 (2017), p. 05C310.

[162] K. Nakane et al. In: *ACS Appl. Mater. Inter.* 11 (2019), p. 37263.

[163] K. Shinoda et al. In: *J. Vac. Sci. Technol. A* 37 (2019), p. 051002.

[164] A. Hirata et al. In: *J. Vac. Sci. Technol. A* 38 (2020), p. 062601.

[165] J. B. Park et al. In: *J. of Phys. D: Appl. Phys.* 42 (2009), p. 055202.

[166] S. E. Potts et al. In: *J. Electrochem. Soc.* 157 (2010), P66.

[167] M. Omura et al. In: *Plasma Sources Sci. T.* 26 (2017), p. 065015.

[168] A. Hirata et al. In: 57 (2018), 06JB02.

[169] Hideaki Yamada and Satoshi Hamaguchi. In: *J. Appl. Phys.* 96 (2004), p. 6147.

[170] M. Taguchi and S. Hamaguchi. In: *Thin Solid Films* 515 (2007), p. 4879.

[171] Y. Murakami, S. Horiguchi, and S. Hamaguchi. In: *Phys. Rev. E* 81 (2010), p. 041602.

[172] V. A. Godyak. In: *Plasma Sources Sci. Technol.* 20 (2011), p. 025004.

Research Achievement

Publications

- **E. J. C. Tinacba**, Michiro Isobe, and Satoshi Hamaguchi, *Surface damage formation during atomic layer etching of silicon with chlorine adsorption*, J. Vac. Sci. Technol. A **39** (2021) 042603.

- **E. J. C. Tinacba**, M. Isobe, and S. Hamaguchi, *Molecular dynamics study on the damage formation in atomic layer etching of Si with halogen radicals*, in the Proceedings of Silicon Technology Division, Japan Society of Applied Physics, (2021) pp. 14-16.

- **E. J. C. Tinacba**, Michiro Isobe, Kazuhiro Karahashi, and Satoshi Hamaguchi, *Molecualr dynamics simulation of Si and SiO_2 reactive ion etching by fluorine-rich ion species*, Surf. Coat. Technol. **380** (2019) 125032.

- **E. J. C. Tinacba**, Tomoko Ito, Kazuhiro Karahashi, Michiro Isobe, and Satoshi Hamaguchi, *Molecular dynamics simulation for reactive ion etching of Si and SiO_2 by SF_5^+ ions*, J. Vac. Sci. Technol. B **39** (2021) 043203.

Conferences (International and Local)

- **E. J. C. Tinacba**, M. Isobe, and S. Hamaguchi, *Study of surface damage formation in atomic layer etching of Si via MD simulation*, 21st International Conference on Atomic Layer Deposition, June 27-30, 2021 (presented online).

- **E. J. C. Tinacba**, M. Isobe, and S. Hamaguchi, *Molecular dynamics study of damage formation in atomic layer etching of Si with halogen radicals, Silicon Technology Division Meeting*, Japan Society of Applied Physics, March 25, 2021 (invited talk).

- **E. J. C. Tinacba**, M. Isobe, and S. Hamaguchi, *Construction of classical interatomic potential functions for molecular dynamics simulation of Si and SiO2 by I+ ions*, The 8th International Conference on Microelectronics and Plasma Technology and the 9th International Symposium on Functional Materials, Rolling Hills, Hwaseong, Korea, January 17 – 20, 2021 (presented online).

- **E. J. C. Tinacba**, M. Isobe, and S. Hamaguchi, *Molecular dynamics study on the damage formation in atomic layer etching of Si with halogen radicals*, 18th International Conference on Thin Films & 18th Joint Vacuum Conference, Budapest, Hungary, November 22 – 26, 2020 (presented online).

- **E. J. C. Tinacba**, M. Isobe, K. Karahashi, and S. Hamaguchi, *Molecular dynamis simulation of surface interactions with high-fluorine content ions such as SF5+ in Si and SiO2 reactive ion etching*, 3rd International Symposium of the Vacuum Society of the Philippines, University of San Carlos, Cebu, Philippines, January 8 – 10, 2020.

- **E. J. C. Tinacba**, M. Isobe, K. Karahashi, and S. Hamaguchi, *Reaction mechanisms of high fluorine-content reactive ion etching (RIE) and atomic layer etching (ALE) of Si and SiO2*, Materials Research Meeting 2019, Yokohama Symposia, Yokohama, Japan, December 10 – 14, 2019.

- **E. J. C. Tinacba**, M. Isobe, K. Karahashi, and S. Hamaguchi, *Molecular dynamics simulation of Si atomic layer etching with NF2 radicals and Ar+ ions*, 41st International Symposium on Dry Process, JMS Aster Plaza, Hiroshima, Japan, November 21 – 22, 2019.

- **E. J. C. Tinacba**, M. Isobe, K. Karahashi, and S. Hamaguchi, *Molecular dynamics simulation of Si-based materials plasma etching processes*, 23rd International

School on Low Temperature Plasma Physics: Basics and Applications, Physikzentrum Bad Honef, Bad Honef, Germany, October 5 – 12, 2019.

- **E. J. C. Tinacba**, M. Isobe, K. Karahashi, and S. Hamaguchi, *Surface reaction analysis of fluorine-based reactive ion etching (RIE) and atomic layer etching (ALE) by molecular dynamics (MD) simulation*, AVS 66th International Symposium & Exhibition, Greater Columbus Convention Center, Columbus, Ohio, USA, October 20 – 25, 2019.

- **E. J. C. Tinacba**, M. Isobe, K. Karahashi, and S. Hamaguchi, *Molecular dynamics simulation of reactive ion etching of Si and SiO2 by fluorine containing ions*, XXXIV International Conference on Phenomena in Ionized Gases & 10th International Conference on Reactive Plasma, Sapporo Education and Culture Hall, Sapporo, Hokkaido, Japan, July 14 – 19, 2019.

- **E. J. C. Tinacba**, M. Isobe, K. Karahashi, and S. Hamaguchi, *Molecular dynamics simulation of F-based reactive ion etching of Si, SiO_2, and Si_3N_4 materials*, 62nd Annual SVC Technical Conference, Long Beach Convention Center, Long Beach, California, USA, April 27 – May 2, 2019.

- **E. J. C. Tinacba**, M. Isobe, K. Karahashi, and S. Hamaguchi, *Molecular dynamics simulation of SiO2 etching by NF_2^+ and $C_2F_5^+$ ions*, 66th The Japan Society of Applied Physics Spring Meeting, Tokyo Institute of Technology, Tokyo, Japan, March 9 – 12, 2019.

- **E. J. C. Tinacba**, K. Ueda, M. Isobe, K. Karahashi, and S. Hamaguchi, *Role of F^+ ions on high-speed etching of Si-based materials*, 40th International Symposium on Dry Process, Nagoya University, Nagoya, Aichi, Japan, November 13 – 15, 2018.